

PHOTOELECTRON STUDY OF THE ELECTRONIC AND OPTICAL PROPERTIES
OF POROUS SILICON

by

ANTHONY W. H. VAN BUUREN

B.Sc., Simon Fraser University, 1987
M.Sc. The University of British Columbia, 1991

A THESIS IN PARTIAL FULFILLMENT OF
THE REQUIREMENTS FOR THE DEGREE OF
DOCTOR OF PHILOSOPHY

in

THE FACULTY OF GRADUATE STUDIES

(Department of Physics)

We accept this thesis as conforming
to the required standard

THE UNIVERSITY OF BRITISH COLUMBIA

January 1996

© Anthony W. H. van Buuren, 1996

In presenting this thesis in partial fulfilment of the requirements for an advanced degree at the University of British Columbia, I agree that the Library shall make it freely available for reference and study. I further agree that permission for extensive copying of this thesis for scholarly purposes may be granted by the head of my department or by his or her representatives. It is understood that copying or publication of this thesis for financial gain shall not be allowed without my written permission.

Department of Physics

The University of British Columbia
Vancouver, Canada

Date Feb. 9 / 95

ABSTRACT

Various explanations have been proposed for the strong visible luminescence from porous silicon (PS), the most widely accepted being quantum confinement. In the quantum confinement model the bandgap of PS depends on the size of the microstructure. Double crystal x-ray diffraction on PS shows a narrow peak and a broad peak consistent with a two phase model for the structure of PS in which there is a macroporous backbone supporting a nanoporous surface layer. From the width of the diffuse peak we estimate the size of the silicon structures in the nanoporous region to range between 30-60Å depending on the preparation conditions.

Synchrotron radiation based techniques such as x-ray absorption spectroscopy (XAS) and photoemission spectroscopy (PES) allow direct measurement of the quantum shift in the conduction and valence band edges in porous silicon. High resolution measurements of the silicon L and K-edge absorption in porous silicon show that the absorption threshold is shifted to higher energy relative to bulk silicon, and the shift is dependent on how the porous silicon is prepared. The blue shift of the conduction band minimum in PS is understood qualitatively using a simple LCAO model. The x-ray absorption spectra also show an excitonic enhancement at the Si L edge in PS which increases with the quantum shift in the L-edge absorption. The enhanced excitonic absorption, is in agreement with the expectation that electron-hole interactions increase in silicon nanocrystals because of confinement effects.

PES data show that the valence band of porous silicon is also shifted relative to the bands for bulk silicon. The quantum shift in the valence band is larger than the shift in the conduction band and is proportional to it with a proportionality constant of 2.0 that is independent of preparation conditions. An independent confirmation of the relationship between the quantum shifts in the valence and conduction band edges is obtained from PS annealing experiments. The quantum shifts in the conduction and valence band edges of PS relative to bulk Si are found to decrease with progressively higher annealing temperatures, up to 550°C, at which point the band edge energies revert to the values for bulk Si. The ratio of the shift in the valence band edge to the shift in the conduction band edge remains approximately constant with annealing and equal to 1.9,

in agreement with the ratio determined as a function of preparation conditions. This result suggests that the PS microstructure progressively becomes larger when heated between 400 and 500°C where the surface hydrogen evolves. The ratio of the valence band shift to conduction band shift is predicted to be 1.5 using an effective mass model for the quantum shifts.

Measurements of the Si L-edge were used to probe the effects of different preparation procedures on the electronic structure of PS. When the porous silicon is made from n-type material with light exposure, the blue shift increases logarithmically with the anodizing current and anodization time. We explore the hypothesis that the etching reaction self-limits and that the quantum size effect is a key part of the self-limiting mechanism. Two models have been proposed to explain the light intensity and time dependence of the quantum shift in anodized n-type PS.

The peak energy of the room temperature photoluminescence of PS is compared with the bandgap determined from the XAS and PES measurements for a series of PS sample prepared under different conditions. The photoluminescence bandgap is found to be smaller than the photoelectron spectroscopy bandgap, but exhibits the same trend with preparation conditions. The width of both the photoluminescence spectrum and the L- absorption edge increase with increasing blue shift, consistent with a distribution of quantum confinement energies.

An alternative explanation for the visible PL in PS is emission from a surface siloxene ($\text{Si}_6\text{H}_6\text{O}_3$) layer which is peaked near 550 nm. The structure of siloxene is known to consist of Si (111) layers terminated above and below by OH groups and H atoms. This is difficult to reconcile with photoelectron experiments which show that freshly prepared PS does not contain oxygen. Recently an oxygen-free form of siloxene (Si_6H_6) called layered polysilane has been synthesized. The x-ray absorption of the layered polysilane and PS are found to be remarkably similar. In particular, the K absorption edge of layered polysilane is shifted by 0.6 eV the same as that of the PS samples with the maximum conduction band shift. Conceivably PS could consist of (111) oriented layers of Si terminated with hydrogen with a chemical formula Si_{6n}H_6 , where n is the number of layers and it depends on the preparation conditions. In this picture layered polysilane (n=1) is the limiting form of PS.

TABLE OF CONTENTS

ABSTRACT	Error! Bookmark not defined.
TABLE OF CONTENTS	iv
LIST OF TABLES.....	vi
LIST OF FIGURES.....	vi
LIST OF ACRONYMS.....	ix
ACKNOWLEDGEMENTS.....	x
1. INTRODUCTION	1
1.1 POROUS SILICON REACTION MECHANISM	4
2. EXPERIMENTAL	7
3. PREPARATION OF POROUS SILICON	19
3.1 ELECTROCHEMICAL PREPARATION OF POROUS SILICON	19
3.1.1 Electrolyte.....	21
3.1.2 Current Density.....	22
3.1.3 Doping Type of Silicon Substrate.....	24
3.2 CHEMICAL PREPARATION OF POROUS SILICON.....	28
3.3 PREPARATION OF SILOXENE.....	30
4. MICROSTRUCTURE OF POROUS SILICON.....	32
4.1 SCANNING ELECTRON MICROSCOPY	32
4.2 X-RAY DIFFRACTION	36
5. PHOTOELECTRON SPECTROSCOPY.....	41
5.1 L-EDGE ABSORPTION.....	41
5.2 K-EDGE ABSORPTION.....	47
5.3 EFFECT OF PREPARATION CONDITIONS ON X-RAY ABSORPTION.....	50
5.4 PHOTOEMISSION.....	58

6. SILOXENE	67
7. EFFECT OF PREPARATION CONDITIONS ON BANDGAP	73
7.1 ANNEALING EFFECTS	73
7.2 SELF LIMITING MODEL.....	81
7.2.1 Model 1: Porous Silicon Strongly Coupled to Bulk Silicon	81
7.2.2 Model 2: Porous Silicon Weakly Coupled to Bulk Silicon.....	89
7.3 LIMITING FORM OF POROUS SILICON.....	95
7.4 PHOTOLUMINESCENCE.....	97
8. CONCLUSIONS	103
9. REFERENCES	108

LIST OF TABLES

TABLE 1: RATE OF PS FORMATION AS A FUNCTION OF CURRENT DENSITY.....	24
TABLE 2: FINAL PS COLOUR AS A FUNCTION OF ANODIZATION CONDITIONS	24

LIST OF FIGURES

FIGURE 1: PROPOSED DISSOLUTION MECHANISM OF SILICON ELECTRODES IN HYDROFLUORIC ACID	4
FIGURE 2: A SCHEMATIC OF THE PS-SILICON INTERFACE IN CROSS SECTION.....	6
FIGURE 3: OPTICAL ELEMENTS AND BASIC ARRANGEMENT OF THE "GRASSHOPPER" MONOCHROMATOR.....	8
FIGURE 4: SCHEMATIC OF THE X-RAY ABSORPTION PROCESS AT THE SILICON L-EDGE..	9
FIGURE 5: EXPERIMENTAL DETERMINATIONS OF INELASTIC SCATTERING ELECTRON MEAN-FREE-PATHS	11
FIGURE 6: SCHEMATIC DIAGRAM OF THE PHOTOEMISSION PROCESS.....	12
FIGURE 7: SCHEMATIC DIAGRAM OF THE LVV AUGER ELECTRON SPECTROSCOPY PROCESS.....	14
FIGURE 8: DIAGRAM OF A THE HEATABLE STAINLESS STEEL SAMPLE HOLDER.....	15
FIGURE 9: SAMPLE TEMPERATURE CALIBRATION CURVE.	16
FIGURE 10: APPARATUS FOR THE FABRICATION OF POROUS SILICON FILMS.	20
FIGURE 11(A,B): TYPICAL I-V RELATIONSHIPS FOR N-TYPE AND P-TYPE SILICON.....	26
FIGURE 11(C): ANODIC I-V RELATIONSHIP FOR SILICON IN HF SOLUTION SHOWING THE THREE REGIONS OF DISSOLUTION.	27
FIGURE 12: STRUCTURAL MODELS FOR SILOXENE:.....	30
FIGURE 13: SEM PHOTOMICROGRAPHS OF THE SURFACE AND THE CROSS SECTION OF A PS FILM GROWN FROM P-TYPE 100 SILICON	33
FIGURE 14: SEM PHOTOMICROGRAPHS OF THE SURFACE AND THE CROSS SECTION OF A PS FILM GROWN FROM P+ TYPE 100 SILICON	34
FIGURE 15: X-RAY ROCKING CURVE FOR PS.....	36
FIGURE 16: POROUS SILICON BRAGG PEAK SHIFT AS A FUNCTION OF CURRENT DENSITY.....	37
FIGURE 17: FWHM OF THE DIFFUSE PS X-RAY PEAK AS A FUNCTION OF ANODIZATION CURRENT.....	39
FIGURE 18: TEY MEASUREMENTS OF L _{2,3} EDGE FOR BULK SI AND PS.....	42

FIGURE 19: LCAO CALCULATION OF THE S-DENSITY OF STATES AT THE L ₃ EDGE.....	43
FIGURE 20: L-EDGE ABSORPTION OF BULK SI AND PS OVER A 100 EV ENERGY RANGE..	45
FIGURE 21: L ₁ EDGE ABSORPTION OF BULK SILICON AND PS.....	46
FIGURE 22: TEY MEASUREMENTS OF THE SILICON K EDGE FOR BULK SI AND PS	47
FIGURE 23: LCAO CALCULATION OF THE P-DENSITY OF STATES AT THE L ₃ EDGE.....	48
FIGURE 24: TEY MEASUREMENTS OF THE SI L _{2,3} EDGE IN PS AS A FUNCTION OF ETCH CURRENT.....	50
FIGURE 25: TEY MEASUREMENTS AT THE L-EDGE OF PS AS A FUNCTION OF SOAK TIME.	51
FIGURE 26: PLOT OF THE CONDUCTION BAND EDGE SHIFT AS A FUNCTION OF THE CURRENT DENSITY	53
FIGURE 27: PLOT OF HF CONCENTRATION VERSUS CURRENT DENSITY WITH PL COLOR AS A PARAMETER.....	54
FIGURE 28: PLOT OF CONDUCTION BAND SHIFT AS A FUNCTION OF PS SOAK TIME.	55
FIGURE 29: TEY MEASUREMENTS AT THE L-EDGE FOR STAIN ETCH PS	57
FIGURE 30: PHOTOEMISSION VALENCE BAND SPECTRA FOR BULK SI AND PS	58
FIGURE 31: THE SI 2P CORE LEVELS SPECTRA FOR BULK SI AND PS.....	59
FIGURE 32: PHOTOEMISSION SPECTRA OF THE VALENCE BAND IN PS CORRECTED FOR CHARGING	61
FIGURE 33: CONDUCTION BAND SHIFT AS A FUNCTION OF THE VALENCE BAND SHIFT FOR A SERIES OF PS SAMPLES.	62
FIGURE 34: LVV AUGER SPECTRA MEASURED BULK SI AND PS.	65
FIGURE 35: PHOTOEMISSION SPECTRA OF THE VALENCE BAND OF PS	66
FIGURE 36: CORRELATION BETWEEN THE QUANTUM SHIFTS OF THE AUGER AND VALENCE BAND EDGES FOR A RANGE OF PS SAMPLES.	66
FIGURE 37: TEY MEASUREMENTS OF X-RAY ABSORPTION AT THE SILICON L _{2,3} EDGE FOR SI, PS AND SILOXENE.	68
FIGURE 38: SI K-EDGE ABSORPTION SPECTRA FOR BULK SI, STAIN ETCH PS AND SILOXENE.	68
FIGURE 39: PHOTOEMISSION VALENCE BAND SPECTRA FOR SI, PS AND SILOXENE:	70
FIGURE 40: THE SILICON K-EDGE SPECTRA FOR SI, STAIN ETCH PS AND LAYERED POLYSILANE.....	71
FIGURE 41: L-EDGE ABSORPTION SPECTRA FOR SI, HEAT TREATED SILOXENE, AND AMORPHOUS-SIO ₂	72
FIGURE 42: TEY MEASUREMENTS OF THE SI L _{2,3} EDGE IN PS AS A FUNCTION OF TEMPERATURE.....	74

FIGURE 43: ENERGY SHIFT OF THE CONDUCTION BAND EDGE IN PS AS A FUNCTION OF TEMPERATURE.....	75
FIGURE 44: PHOTOEMISSION SPECTRA OF THE VALENCE BAND OF PS AS A FUNCTION OF ANNEALING.....	76
FIGURE 45: QUANTUM SHIFT IN THE CB, VB AND AUGER EDGE AS A FUNCTION OF TEMPERATURE.....	78
FIGURE 46: CONDUCTION BAND SHIFT AS A FUNCTION OF THE VALENCE BAND SHIFT WITH ANNEALING TEMPERATURE AS A PARAMETER.....	79
FIGURE 47: CURRENT DENSITY AS A FUNCTION OF LIGHT INTENSITY DURING ETCHING OF N-TYPE SI.....	81
FIGURE 48: CONDUCTION BAND EDGE SHIFT AS A FUNCTION OF THE CURRENT DENSITY.....	82
FIGURE 49: CONDUCTION BAND EDGE SHIFT AS A FUNCTION OF THE ANODIZATION TIME.....	83
FIGURE 50: SCHEMATIC DIAGRAM SHOWING A SILICON WIRE ON A BULK SI SUBSTRATE.....	85
FIGURE 51: A SCHEMATIC DIAGRAM OF THE ILLUMINATION WAVELENGTH DEPENDENCE OF THE PS ETCHING PROCESS.....	92
FIGURE 52: X-RAY ABSORPTION SPECTRA OF PS ETCHED WHILE ILLUMINATED BY LIGHT WITH MAXIMUM PHOTON ENERGIES OF 2.0, 2.4 AND 2.7 EV.....	93
FIGURE 53: PLOT OF BANDGAP AS A FUNCTION OF MAXIMUM PHOTON ENERGY OF ILLUMINATION DURING ANODIZATION.....	94
FIGURE 53: PL SPECTRA FROM N-TYPE PS SAMPLES PREPARED AT DIFFERENT CURRENT DENSITIES.....	97
FIGURE 54: PL SPECTRA FROM P-TYPE PS SAMPLES AS A FUNCTION OF SOAK TIME.....	98
FIGURE 55: PL PEAK POSITIONS AS A FUNCTION OF THE PHOTOELECTRON BANDGAP.....	99
FIGURE 56: BROADENING MODEL OF PS X-RAY ABSORPTION SPECTRA.....	101
FIGURE 57: FWHM OF THE PL SPECTRA AS A FUNCTION OF THE QUANTUM SHIFT.....	103

LIST OF ACRONYMS

ΔE_c	Conduction Band Shift
ΔE_v	Valence Band Shift
ΔE_A	Auger Edge Shift
AES	Auger Electron Spectroscopy
BZ	Brillouin Zone
CB	Conduction Band
CBM	Conduction Band Maximum
CG	Canadian Grasshopper
DCM	Double Crystal Monochromator
DOS	Density of States
EtOH	Ethanol
EXAFS	Extended Absorption Fine Structure
FWHM	Full Width Half Maximum
FY	Fluorescence Yield
HF	Hydrofluoric Acid
LCAO	Linear Combination of Atomic Orbitals
MCP	Microchannel Plate
PES	Photoemission Spectroscopy
PL	Photoluminescence
PS	Porous Silicon
PY	Partial Electron Yield
SEM	Scanning Electron Microscopy
TEM	Transmission Electron Spectroscopy
TEY	Total Electron Yield
UHV	Ultra High Vacuum
VB	Valence Band
XAS	X-ray Absorption Spectroscopy

ACKNOWLEDGEMENTS

I would like to acknowledge and thank my supervisor Tom Tiedje who was involved in all aspects of this thesis. Tom was never too busy to answer my many physics questions and was always interested in my thesis work. I found working with Tom both intellectually rewarding and enjoyable, a rare combination.

A special thanks to Steve Patitsas who was responsible for the theoretical modeling of the x-ray absorption spectra. Steve was both a friend and a source of many interesting discussion ranging from physics to politics.

I would like to thank Jeff Dahn, Brian Way, Alf Wilson, Wolfgang Weydanz, Yuan Gao, Sayuri Ritchie, Stefan Eisebitt and Tom Tiedje who all spent countless hours taking data at various synchrotrons around the world. In particular I acknowledge Jeff Dahn who was one of the main reasons I started my graduate studies in Physics.

I thank Robin Coupe for his help with the SEM and his help with many of the diagrams in this thesis. I also thank all the other people in the lab for making my time at UBC both fun and intellectually enriching.

Finally I thank my parents for all the support they have given me during my education and to Catherine for understanding all the time I was home late from the lab.

1. INTRODUCTION

Electrochemical etching of silicon in a hydrofluoric acid (HF) solution produces a highly porous material which exhibits efficient visible photoluminescence (PL), at room temperature.¹⁻⁴ The HF solution etches an array of holes (pores) into the surface of the Si anode when current flows through the electrochemical cell. The size of the pores depend on the wafer resistivity and dopant type, electrolyte composition, temperature, and applied current density.⁵⁻⁷ The formation of porous layers on silicon electrodes anodized in hydrofluoric acid (HF) was first discovered by A. Uhlir at Bell labs in 1956 during studies of electropolishing.⁸ The properties of porous silicon layers were studied intensively in the 1970's because of their potential use in producing silicon layers fully isolated by oxidized porous silicon.⁹

In 1984, low temperature PL in the deep red to near infrared was observed in porous silicon (PS) samples prepared under various conditions.¹⁰ This study suggested that the optical properties of PS were somehow different than bulk silicon. Canham reported visible PL at room temperature from PS that was chemically etched in HF for a few hours after the initial electrochemical etch.¹ The PL peak was found to shift up in energy with decreasing density of the PS layer. The discovery of efficient PL in the visible region from porous silicon (PS) has stimulated enormous interest in the properties of this material. The source of the PL have been attributed to nanometer-scale, quantum confined structures formed by the etching reaction. Various alternative explanations for the unusual optical properties have been proposed as well including surface molecular species such as $(\text{SiH}_2)_n$ ¹¹ or siloxene,^{12,13} although most experimental data currently favour the quantum confinement model.^{1-3,14-19}

The properties of low-dimensional structures can differ significantly from those of the corresponding bulk material and can be tailored to a specific need by adjusting the size. Quantum size effects will occur for structures, where the charge carriers are confined by at least one dimension on the order of 10 nm or less. One expected quantum size effect is the widening of the

bandgap, caused by carriers acquiring the quantum energy of localization. This is demonstrated by the well-known ground state energy and wavefunction of a particle in an infinite square well potential. In equation 1 we see the energy of the ground state is inversely proportional to m^*L^2 :

$$E = \frac{\pi^2 \hbar^2}{2m^* L^2} \quad (1)$$

where m^* is the mass of the particle and L is length of the box. As L becomes smaller the energy of the ground state shifts up. In this thesis we use photoelectron spectroscopy based techniques to measure the conduction and valence bands of porous silicon as a function of preparation conditions. We then interpret our results in terms of a quantum confinement model for the electronic and optical properties in PS.

Since photoelectron spectroscopy involves collection of low energy electrons emitted from the material they are inherently surface sensitive. Consequently in an inhomogeneous material such as PS, the results of the photoelectron spectroscopy may not be directly comparable with the more bulk sensitive optical techniques such as PL. However both PL and photoelectron spectroscopy measurements are sensitive to inhomogeneities in the sample. We explore the relationship between the PL spectrum of PS and the photoelectron spectroscopy measurements of the bandgap for a series of PS samples prepared under different conditions.

It should be noted that there are two distinct wavelength regions in the PL from PS, they are the red-yellow and infrared bands.^{20,21} The red-yellow band is due to quantum confinement possibly supplemented by surface states and the infrared band is correlated with dangling bonds or possible bandgap luminescence in large crystallites. In this work we only measure the red-yellow PL. Blue luminescence has been reported in PS following rapid thermal oxidation. The blue PL may have one of two origins: luminescence from small Si nanocrystals imbedded in silicon dioxide matrix, or luminescence from a defect in the silicon dioxide.^{20,21}

Recently a two phase model for the microstructure of PS has been proposed, in which there is a nanoporous layer responsible for the visible PL on the surface of a macroporous silicon backbone.^{7,22} One can conclude that the etching process is self-limiting and stops when the size of the surface structure reaches some critical value, and thereby protects the porous silicon from complete dissolution. It has been proposed that the self limiting behavior of the etching process is caused by a reduction in the number of holes at the silicon electrolyte interface when the dimensions of the microstructure are small enough to cause a quantum shift in the valence band.³

To test the hypothesis that the self limiting behaviour of the etching process is due to the quantum confinement effect we conduct photoelectron spectroscopy measurements of the conduction- and valence band edges of PS as a function of preparation conditions. High resolution double crystal x-ray diffraction experiments were conducted to explore the two phase nature of the PS microstructure and determine the particle size in the nanoporous layer.

1.1 POROUS SILICON REACTION MECHANISM

Electrochemical anodization of silicon in HF produces a porous material that luminesces efficiently in the visible part of the spectrum. If the silicon is under anodic bias, PS formation is observed as long as the reaction is limited by the charge supply rather than the ionic diffusion in the electrolyte. The chemical reaction that takes place in the etching process requires holes to be available at the semiconductor electrolyte interface. It has been proposed that the self-limiting behaviour of the etching process is caused by a reduction in the number of holes at the

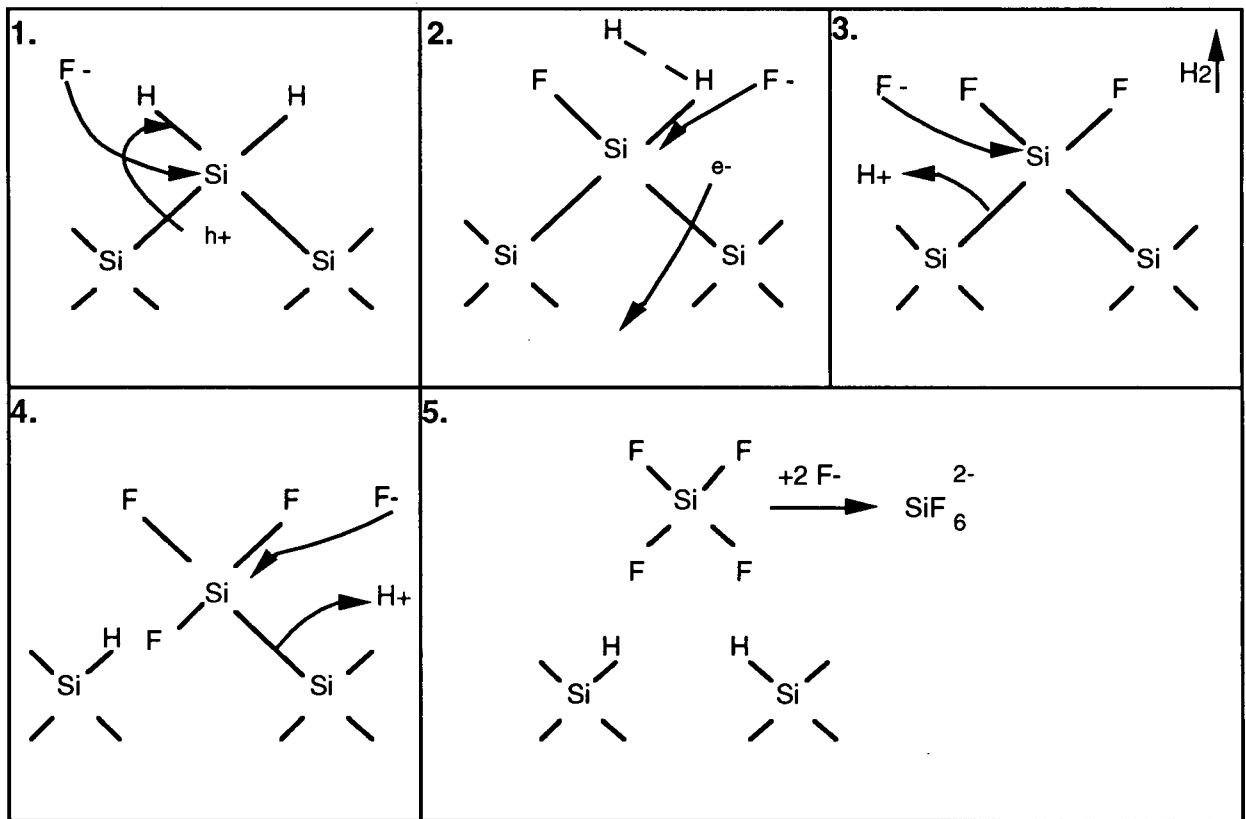


Figure 1: Proposed dissolution mechanism of silicon electrodes in hydrofluoric acid (HF) associated with porous silicon formation. (1) -(5) indicates the sequence of reaction steps involving F, H, Si holes (h⁺) and electrons (e⁻).

semiconductor-electrolyte interface. A dissolution mechanism shown in Fig 1 has been proposed to describe the formation of PS.³ For this mechanism it is essential that a silicon surface covered in hydrogen is virtually inert against further attack by fluoride ions if no electronic holes (h^+) are available at the silicon electrode because the electronegativity of hydrogen is about that of Si and the induced polarization is low. If there are holes available at the Si surface a nucleophilic attack on a Si-H bond by a fluoride ion can occur forming a Si-F bond as shown in step 1. Due to the polarization of the bonded F another fluoride ion can attack with the evolution of hydrogen gas and an electron is then injected into the silicon electrode. (step 2) Polarization from the two Si-F bonds will draw the electron density and weaken the Si-Si backbonds. The weakened backbonds are in turn attacked by HF removing the SiF_4 molecule from the surface leaving the remaining Si surface terminated with H. The SiF_4 molecule is attacked by HF again forming two hydrogen ions and a SiF_6^{2-} ion which is soluble in water. (step 5) Normal fluctuations in the etch rate will cause some areas to etch faster than others. A pit in the surface of the silicon will increase the local electric field distribution, making the hole transfer preferential at this position. Therefore the surface inhomogeneities are amplified.

We propose that the etching process is self-limiting and stops when the thickness of the residual silicon reaches a critical value when the valence band is shifted down in energy due to quantum confinement. In Fig. 2 we show a model of the PS-silicon interface and the corresponding band diagram. If a hole h^+ in the bulk silicon approaches the interface to the PS it needs an additional energy ΔE_v to penetrate into the confined region, whereas no additional energy is necessary to move to the pore tip. Therefore the anodization process preferentially etches the bulk silicon at the bottom of the pores and does not attack the PS film that is left behind on the surface as a product of the reaction. This process is self limiting: a large PS particle implies a low energy barrier for holes; therefore holes can easily move in from the bulk silicon continuing the electrochemical dissolution. The PS particle will become smaller until the bandgap increases to a point where the hole can no longer be transferred from the silicon. The PS then becomes depleted in holes and the reaction stops.

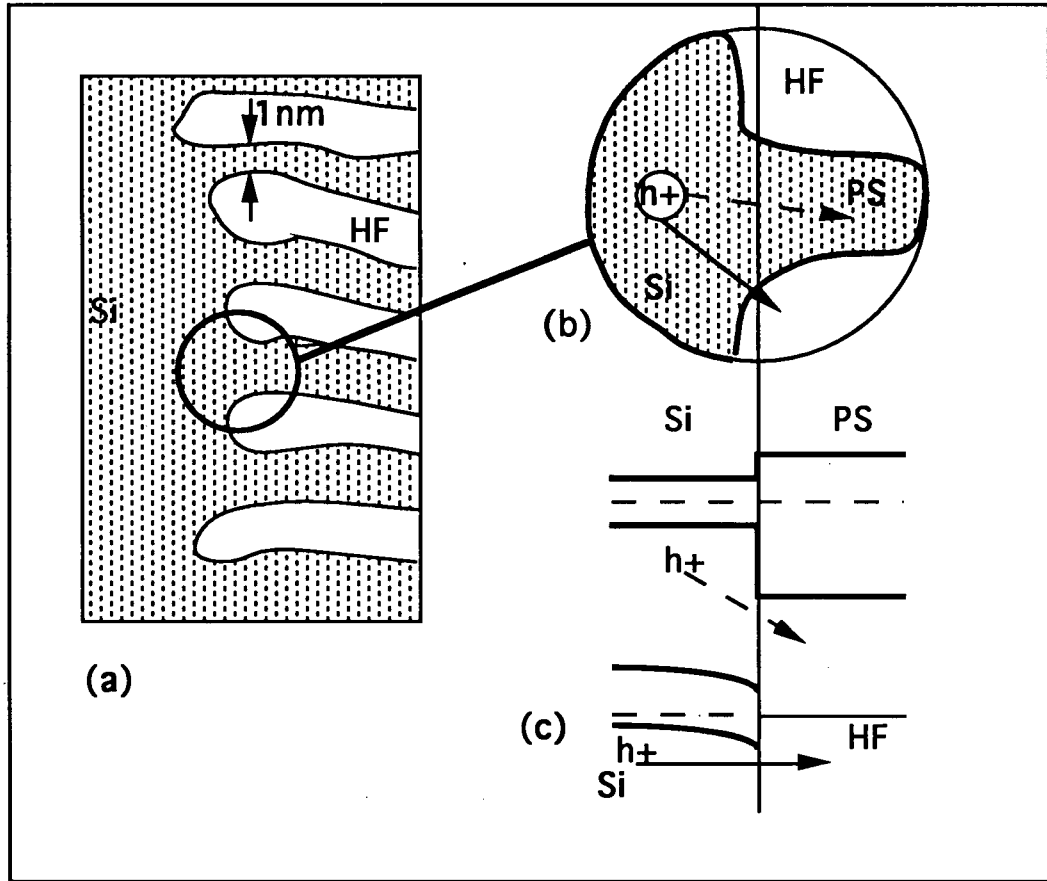


Figure 2: (a) A schematic of the PS-silicon interface in cross section. (b) An enlarged area of the interface showing two possible ways (broken and solid arrow) for a hole to cross the interface are illustrated. (c) The corresponding band diagram of the interface in b showing the two different energy barriers for a hole penetrating into the PS (broken arrow) or a pore tip (solid arrow). Diagram based on Fig.1 of Ref. 4.

2. EXPERIMENTAL

The synchrotron is a storage ring where relativistic electrons are magnetically constrained to a somewhat circular closed path. At the bending magnets in the storage ring the electrons are centripetally accelerated and lose energy via radiation. The synchrotron radiation is intense, peaked in the forward direction and has a continuous spectrum giving it many advantages over conventional x-ray tube sources. Photoelectron experiments in this study were conducted at the following three beamlines; the Canadian grasshopper and double crystal beamlines at CSRF, SRC Wisconsin, and the U1 beamline at the NSLS Brookhaven. The beamlines are situated at bending magnets on the electron storage ring. Since the majority of the photoelectron experiments were conducted at the Canadian Grasshopper (CG) beamline, we will describe the optics of this beamline in more detail. The electrons are injected into the Aladdin storage ring of the SRC at an energy of 800 MeV or 1 GeV with a current of 180 mA and 100 mA respectively.

The CG beamline was designed to cover an energy range from 30-500 eV using a Mark IV grasshopper grazing incidence monochromator.²³ The monochromator is maintained at UHV with a base pressure of 5×10^{-10} torr throughout. Optical elements and the basic arrangement of the grasshopper monochromator are shown in Fig. 3 at zero order and at a mid-range position. The grazing incidence mirror M1 focuses the beam in a vertical plane on the entrance mirror slit S1. This mirror slit combination S1 directs the incoming radiation onto the grating during scanning. The slit width can be varied from 10-400 μm . The grating is mounted on one arm of the Grasshopper's hind legs and pivots about the entrance slit, and together with M1 translates parallel to the incoming radiation. The scanning of the monochromator is accomplished using Rowland circle geometry. A Rowland circle can be thought of as rotating about the exit slit S2, to give a constant exit beam direction.

X-ray absorption spectroscopy (XAS) and photoelectron spectroscopy (PES) can be used to study electronic energy states in matter. In a quantum confined semiconductor one would

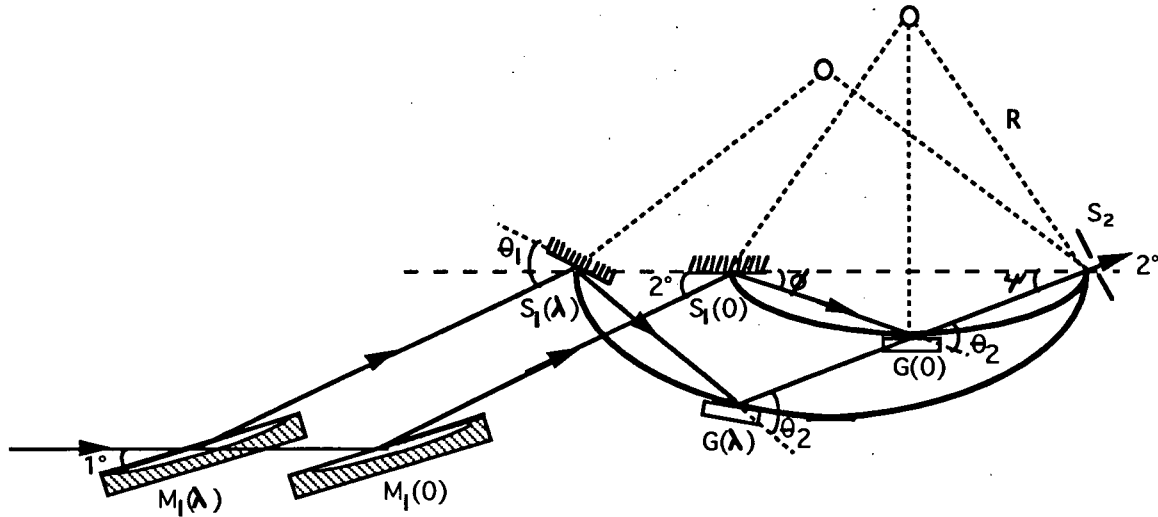


Figure 3: Optical elements and basic arrangement of the "Grasshopper" monochromator.²³ Angles are exaggerated for the purpose of clarity, and two positions are shown, zero order and wavelength λ .

expect a larger bandgap hence the conduction band edge would be at a higher energy and the valence band edge at a lower energy with respect to bulk Si. The XAS process involves the absorption of a photon and the excitation of an electron from a core level into an empty state in the conduction band. In x-ray absorption the conduction band is examined directly as the core hole states are dispersionless. In other words, the electronic structure of interest is not convoluted with another distribution of states. This is an important advantage compared to spectroscopy using visible radiation such as photoluminescence, which involve transitions between the bottom of the conduction band and the top of the valence band. The x-ray absorption spectrum is divided into two regions. The first is the near edge structure (XANES) which is attributed to the density of empty states for the excited electron, the second is the extended absorption fine structure (EXAFS) region which occurs about 100 eV above the absorption edge. In this thesis we will only study the XANES region. The XAS process for the silicon L-edge is shown schematically in Fig. 4. When the incident photon is equal to the energy difference between the 2p core level and the conduction band (approximately 100 eV) a photon can be absorbed and a 2p core hole created. The core hole can decay with the ejection of an Auger electron or the emission of a photon as shown in Fig. 7.

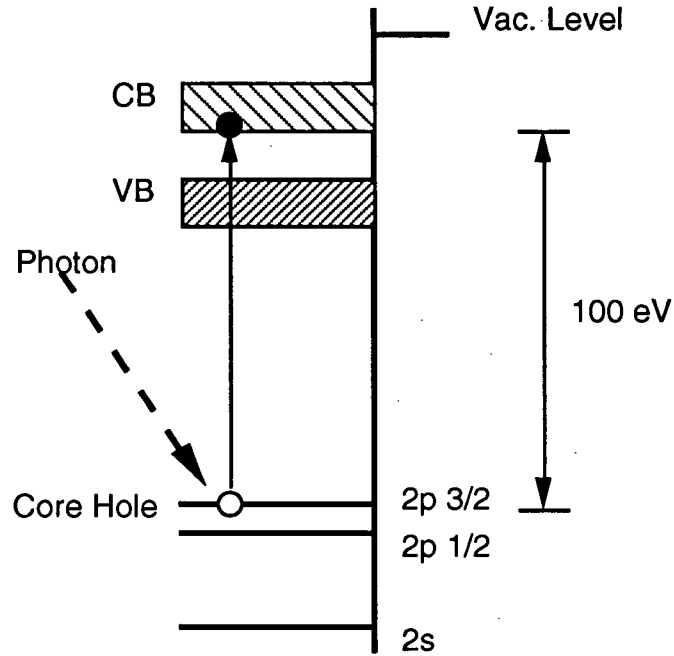


Figure 4: Schematic of the x-ray absorption process at the silicon L-edge.

The initial state $|i\rangle$ for the XAS process is a core electron, while the final state $|f\rangle$ is a core hole with an excited electron in the conduction band. As the atomic dimensions are small compared to the wavelength in the soft x-ray region, Fermi's golden rule for the transition probability per unit time $w_{i \rightarrow f}$ can be applied in the dipole approximation:

$$\omega_{i \rightarrow f} \propto |\langle f | \hat{r} | i \rangle|^2 \delta(E_i - E_f - h\omega) \quad (2)$$

where \hat{r} is the dipole operator. The transition takes place between a localized core orbital and a delocalized state in the CB. If the initial and final state wavefunctions can be separated into single electron wavefunctions a one electron picture can be used to describe the XAS process. Using core wavefunctions to describe the initial state and Bloch wavefunctions expanded in atomic like functions around the atom of interest to describe the final state, the matrix element in equation 2 can

be split into radial and angular parts. Angular integration results in the following dipole selection rules for the absolute angular momentum l and the component of the angular momentum in the z -direction m :

$$\Delta l = \pm 1 \qquad \Delta m = 0, \pm 1 \qquad (3)$$

Fermi's golden rule in the form of equation 2 applies to the transition rate from $|i\rangle$ to $|f\rangle$, where $|f\rangle$ is a single state within a continuum. By summing over all final states we obtain the following expression for the transition rate:

$$\begin{aligned} \omega_{i \rightarrow f} &\propto \int_k |\langle f | \hat{r} | i \rangle|^2 \delta(E_i - E_f - \hbar\omega) k^2 dk \\ \omega_{i \rightarrow f} &\propto |\langle f | \hat{r} | i \rangle|^2 \rho(E_f) \end{aligned} \qquad (4)$$

where $\rho(E_f)$ is the density of final states expressed as a function of energy. Therefore the energy dependence of the XAS spectra is determined by variations in the density of unoccupied states in the conduction band. From an initial $1s$ core level only final states of p symmetry can be reached (K-edge absorption), and an initial $2p$ core level transitions to s and d final states are possible ($L_{2,3}$ -edge absorption).

The final state of the x-ray absorption consists of an excited electron in the CB and a core hole. It is not clear whether the measured conduction band density of states (DOS) corresponds to the system with or without the effect of the core hole. Although controversial, the experimental evidence to date suggests that the DOS measured in XAS corresponds to a system with an additional potential due to the core hole. The sharp onset of the bulk silicon x-ray absorption spectrum has been attributed to the effects of the core hole potential.

The absorption coefficient is measured by total electron yield (TEY) and partial yield (PY). The elastic Auger electron has only a small probability of escaping the silicon without being

inelastically scattered and creating many secondary electrons. In total electron yield all electrons emitted from the sample are collected without regard to energy. The total electron yield is composed of photoelectrons, Auger electrons and inelastically scattered or secondary electrons. It is well established that the TEY signal is proportional to the absorption coefficient.²⁴

The TEY signal is measured with a microchannel plate detector which collects the electrons ejected from the sample or by measuring the current produced by the ejected electrons. The electron detector consists of two microchannel plates each biased to produce 10^4 secondary electrons for each charged particle or incident photon. A grid in front of the MCP can be biased positive to attract more secondary electrons and increase the signal or biased negative to suppress the secondary electrons and detect only the higher energy Auger electrons. In Fig. 5 we show the universal curve for the inelastic mean free path of electrons in matter as a function of electron

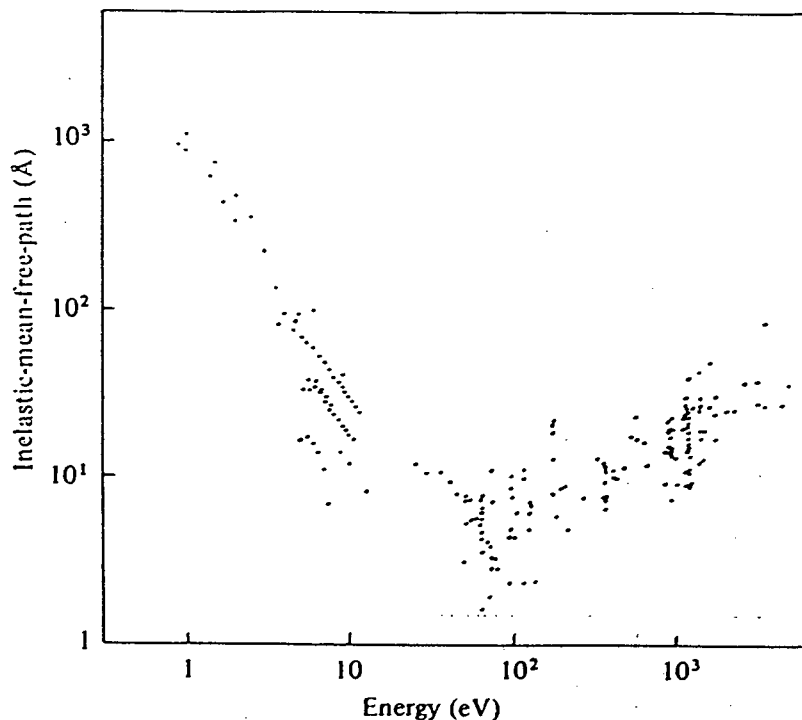


Figure 5: Collection of experimental determinations of inelastic scattering electron mean-free-paths as a function of energy above the Fermi level for many different materials. Diagram after Ref. 25.

energy.²⁵ Since the kinetic energy of secondary electrons is approximately 5-10 eV, the TEY technique will be a sensitive probe to a maximum depth of 100Å. In PY a negative bias is applied to the electron detector, this has the effect of making the absorption measurement much more surface sensitive. The elastic Auger electrons have an energy of 90 eV therefore the escape depth of the Auger electron is on the order 10Å as shown in Fig. 5.

The resolution of the x-ray absorption experiments on the CG beamline at a photon energy of 100 eV was found to be 0.03 eV. The Si K-edge absorption spectra were measured at the double crystal monochromator (DCM) beamline at CSRF. Details of the DCM monochromator have been described elsewhere.²⁶ The DCM is designed to cover a photon energy range from 0.8-2.8 KeV and has an energy resolution of 0.9 eV at a photon energy of 1840 eV, which is the energy of the silicon K-edge. The reported resolution of the monochromator at the U1 beamline at the NSLS is 0.1 eV at a photon energy of 100 eV.²⁷

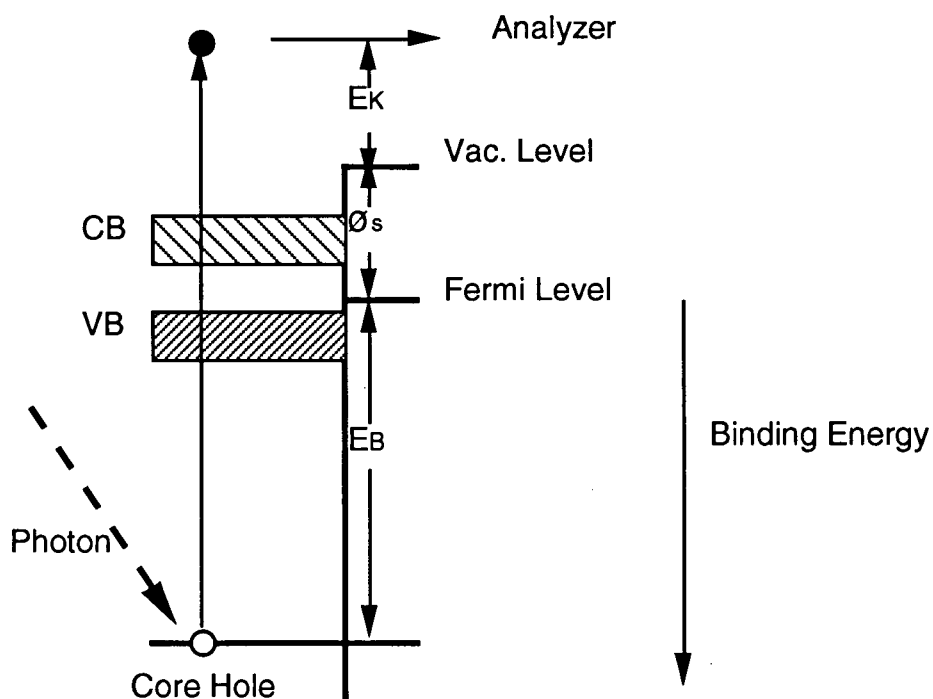


Figure 6: Schematic diagram of the photoemission process.

Unlike XAS, photoelectron spectroscopy (PES) probes the filled electronic states and can be used to measure binding energies of electrons in core levels as well as the density of states in filled bands. The photoemission process is shown schematically in Fig. 6 where monochromatic x-rays of energy $h\nu$ are absorbed by the sample resulting in the ejection of electrons with kinetic energy E_K . From conservation of energy we can write

$$h\nu = E_B + E_K + \phi_s \quad (5)$$

where E_B is the binding energy of the electron state and ϕ_s is the work function of the sample. Therefore one can obtain the binding energy of the filled states by measuring the kinetic energy of the ejected electrons. The binding energy of an electronic state is defined as the energy difference between that state and the Fermi level. The work function is defined as the energy difference between the Fermi level and the vacuum level. A hemispherical energy analyzer (VSW-HAC 100) was used to determine the kinetic energy of the ejected photoelectron. This is a type of electrostatic deflection analyzer which consists of two spherical electrodes set at different potentials. The spherical electrodes have a set pass energy, only electrons with the correct kinetic energy will pass through to the detector. Prior to entering the spherical electrodes the photoelectrons pass through a retarding potential which can be scanned. The kinetic energy of the photoelectron is then defined as

$$E_K = E_R + E_P + (\phi_a - \phi_s) \quad (6)$$

where E_R is the retarding potential, E_P is the pass energy, ϕ_a is the work function of the electron energy analyzer and $(\phi_a - \phi_s)$ is the contact potential. If we substitute this equation for E_K into equation (5) we get

$$h\nu = E_B + E_R + E_P + \phi_a \quad (7)$$

This is a desirable result because one does not need to know ϕ_s which depends on preparation conditions and must be measured independently for each sample. The spectrometer work function ϕ_a was determined to be 4.5 eV and was assumed to be a constant. The combined resolution of the CG monochromator and the electron energy analyzer for the photoemission experiments was 0.25 eV at a photon energy of 100 eV and an entrance slit width of 30 micron.

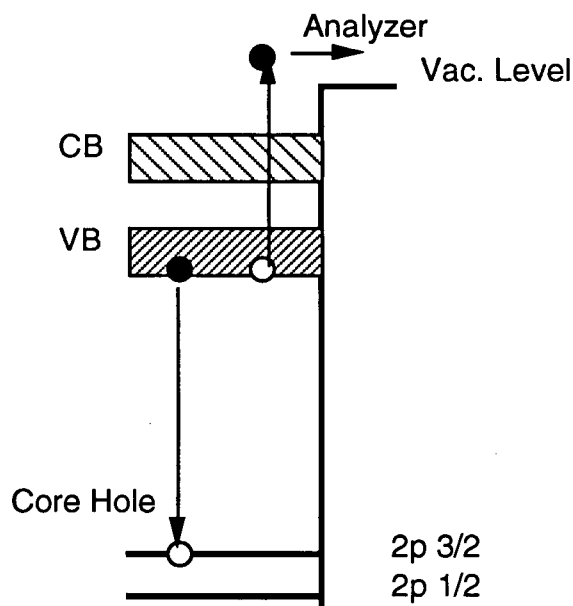


Figure 7: Schematic diagram of the LVV Auger electron spectroscopy process.

During the photoemission experiments we can also measure the energy of the emitted Auger electrons. A schematic diagram of the LVV Auger electron spectroscopy (AES) process is shown in Fig. 7. In the LVV Auger process a Si 2p core hole is filled by an electron from the Si valence band. To fulfill the requirement of conservation of energy an electron is also ejected from the valence band. The kinetic energy of this Auger electron is given by

$$E_A = E_B(2p) + \phi_a - E_B(\text{VB}) \quad (8)$$

where $E_B(2p)$ is the binding energy of the 2p core level and $E_B(VB)$ is the binding energy of the valence band. The kinetic energy of the LVV Auger electron is independent of the photon energy that produces the initial core hole but will be sensitive to any changes in the valence band when Si is made porous.

After preparation PS samples are introduced immediately into a load lock with less than five minutes exposure to room air. The loadlock is pumped down to 7×10^{-8} torr, then the sample is transported with a magnetic transfer arm into the manipulator in the main analysis chamber. The main chamber is maintained at a base pressure of 5×10^{-10} torr. PS samples are mounted on a 1 inch square stainless steel sample block which can accept the threaded rod on the end of the transfer arm. Samples to be annealed are mounted in a Ta foil basket spot-welded to Ta wires which are screwed down to the stainless steel sample block as shown in Fig. 8. The Ta wires can be resistively heated.

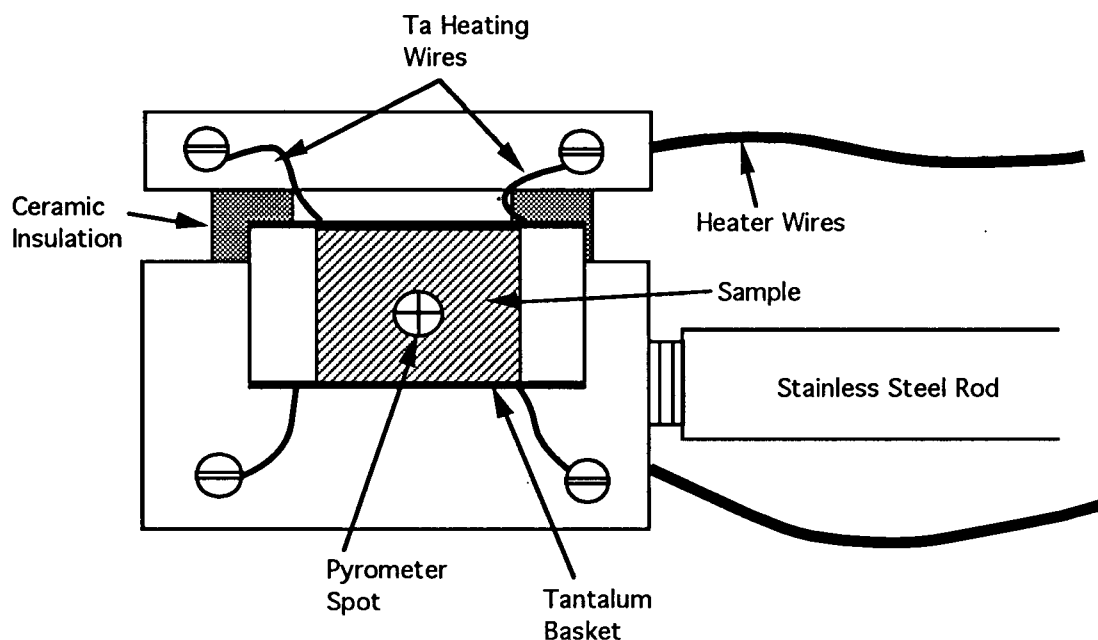


Figure 8: Diagram of a the heatable stainless steel sample holder.

Approximately 20 W power applied to the heater wires would bring the sample to 600°C. The temperature of the sample was measured with an IRCON infrared pyrometer and a type-K chromel-alumel thermocouple in contact with the front surface of the sample. The limits on the range of the temperature measurement resulted from two effects. Firstly, the pyrometer was only sensitive to temperature above 500°C. Secondly, it was not always possible to have the thermocouple in contact with the sample. Therefore temperatures below 500°C could not always be measured directly. To overcome this problem the temperature of the wafer was determined as a function of the power supplied to the Ta heating wires. The resulting calibration curve shown in Fig. 9 could be used to determine the sample temperature when it could not be measured directly. Temperature measured in this manner were found to be accurate to within $\pm 30^\circ\text{C}$. Note in Fig. 9 we also plot the measured pyrometer temperatures as a function of the heating power.

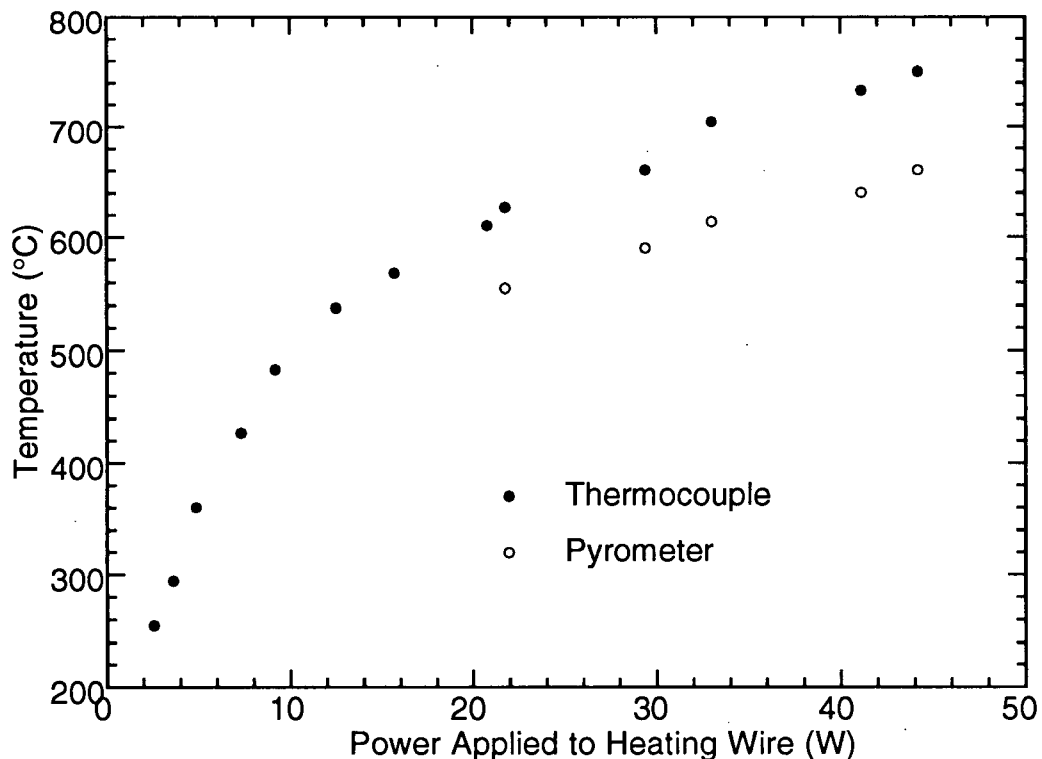


Figure 9: Sample temperature as measured by the type-K chromel-alumel thermocouple and an IRCON pyrometer as a function of power applied to the Ta heating wires.

The pyrometer temperature could then be calibrated with the type-K thermocouple measurements.

Once in the manipulator the sample can be rotated for direct line of sight to the mass spectrometer for monitoring of desorption during annealing experiments or lowered to carry out photoemission measurements with the hemispherical electron energy analyzer or x-ray absorption with the microchannel plate detector. The samples were positioned at a 45° angle to the incident photon flux in all photoelectron experiments. We are able to measure both electron yield and photoemission simultaneously without moving the sample.

The optical bandgap of PS was measured by the bulk sensitive photoluminescence (PL) technique. PL is a bulk probe because the emitted photons are being measured rather than the inherently surface sensitive electron measured in the photoelectron spectroscopes. The PL spectra were obtained at room temperature with the samples in a flowing nitrogen ambient and at 4K with samples immersed in liquid He. The samples measured at room temperature were held in a flowing nitrogen ambient to maintain a stable PL emission intensity during the time period of the measurement. A rapid drop in PL intensity was observed if the PS sample was exposed to air during the measurement presumably due to oxidation of the PS. The PL was excited with the 457 nm line from an Ar ion laser and the emission was detected with a Bomem interferometer equipped with a room temperature silicon photodiode detector and a liquid nitrogen cooled InGaAs detector. The PL spectra are normalized to correct for the spectral dependence of the throughput of the interferometer, which was calibrated with a halogen lamp, (assumed to be a black body radiator at 3300 K) incident on a white surface in the sample holder position. After preparation PS samples were exposed to air for time periods ranging from a few minutes up to an hour before the PL measurements were made.

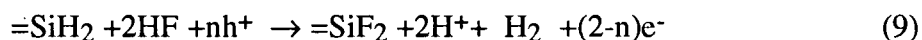
Information about the PS microstructure was obtained by double crystal x-ray diffraction. The purpose of double crystal diffraction is to study the fine detail of a single Bragg peak rather than scan over all peaks as in a normal $\theta/2\theta$ scan. A BEDE model 200 double crystal diffractometer with a Rigaku rotating anode copper x-ray source was used in the x-ray diffraction

experiments. In order to achieve the resolution needed to study the Bragg peaks at high resolution, well collimated and monochromatic x-rays are needed. The collimator consists of a perfect silicon crystal into which a channel is cut to give two parallel 220 surfaces. The beam emerging from the collimator has undergone two successive Bragg reflections and is hence well conditioned in angle. It is not however conditioned in wavelength and still contains both the copper $K\alpha_1$ and $K\alpha_2$ components. To monochromate the beam it must be Bragg reflected off a third crystal with a high wavelength dispersion reflection. After the monochromator crystal the x-ray beam is incident on the specimen. In our case a Si (111) crystal was used as a monochromator. This gives a diffraction peak with a minimum half width of 12 arcseconds from a crystalline silicon sample.

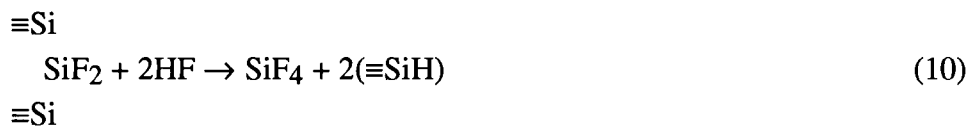
3. PREPARATION OF POROUS SILICON

3.1 ELECTROCHEMICAL PREPARATION OF POROUS SILICON

Bulk crystalline Si can be made highly porous by partial electrochemical dissolution in hydrofluoric-acid (HF) based electrolytes. The dissolution process follows an interfacial two electron transfer through an overall electrochemical reaction involving HF molecules ^{3,28},



where $\equiv\text{SiH}_2$ represents a surface Si atom terminated with hydrogen as shown in Fig.1 section 1. For the case of p-type silicon the reaction may proceed entirely with holes ($n=2$). For n-type silicon in the dark, where the dissolution occurs under reverse bias, the etching current density during pore formation may exceed the saturation current due to limiting hole flux by many orders of magnitude, and the participation of electrons injected into the conduction band ($n<2$) is expected. The divalent silicon species is oxidized to tetravalent silicon in the form of SiF_6^{-2} ions through a two step reaction.



After the reaction the silicon surface is again terminated with hydrogen.

Porous silicon films are fabricated using the apparatus shown schematically in Fig. 10. The electrochemical reaction is carried out in a cylindrical container formed by pressing the front surface of the silicon sample against an O-ring on the bottom of a Teflon reaction cell containing

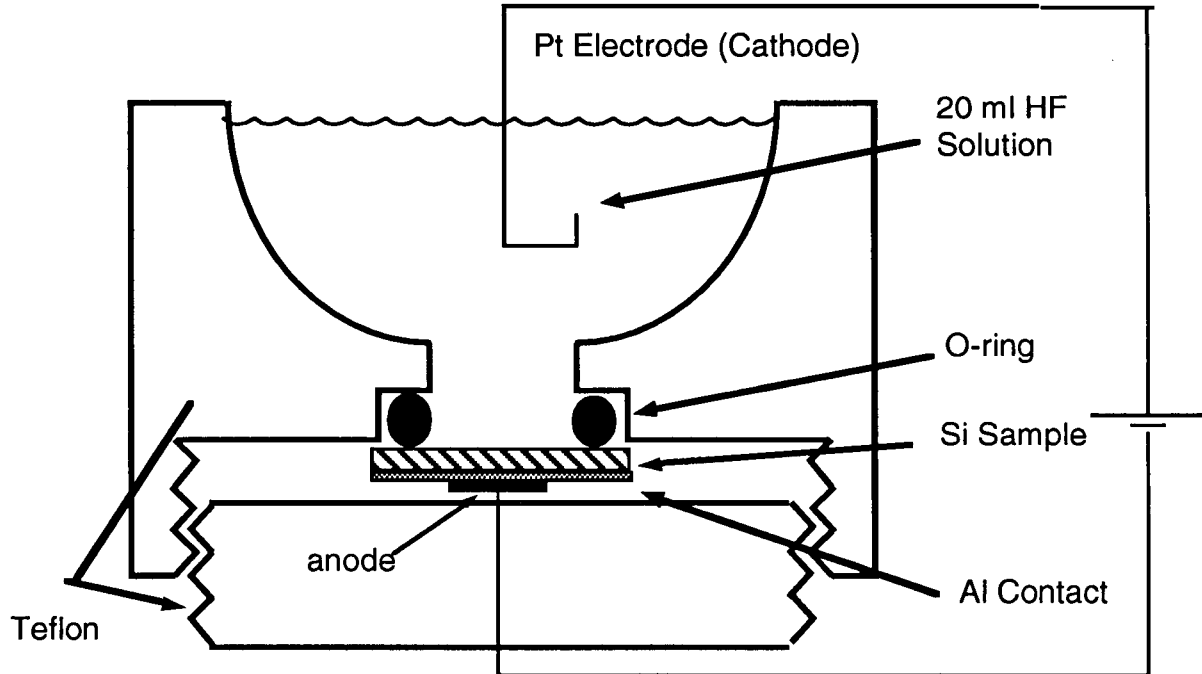


Figure 10: Apparatus for the fabrication of porous silicon films.

approximately 50ml of HF etching solution. The bottom of the reaction cell was threaded so a second piece of Teflon could be screwed in to maintain pressure on the silicon to prevent leakage of the HF etching solution around the O-ring. A wire was fed through a hole drilled in the center of the bottom Teflon piece to make contact between the silicon and the external circuit. The size of the PS sample could be varied with interchangeable reaction cells with O-ring diameters ranging from 0.8 to 2.5 cm diameter. Uniform electrical contact was made to the silicon through an ohmic back contact of either aluminum deposited by evaporation and annealed in vacuum at 500°C or a Ga-Al alloy deposited on the back of the wafer as follows. To make an ohmic contact molten Ga was painted on the back of the wafer then mechanically scratched into the surface with an Al rod. Scratching was necessary to penetrate the surface oxide layer. The metal contact ensured an even

current flow in the wafer and a more uniform porous layer. A platinum wire suspended in the etching solution, was used as the cathode in the electrochemical cell. Anodization was carried out at a constant potential difference of 2 to 5 V between the Pt wire and the back of the silicon substrate. The Pt wire was negative with respect to the silicon. In all cases the electrochemical reaction was carried out at room temperature and pressure. The microstructure of PS depends strongly on the anodization conditions such as HF concentration and current density also on the dopant type and their concentration in the bulk silicon starting material. We explain how each of the above mentioned conditions affects the anodization reaction.

3.1.1 Electrolyte

The electrolyte used in the anodization reaction consisted of a mix of concentrated hydrofluoric acid, ethanol and deionized water (HF:H₂O:EtOH). Concentrated HF consists of 48% by weight hydrogen fluoride gas dissolved in deionized water. By decreasing the ratio of HF to EtOH:H₂O in the electrolyte one could change the etching reaction from stable pore growth to electropolishing of the silicon surface. To produce uniform PS films it was necessary to include EtOH in the electrolyte due to the hydrophobic properties of the PS.²⁹ Purely aqueous solutions do not penetrate the pores of the PS film. Also H₂ gas produced during the etching reaction will stick to the PS surface leading to non-uniform growth. Ethanol is thought to wet the PS surface and promote both the infiltration of the electrolyte into the pore and the evolution of H₂ gas from the surface and hence increase the rate of pore growth.

After anodization PS samples continue to etch slowly in the HF solution even when the external potential is removed. The chemical etch of the PS material is thought to be caused by oxidation of the PS by H₂O followed by attack of the SiO₂ by HF. The chemical etch rate in HF solutions depends strongly on the concentration of ethanol. Since PS is highly hydrophobic, ethanol allows the HF solution to infiltrate the pores; if ethanol is not added the chemical etch rate is very slow and confined to the surface.²⁹ In the etch process the PS surfaces are passivated with

hydrogen but if the sample is exposed to air the surface oxidizes on a time scale of 15 minutes. To avoid oxidation after processing, the PS samples are removed from the etching solution, rinsed in ethanol, blown dry with nitrogen and then immediately loaded into the UHV chamber for analysis.

3.1.2 Current Density

The current was supplied to the electrochemical cell with either a Keithley model 220 programmable current source or a current-limited Topward power supply. During anodization a constant potential difference ranging from 2 to 5 V was applied between the Pt wire and the back of the silicon substrate, with the Pt wire negative with respect to the silicon. The applied voltage varied from sample to sample depending on the doping concentration and the quality of the metal back contact. The current density was adjusted directly with the current source or in the case of n-type material by the intensity of the illumination as discussed in the next section. At high current densities above about $100\text{mA}/\text{cm}^2$ the etching reaction changes from pore growth to electropolishing.

The surface morphology produced in the electrochemical reaction depends on whether charge supply or mass transport is the rate limiting step. For low current densities the reaction is limited by charge supply from the electrode and for high current densities the reaction is limited by mass transport through the electrolyte. For a flat silicon anode the transition from charge supply limited process to a ionic diffusion limited process is characterized by a specific current density we will call J_{ps} .⁷ If the diffusion of chemical reactants in the electrolyte is the rate limiting step holes will accumulate at the electrode surface and HF is depleted from the electrode surface. Hills on the electrode dissolve faster than depressions because they are more exposed to the electrolyte. As a result the surface becomes smoother an effect known as electropolishing of the surface. For $J < J_{ps}$ the reverse is true and holes are depleted and HF accumulates at the surface of the electrode.

The PS film can be separated from the silicon substrate by reducing the HF concentration or increasing the current density at the end of the preparation process to cause electropolishing at

the bottom of the pores.³⁰ Self supporting PS membranes have also been formed by growth of the pores completely through the thickness of the silicon wafer.³¹ The time T_c at which the propagating pores reached the backside of the wafer was determined by a sharp rise in the electrode potential and by the presence of electrolyte leaking through the wafer. Knowing the thickness of the Si wafer and measuring T_c we estimate the rate of pore growth as a function of anodization conditions. The growth rate of the PS film is dependent on the doping concentration and the current density as shown in Table 1.

Silicon Substrate	Current Density (mA/cm ²)	Rate of PS layer formation (nm/s)
p-type 0.005 ohm-cm	25	18
p-type 0.005 ohm-cm	50	42
p-type 0.005 ohm-cm	100	69
p-type 10 ohm-cm	30	10
n-type 0.01 ohm-cm	50	49

Table 1. Rate of PS formation as a function of current density. Silicon wafers were $525 \pm 20 \mu\text{m}$, electrolyte was 1:1:2 HF:H₂O:EtOH in all cases.

PS samples initially etched at low current densities ($\approx 1 \text{ mA/cm}^2$) exhibit interference colors with increasing thickness similar to SiO₂ films on Si. In particular while etching under white light the samples appeared brown, blue, clear (silicon colour) and yellow, then the cycle repeats itself. After approximately 5 minutes the color of the PS film remains constant. Depending on the starting material and anodization conditions the final color of the PS films ranged from blue-gray to yellow. A table of the final colour of the PS films made from p-type Si as a function of doping density HF concentration and etching current density is given below:

Resistivity of Si wafer (ohm-cm)	Current Density mA/cm ²	Electrolyte (HF:H ₂ O:EtOH)	Color
10	10	1:1:2	light brown-tan
10	30	1:1:2	green-yellow
10	80	1:1:2	yellow
10	10	1:0:1	dark brown
10	30	1:0:1	light brown
10	80	1:0:1	brown
0.005	10	1:0:1	blue-gray
0.005	30	1:1:2	dark-brown
0.005	100	1:1:2	dull-red

Table 2 Final PS colour as a function of anodization conditions for samples made from boron doped Si (100). All samples were conditioned at an etch rate of 1mA/cm² for 5 mins. before a growth etch for 15 mins. at the stated current density.

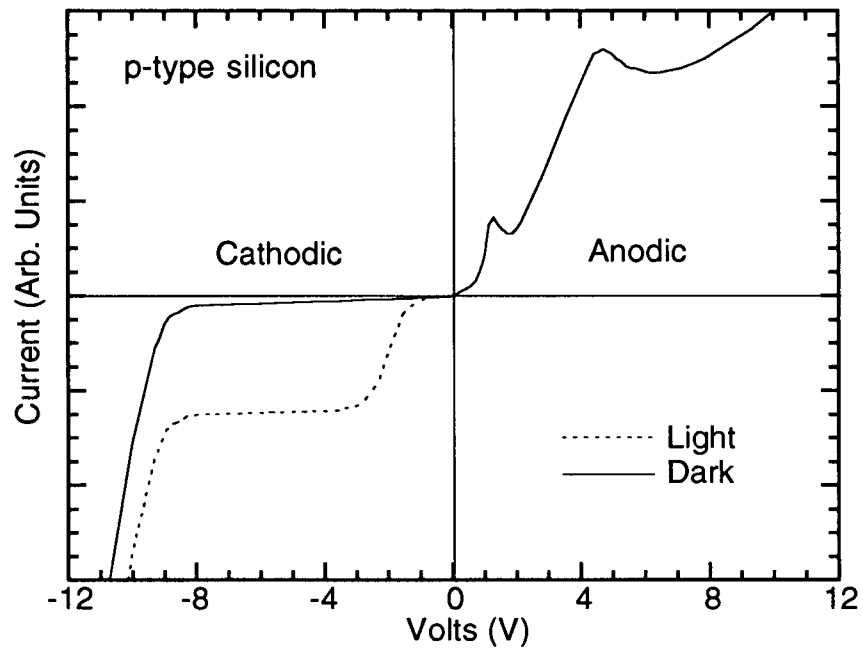
3.1.3 Doping Type of Silicon Substrate

Holes are minority carriers in n-type silicon therefore etching in hydrofluoric acid electrolyte under normal anodic bias is very slow. Hole generation can be enhanced in the n-type material if the electrode is illuminated or the applied bias is increased until the breakdown field is reached. Breakdown occurs in silicon for an electric field strength of 3×10^5 V/cm.⁷ High doping density or sharp pore tips in the anode surface lower the required bias for breakdown. PS samples prepared from n-type Si by electrical breakdown were found to be nonuniformly etched, with etching confined to a few isolated spots on the surface. From the point of view of etching, n-type silicon under illumination behaves much like p-type silicon. The n-type sample preparation carried

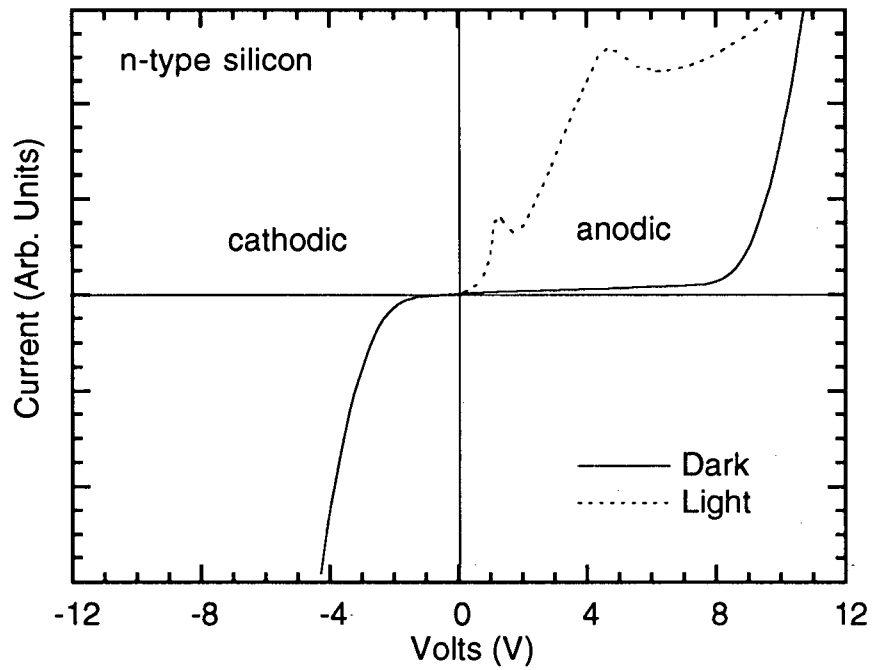
out under illumination produced very uniform material. Etching was carried out by illuminating the sample in the electrochemical cell by a 30 watt halogen lamp from a microscope illuminator. The samples were initially conditioned at a light intensity sufficient to produce a current of 0.8 mA/cm^2 , for 5 minutes to start uniform pore growth. This was followed by a growth etch in which the current was raised by increasing the light intensity by variable amounts. The intensity of the light was changed with neutral density filters. The maximum wavelength of light incident on the sample could also be adjusted by inserting colour glass filters between the lamp and the sample.

For heavily doped n-type substrates no breakdown or illumination is necessary to generate a dissolution current. In this case charge transfer occurs via tunneling of electrons through the narrow barrier region at the silicon-electrolyte interface. Therefore anodization can be achieved without illumination at low bias voltages. The anodization reaction was typically conducted in the dark on p-type silicon since these substrates are only weakly light sensitive during etching. For all doping types the PS growth was initiated with a conditioning phase followed by a growth phase as described above.

Figures 11(a) and (b) show the typical I-V curves for n and p-type silicon in aqueous HF solution in the dark and under illumination.³²⁻³⁴ The I-V curves are similar to the normal Schottky diode behavior expected from a semiconductor electrolyte interface. Under cathodic polarization the silicon is stable and does not dissolve yet hydrogen gas is liberated due to reduction of water at the silicon electrode. Under anodic polarization the silicon electrode dissolves. Since n and p-type silicon substrates are different in their electronic properties not their chemistry, the I-V plots for illuminated n-type substrates are identical to that of p-type substrates. The anodic dissolution portion of the I-V curve shown in Fig. 11 (c) can be divided into three distinct regions.^{32,34} Pore formation takes place in region A. At anodic potentials above the first current maximum, region C, the silicon substrate electropolishes. In region B a transition zone exists where pore formation and electropolishing compete. A second current maximum is observed in the electropolishing region of the I-V curves. This feature is thought to be due to growth of an insulating anodic oxide on the silicon electrode.³²

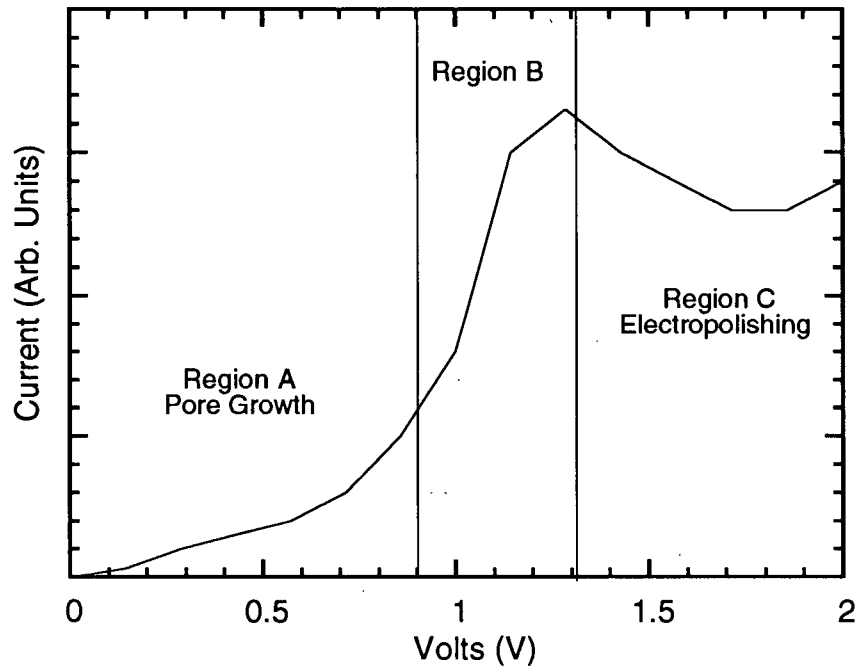


(a)



(b)

Figure 11(a,b): Typical I-V relationships for n-type (a) and p-type silicon (b).³⁴ The solid line indicates the dark response and the dashed line indicates the response under illumination.



(c)

Figure 11(c): Anodic I-V relationship for silicon in HF solution showing the three regions of dissolution. The scales on the graphs are arbitrary because both depend strongly on doping type and concentration of the Si substrate and anodization conditions.

3.2 CHEMICAL PREPARATION OF POROUS SILICON

Stain films on Si wafers produced by chemical treatments with solutions of HF:HNO₃:H₂O were first observed over 30 years ago.³⁵ These films are believed to be similar structurally to the anodically produced PS films.³⁶ In the etching of silicon by the stain etch method, the oxidation reaction chemistry is thought to be the same as that of anodic oxidation, where the electron acceptor is a chemical species such as HNO₃. Stain etch films were produced using a 4:1:5 volume solution of HF:HNO₃:H₂O. The reagents were 49% HF, 70% HNO₃ and deionized water. In the electrochemical reaction holes are supplied by the external power supply. In the chemical preparation holes are produced by the reduction of NO₂ on the sample surface. The reaction is autocatalytic in that the reaction products promote the reaction itself.³⁷ It proceeds in the presence of HNO₂, as shown



The etching process is limited by the first step in the above reaction. The second step of the reaction proceeds in the presence of the silicon surface. Here the anode reaction is given by:



Hydrofluoric acid dissolves this SiO₂. The reaction is given by



The overall reaction is then:



The process is activation limited by the presence of HNO_2 at the surface which causes a delay of several minutes after immersion of the sample and the staining reaction. The process is accelerated by priming the etch solution with HNO_2 . This is achieved by immersing a piece of Si for 1 minute into the concentrated $\text{HF}:\text{HNO}_3$ solution prior to adding water.³⁸ A vigorous reaction occurs and the Si rapidly dissolves with the emission of heat and a yellowish gas thought to be NO_2 . Si substrates were stain etched in primed $\text{HF}:\text{HNO}_3:\text{H}_2\text{O}$ solutions between 1-30 minutes. The rate of reaction was found to depend on the composition of the solution and the doping of the Si sample. Stain etch films etched for 15 minutes on heavily doped p-type substrates were about 1.5 μm thick and black in appearance. Stain films etched for the same time on lightly p-doped material were about 0.25 μm thick and exhibited various interference colors after etching. The rate of growth of the PS films was found to decrease with time and for a particular set of conditions a limiting thickness was eventually achieved. This behaviour is consistent with previous studies.³⁶

3.3 PREPARATION OF SILOXENE

Siloxene is easily prepared by a reaction of CaSi_2 with HCl , originally described by Wöhler³⁹ in 1863 and later refined by Kautsky.⁴⁰ CaSi_2 consists of alternating Ca layers and Si (111) planes, in which the Si-Si bond distance is the same as in crystalline Si. The Ca-layers are removed by a chemical reaction with HCl , where the remaining Si-dangling bonds are saturated with H and OH radicals as shown in Fig.12(c). Other structural models for siloxene have also been proposed shown in Fig. 12 (a,b), in which the oxygen atoms are incorporated into the silicon sheets to form linear chains of Si interconnected with oxygen, or silicon rings interconnected with oxygen bridges. ^{12,13} However these two structures have been eliminated as possible forms of siloxene by recent x-ray diffraction work.^{41,42} Only the structure shown in Fig. 12(c) is ever observed in the x-ray diffraction data.

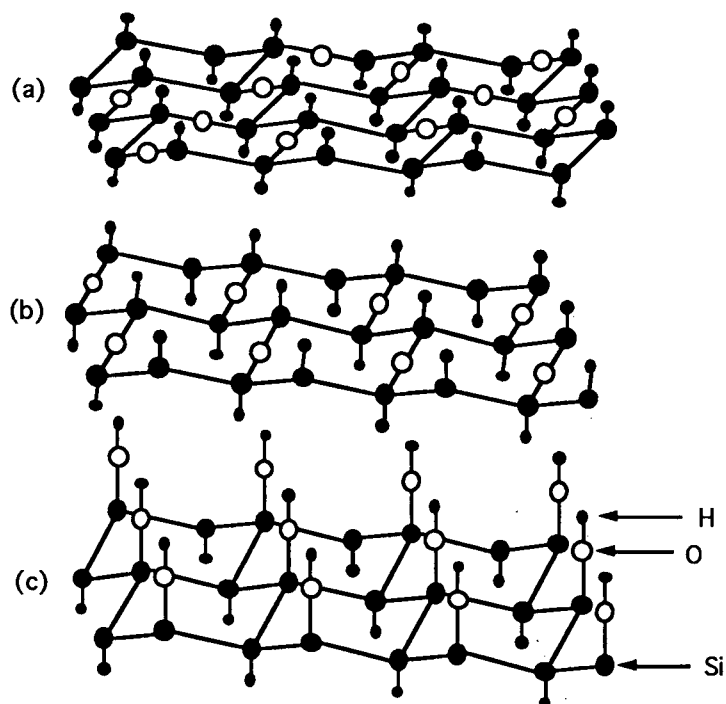


Figure 12: Structural models for siloxene consisting of: (a) silicon rings interconnected by oxygen bridges, (b) linear silicon chains interconnected by oxygen, (c) Si (111) planes terminated with alternating H and OH radicals.

The siloxene samples were prepared by slowly adding aqueous hydrochloric acid (37%) to powdered CaSi_2 (Aldrich). Reactions were carried out at room temperature in a darkened room. After mixing for approximately 30 minutes the yellow siloxene was filter rinsed with cold ethanol and vacuum dried until a base pressure of 100 mtorr was reached. Typically this took 4-6 hours. Samples were then recovered in an argon filled glove box and stored in an opaque vial under an argon atmosphere. Siloxene samples that were allowed to sit in room air would oxidize over a period of a few hours.^{41,42}

A second type of siloxene sample was prepared at 0°C under nitrogen, recovered by filtering and rinsed in concentrated HF, and then vacuum dried.⁴¹ Siloxene prepared in this manner was found to combust spontaneously upon exposure to air, so it must be handled without air exposure. After the drying step, the samples were transferred to the UHV chamber for analysis. The powder x-ray diffraction pattern of this sample is consistent with oxygen free siloxene (Si_6H_6) which we call layered polysilane.⁴² The layer polysilane appeared greenish in color.

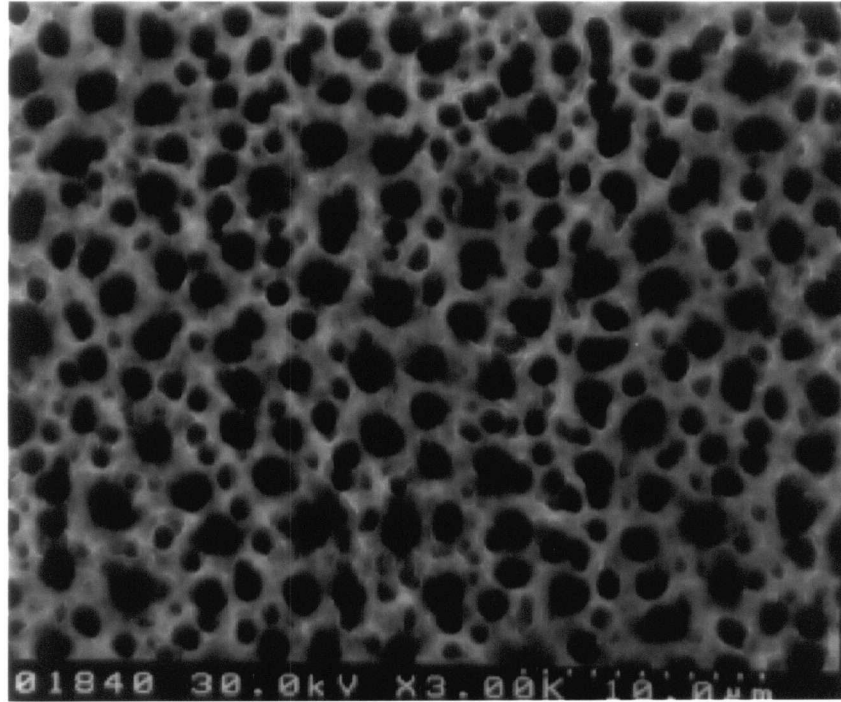
Some of the siloxene sample prepared at 0°C was transferred while damp to a stainless steel tube furnace which was connected both to a roughing pump and an argon flow. The sample was first vacuum dried and then heated to 400°C for 90 mins. then cooled to room temperature both under flowing argon. This sample was called heat treated siloxene.⁴¹ The sample was red-brown in color and was air stable.

4. MICROSTRUCTURE OF POROUS SILICON

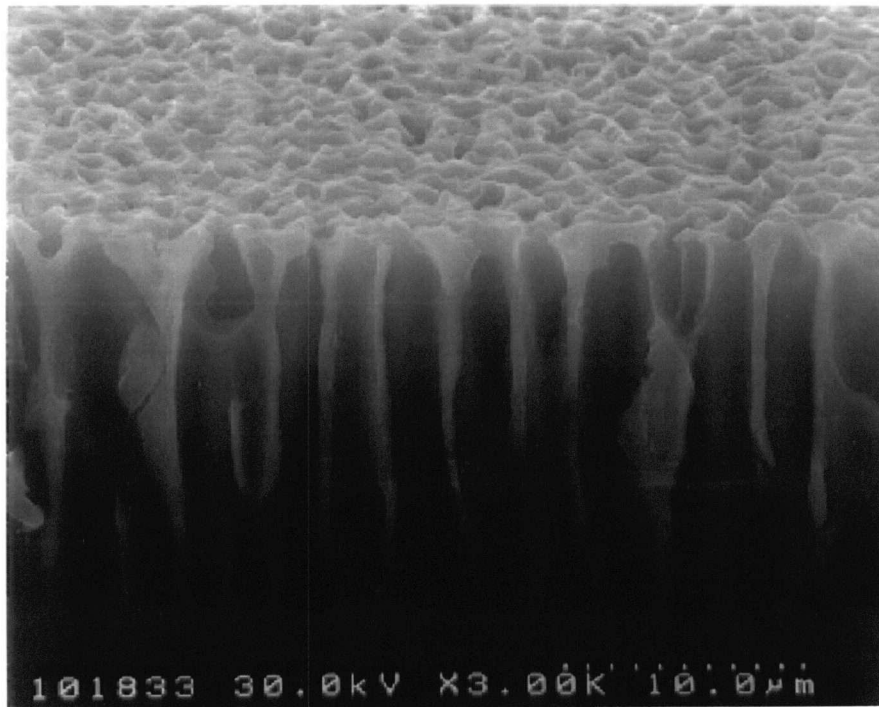
Recently a two phase model for the microstructure of PS has been proposed, in which there is a nanoporous layer responsible for the visible luminescence on the surface of a macroporous silicon backbone.⁷ Previous studies have established that porous silicon retains at least some of the crystalline structure of the substrate. We can examine the PS micro structure in terms of the two phase model using scanning electron microscopy and double crystal x-ray diffraction measurements on PS near the Si (400) diffraction peak.

4.1 SCANNING ELECTRON MICROSCOPY

We use field emission SEM to examine the PS microstructure on length scales down to 50 nm. SEM photomicrographs of the surface and cross section of a PS film made from lightly doped p-type silicon (100) etched at 12 mA/cm² for 20 mins. are shown in Fig.13. In cross section the porous structure is characterized by randomly spaced, parallel sided pores oriented in the (100) direction with a pore diameter of about 1.5 μm . The pore diameter at the surface is smaller, between 0.5-1.0 μm , but enlarges to 1.5 μm over the first micron of pore growth. The change in pore size is associated with the transition from pore initiation to stable pore propagation. It is interesting to note that the size of the remaining silicon in the pore walls is on the order of 0.5 micron, much too large for any quantum confinement effects. In Fig.14 we show the SEM photomicrographs for PS made from p+ silicon (100) etched at 65 mA/cm² for 90 minutes. In the heavily doped silicon the pore diameters are at least a factor of 10 smaller than for the p-type material. The pores are approximately 100 nm in diameter, oriented in the (100) direction. In addition there are numerous budding side branches seen on the pore walls. Generally, an increase in the pore diameter accompanies an increase in the anodization current density

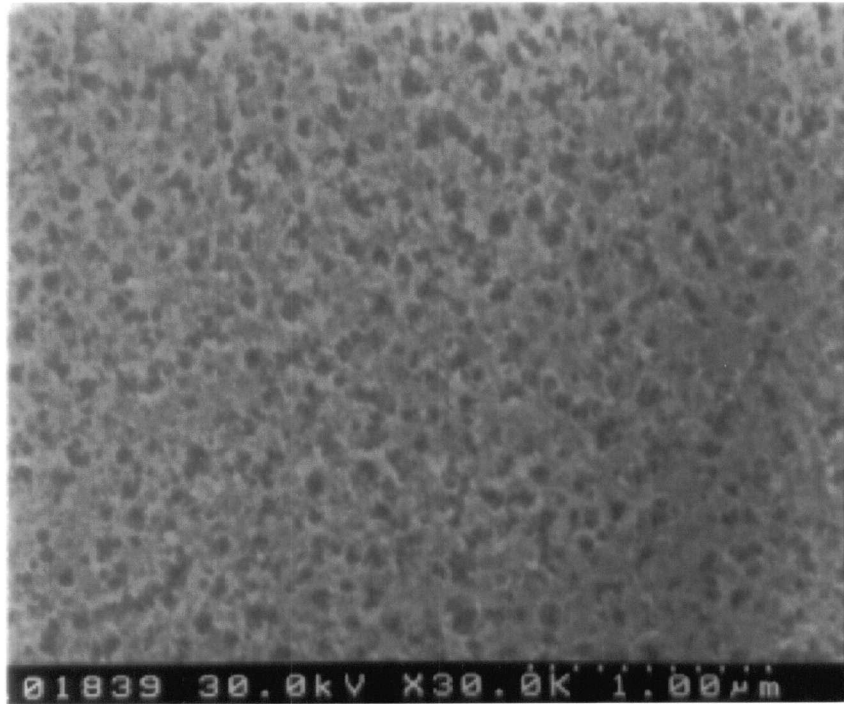


(a)

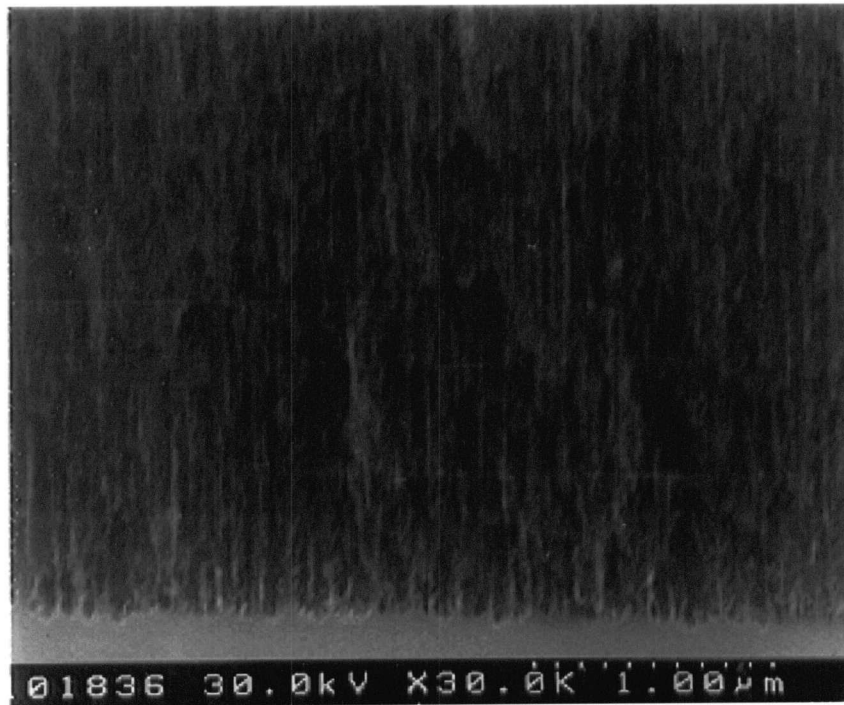


(b)

Figure 13: SEM photomicrographs of the surface (a) and the cross section (b) of a PS film grown from p-type 100 silicon etched at 12 mA/cm^2 for 20 mins. Note dotted line bottom right corner of the pictures is 10 microns.



(a)



(b)

Figure 14: SEM photomicrographs of the surface (a) and the cross section (b) of a PS film grown from p+ type 100 silicon etched at 65 mA/cm^2 for 90 mins. Note dotted line bottom right corner of the pictures is 1 micron.

for both heavily and lightly doped silicon. The pore structure for the n+ material is virtually identical to the p+ material suggesting that the mechanism for pore formation is the same in heavily doped silicon.

Recent SEM³⁴ and transmission electron microscopy (TEM)⁴³ studies revealed that the pores selectively propagate in the <100> direction independent of anodization conditions or the crystallographic orientation of the silicon substrate. One possible explanation can be obtained from the PS formation mechanism.^{7,28,34} In the first step of the dissolution process Si-F bonds replace surface Si-H bonds with the consumption of one charge carrier per bond. The polarization effects of the F weaken the Si-Si backbonds so they can be attacked by HF or H₂O. For the (100) surface two F atoms are polarizing two Si backbonds compared to the (111) surface where one F is polarizing three Si backbonds or the (110) surface where one F atom on average is polarizing two Si backbonds. The attack of the Si backbonds will be easier and therefore faster on the (100) surface.

The microstructure of PS films of different doping density has also been studied by many groups using cross sectional TEM.^{5,34,43-46} For PS films formed on p+ (100) silicon the pore sizes on the order of 20 nm and interpore spacing of 10nm have been observed in the TEM micrographs.^{5,34,43} The TEM micrographs for p-type silicon show that both the pore diameters and the interpore spacing are extremely small, generally between 1 and 5 nm, with a highly interconnected and homogeneous pore network.^{34,45} Raman spectroscopy, on PS made from p-type silicon, provides additional evidence for the existence of microstructures on the order of 2-3 nm in size.^{46,47} Structures of this size can not be resolved with the SEM. These results suggest that there is a coexistence of two distinct pore sizes which differ by three orders of magnitude. To avoid ambiguity we call the larger pores observed in the SEM "macropores", and we call the smaller pores observed in the TEM "nanopores". Presumably the macropore walls observed in the SEM photomicrographs must have a nanoporous surface layer. Similar results have been observed in the microstructure of n-type silicon in which the macropore walls are covered with a nanoporous silicon layer that was up to 0.5 microns in depth.^{7,22}

4.2 X-RAY DIFFRACTION

Double crystal x-ray diffraction measurements on p+ doped PS near the Si (400) diffraction line typically show two narrow diffraction peaks, one corresponding to the bulk Si substrate and one to the porous material as shown in Fig.15. The crystalline silicon peak shown in Fig.15, has a full width at half maximum of about 16 arcsec, and the FWHM of the porous peak is 21 arcsec.

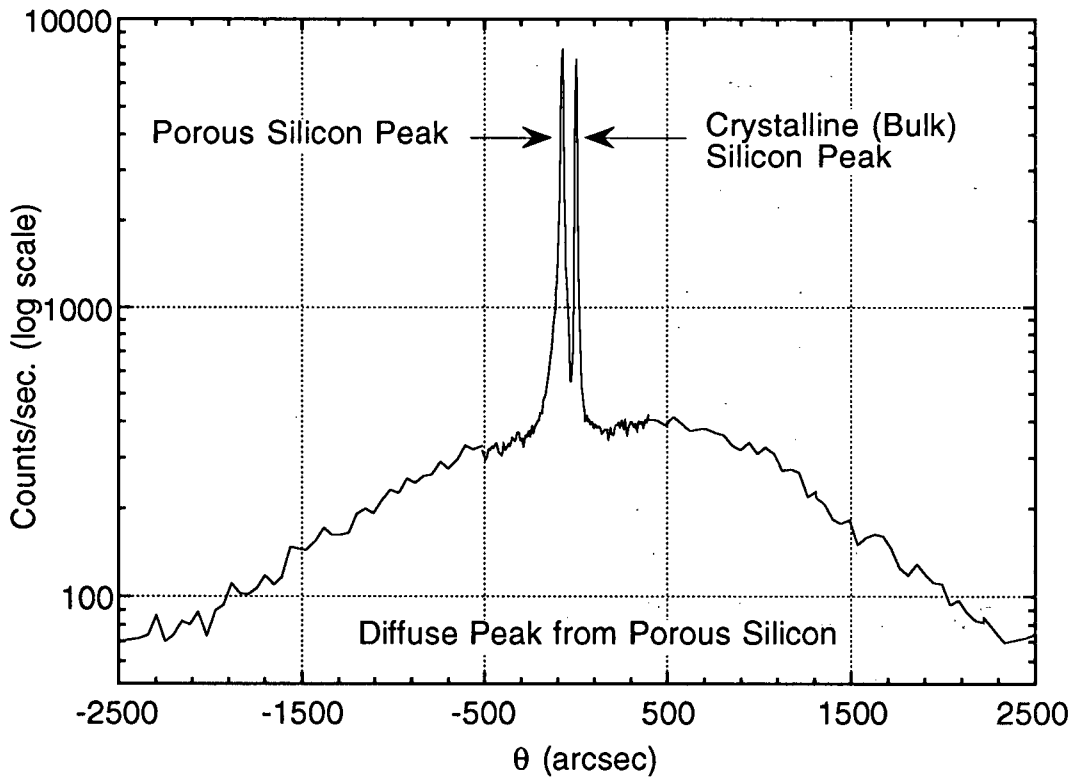


Figure 15: X-ray rocking curve for PS. Zero θ has been set at the zero position for the bulk Si peak. This sample was made from a $\langle 100 \rangle$ p+ silicon wafer by anodization at 15 mA/cm^2 for 75 mins.

The two narrow peaks are separated by approximately 70 arcsec. The angular separation between the two Bragg peaks corresponds to a lattice parameter increases on the order of $\Delta d/d = 5 \times 10^{-4}$ along the [001] direction perpendicular to the sample surface. By measurement of the asymmetric

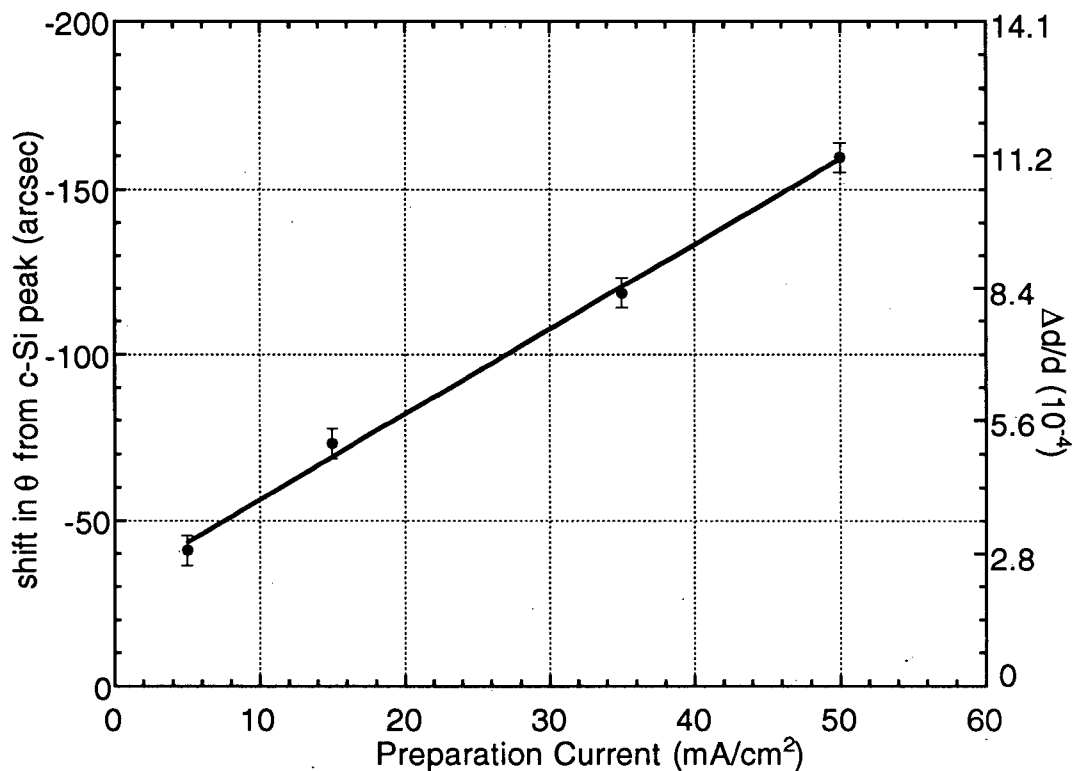


Figure 16: Porous silicon peak shift (to the left of the c-Si peak) as a function of anodization current density. Shift in terms of $\Delta d/d$ change in lattice parameter is also given.

(224) reflection other groups have shown that there is no change of the lattice parameter parallel to the interface.⁴⁸ These observations have led to the conclusion that the PS layer is tetragonally distorted.⁴⁹ We attribute the narrow PS diffraction peak to the relatively large scale silicon macrostructure seen in the SEM photomicrographs. For p+ and n+ -type PS the angular shift of the narrow PS peak from the crystalline silicon peak was found to be a linearly increasing function of anodization current as shown in Fig.16. This plot also shows the $\Delta d/d$ lattice expansion values associated with the angular shifts. The differentiated form of the Bragg equation was used to derive the relative difference in lattice spacing between the porous silicon and the substrate, $\Delta d/d$

$$\frac{\Delta d}{d} = -\cot\theta \cdot \Delta\theta \quad (19)$$

where θ is the Bragg angle and $\Delta\theta$ is the angular separation of the PS and Si Bragg peaks. The increasing angular separation with current is due to increasing strain associated with a smaller macrostructure. The PS peak becomes broader and less intense and eventually disappears as the angular separation increases, most likely due to a loss in coherence as the size of the backbone decreases. The PS Bragg peak was only observed in p-type PS samples prepared at current densities less than 25 mA/cm². The lattice parameter increase of a p-type PS sample prepared at a current density of 15 mA/cm² was found to be $\Delta d/d = 18 \times 10^{-4}$. This value is about four times larger than that obtained on a p+ -type sample prepared at the same anodization current density.

In addition to the sharp PS peak in Fig.15, there is a broad diffuse peak associated with the PS.^{48,50} An estimate of the diameter of spherical nanocrystallites can be obtained from the broadening of x-ray diffraction lines using the Scherrer equation,⁵¹

$$L = \frac{\lambda}{2\cos\theta_0} \frac{0.9}{\omega} \quad (20)$$

where L is the diameter of the crystallites, λ is the x-ray wavelength (1.54Å), θ_0 is the Bragg angle (34.59°) and ω is the FWHM of the diffraction peak. The width of the diffuse PS peak in Fig.15 is approximately 2900 arcsec. which corresponds to silicon structures on the order of 59 Å in diameter. Other groups measuring the width of the diffuse x-ray peak from p+ PS, have reported structures 120Å in size.⁴⁸

Diffraction peak broadening can also be caused by lattice plane misorientations in deformed regions of the PS. Triple axis x-ray reciprocal space mapping of p+ PS has shown that the diffuse peak is not due to deformation in the PS layer.⁵² The effect of surface stress in the crystallites could also cause a broadening in the diffraction peak and at this point can not completely ruled out. In fact, the asymmetric nature of the diffuse peak may be evidence for a surface stress effect. Although the stress needed to explain the diffuse peak completely would suggest a change in lattice constant on the order of $\Delta d/d = 0.1$, which is in excess of the mechanical limit for bulk silicon.⁵³

The width of the diffuse PS peak has also been measured as a function of anodization current. In Fig. 17 we plot the width of the PS peak at half maximum and the corresponding particle size as calculated by equation 19 as a function of anodization current.

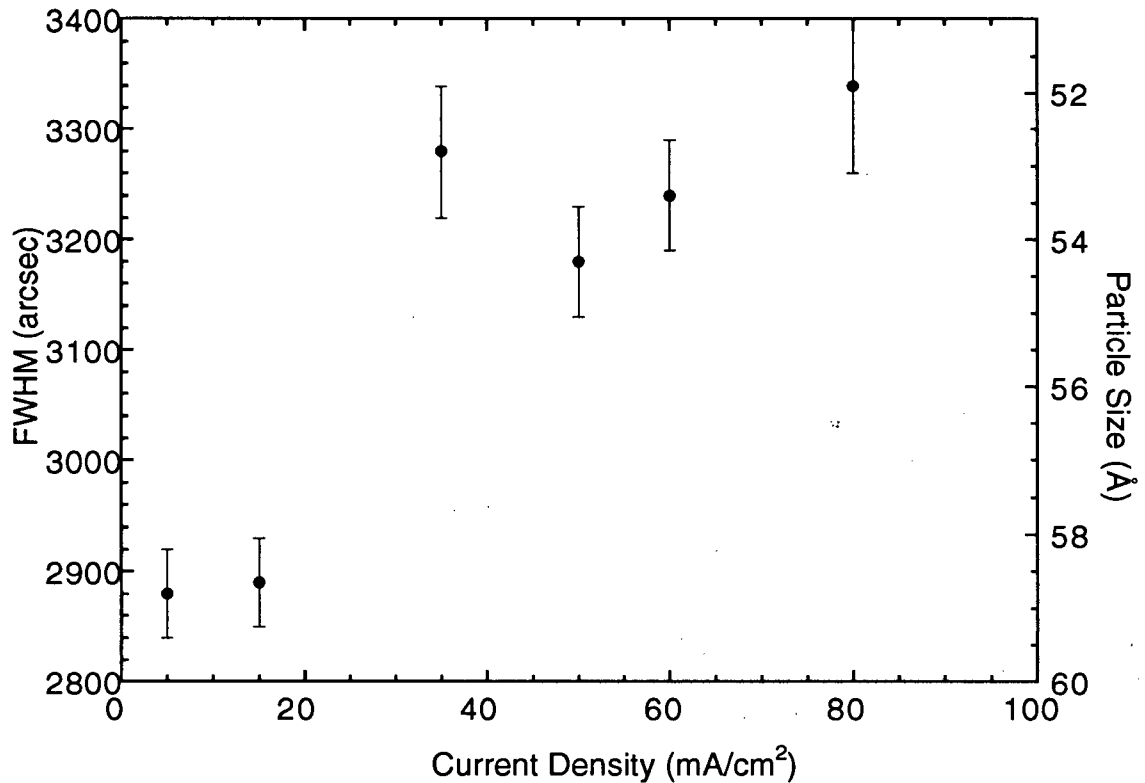


Figure 17: Full width at half maximum of the diffuse PS peak as a function of anodization current. The particle size determined from equation 19 is plotted on the right hand axis.

The overall trend shown Fig. 17 is that the half width increases with anodization current. The diffuse PS peak indicates that the silicon nanostructure is getting smaller with increasing current but not changing dramatically in size. The diffuse peak, although less intense has been measured in p-type PS. For a p-type sample etched at 20 mA the width of the diffuse peak is approximately 6000 arcsec, which corresponds crystallites 32 Å in diameter, similar to values obtained by Raman spectroscopy^{46,47} TEM⁴⁵, and small angle scattering.⁵⁴

We attribute this diffuse peak to the nanostructure which is presumably responsible for the photoluminescence. In the two phase model this nanostructure is thought to be a nanoporous layer on the surface of a macroporous silicon backbone. This nanoporous layer will be the part of the material that the photoelectron spectroscopy measurements are sensitive to.

We model the change in the conduction band energy due to quantum confinement using a square three dimensional box oriented $\langle 100 \rangle$ relative to the silicon lattice.

$$\Delta E_c = \frac{\hbar^2 \pi^2}{2 L^2} \left(\frac{2}{m_t^*} + \frac{1}{m_l^*} \right) \quad (21)$$

If L is 59 \AA and m_t and m_l are the transverse and longitudinal effective masses in bulk Si ($0.2 m_0$, and $1.0 m_0$ respectively) we find the shift in the conduction band edge due to confinement to be equal to $\Delta E_c = 0.10 \text{ eV}$. For $L = 32 \text{ \AA}$ the shift in the conduction band edge due to confinement is $\Delta E_c = 0.33 \text{ eV}$.

The conduction band shift measured by the x-ray absorption on p+ type PS samples prepared under similar conditions as the samples in Fig.17 is shown later in Fig. 26 of Chap. 5. We find the shifts in the XAS for a p+ sample prepared at 15 mA/cm^2 to be $0.08 \pm 0.03 \text{ eV}$ and for the p type sample prepared at 10 mA/cm^2 to be $0.25 \pm 0.03 \text{ eV}$, in remarkably good agreement with the values inferred from the x-ray data and the effective mass model.

5. PHOTOELECTRON SPECTROSCOPY

5.1 L-EDGE ABSORPTION

Core level XAS provides a method to obtain information on the partial density of states of a selected angular momentum. In fact because of the well defined angular momentum of the core level the K-edge absorption spectrum probes the p-density of states while the L_{2,3} edge probes the s and d density of states. Due to the spin orbit interaction the silicon 2p core level is split into two states separated by 0.61 eV.^{55,56} Thus the L_{2,3} XAS spectrum is a superposition of absorption structure related to transitions from the Si 2p_{3/2} and Si 2p_{1/2} core levels.⁵⁶⁻⁵⁸ The Si L₃ absorption edge due to electron transitions from the Si 2p_{3/2} core level begins at the lower photon energy. Typical Si L_{2,3}-edge absorption spectra for porous and bulk Si are shown in Fig. 18. The bulk silicon sample in Fig. 18 was rinsed in HF immediately before loading into the analysis chamber and as a result has an H-terminated surface. The bulk L_{2,3} spectrum contains structure above the absorption threshold which we label as A, B and C from the Si 2p_{3/2} state and associated structure labeled a, b and c due to transitions from the 0.61eV spin orbit split Si 2p_{1/2} level. This spectrum can be considered a probe of the s-density of empty states since the contribution of the d orbitals in the Si conduction band in the range 0-4 eV above the conduction band minimum (CBM) is small.⁵⁹

In order to interpret the features in the L_{2,3} edge of bulk silicon we compare the spectrum to a L₃ edge calculation of the s-density of states for bulk Si. The s-partial DOS are calculated by Patitsas⁶⁰ using the Si conduction band structure and wavefunctions generated by a LCAO code written by Papaconstantopoulos⁶¹. For simplicity, the dipole matrix element of equation 4 is approximated by a simple overlap of a 3s orbital with the generated wavefunction. Hence this is the s-projection of the DOS. The value of the s-DOS at a given energy is a product of this overlap and the total number of k-states in the Brillouin zone (BZ) over a small energy interval. The calculated L₃ absorption has been Gaussian broadened by 0.15 eV (full width half max.) to

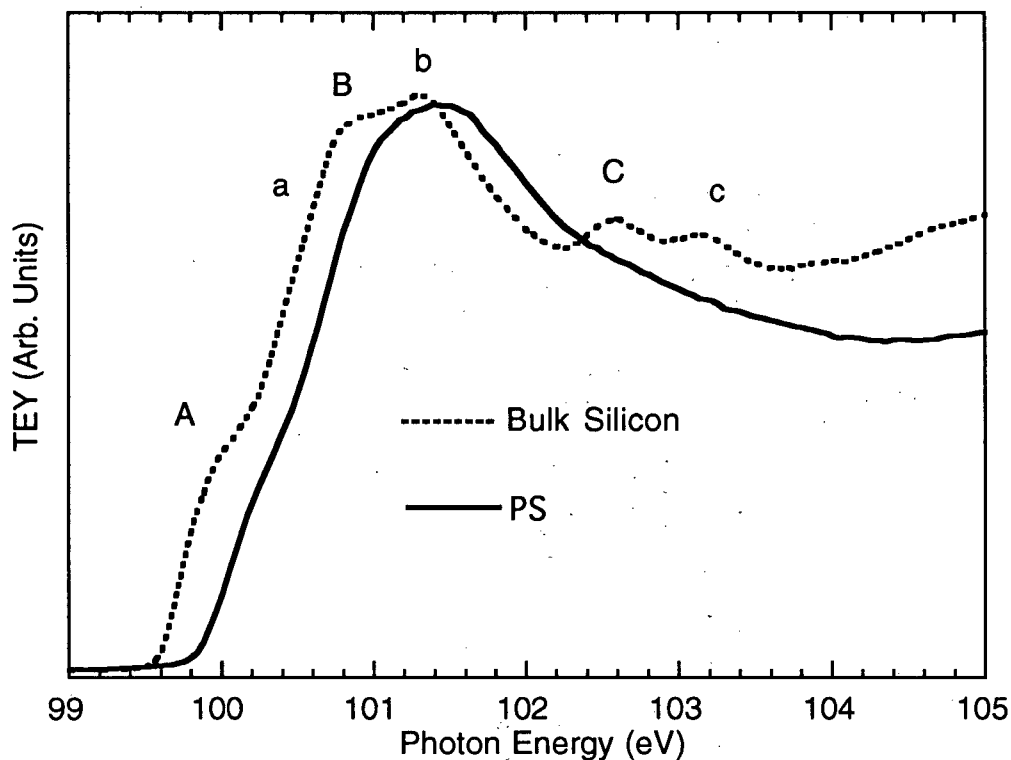


Figure 18: Total electron yield measurements of the absorption of the silicon (100) $L_{2,3}$ edge for bulk Si and a PS sample made from n-type (100) silicon etched for 20 mins. at a current density of 30 mA/cm^2 . The electron yields have been scaled at the edge jump to facilitate comparison.

represent the experimental resolution at the $L_{2,3}$ absorption edge. The bulk s-DOS shown in Fig.19 has the same three peaks A, B and C as observed in the Si L_3 edge. These peaks are associated with maxima in the DOS of bulk Si. Peak A originates from the states near X_1 just above the CBM, peak B is associated with the L_1 point and the weaker C peak comes from the L_3 point.⁵⁹

Notice in Fig. 18 that the L-edge in the PS is shifted by 0.34 eV higher in photon energy relative to the bulk silicon.^{15,16} We attribute the blue shift to quantum confinement which raises the energy of the bottom of the conduction band relative to the Si 2p core level. A blue shift in the Si L-edge attributed to quantum size effects has also been reported in ultrathin hydrogenated

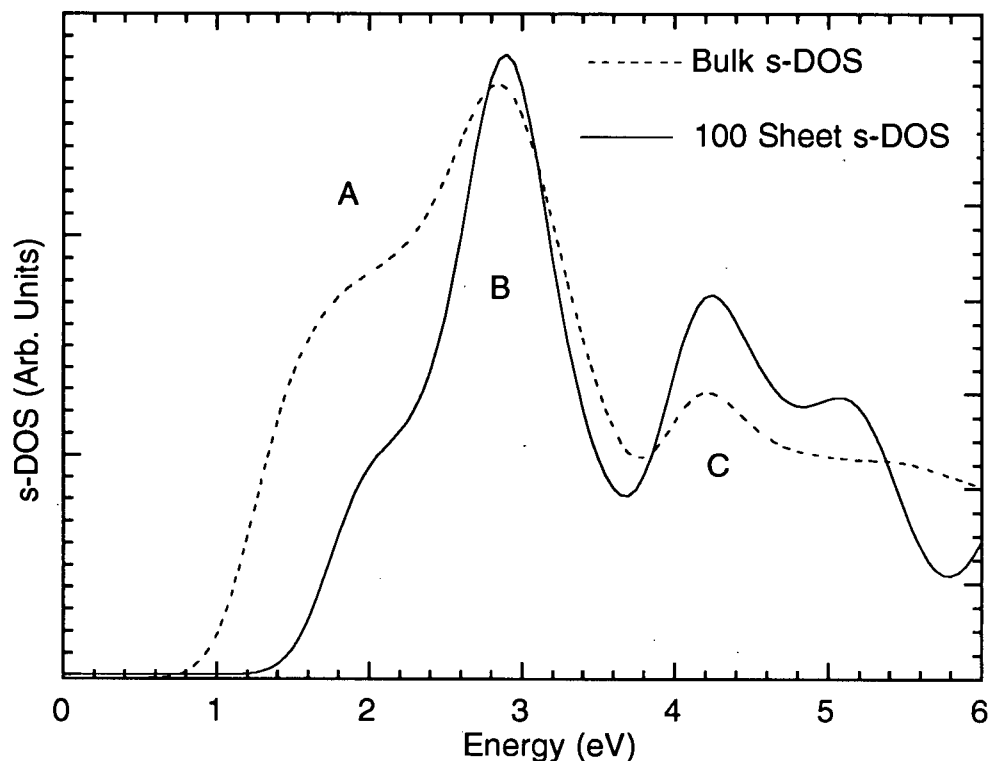


Figure 19: LCAO calculation of the s-density of states at the L_3 edge for bulk Si shown as a dotted line and for a $\langle 100 \rangle$ sheet of Si shown as the solid line. The calculated L_3 edge has been Gaussian broadened by 0.15 eV to represent experimental resolution at the $L_{2,3}$ edge. The zero of energy scale is referenced to the top of the valence band.

amorphous silicon films on silicon oxide⁶² and recently in ultrathin Si/SiO₂ superlattices.⁶³ In addition to a shift to higher energy the double step feature associated with the spin-orbit splitting of the 2p core level, appears to be less pronounced and the crystalline features at B and C are absent in the spectra of the PS.

We attribute this effect to broadening due to a distribution of quantum shifts in the inhomogeneous porous material. In Fig. 56 we model the absorption spectrum of PS with the absorption spectrum of bulk silicon shifted up in energy to simulate the average quantum shift and broadened by convolution with a Gaussian to simulate the distribution of quantum shifts. As shown in Fig. 56 the features at B and C disappear in the model absorption spectrum, in agreement with the actual PS $L_{2,3}$ edge. Alternatively the absence of peaks at B and C may be a consequence

of the core hole potential on the PS conduction band DOS. Effects of the core hole potential on the L-edge absorption are discussed further in section 5.3.

While it is a theoretical challenge to calculate the electronic structure and the absorption spectrum of silicon nanostructures taking different shapes and surface relaxations into account, we believe that the essential physics behind the observed effects can be illustrated by the following simple model: we assume the nanostructure to be $\langle 100 \rangle$ oriented thin silicon sheets. The electron confinement is modeled by restricting the component of the electron wavevector perpendicular to the silicon sheets to certain discrete values that satisfy the boundary conditions for electron standing waves imposed by the confinement in one dimension. The solid line in Fig. 19 was calculated using the LCAO method described above, assuming the nanostructure is the thinnest connected free standing $\langle 100 \rangle$ sheet of passivated Si. The effect of the sheet is incorporated into the calculation by not accepting all the k-points in the BZ as for the bulk Si calculation. Instead the BZ is sampled by two 2-dimensional planes oriented in the $\langle 100 \rangle$ direction cutting through the BZ. In this case the cuts were midway between the Γ and X points. In qualitative agreement with the data the calculated PS L_3 edge is also blue shifted, in this case by approximately 0.55 eV. The absence of inhomogeneous broadening in the PS L_3 calculation leaves the features at B and C intact.

Note the feature at A in the calculated PS L_3 edge is much smaller compared to the bulk L_3 edge. Also this feature is blue shifted but B and C are almost unchanged. The k-space sampling discussed above does not favour the region of the BZ that corresponds to the CBM causing a dramatic decrease in the s-DOS states in this region. Also k-sampling of the region giving A is one sided favouring higher energy since it is at the conduction band minimum. This is not the case for the regions around B and C, which explains why these features do not shift. Therefore it is expected that the peak at A should shift to higher energies as the number of k-states is reduced.

The energy of the L-edge is obtained by extrapolating the linear part of the absorption edge just above the threshold to its intersection with the baseline formed by a linear extrapolation of the pre-edge part of the spectrum. The quantum confinement shift in the L-edge is then defined as the

difference between this extrapolation for the PS, and for the bulk Si reference sample. The quantum shift (ΔE_C) in the L-edge can be measured with an accuracy of about ± 0.03 eV in these experiments. In practice the reference spectrum for bulk Si was obtained simply by moving the sample up or down in the analysis chamber so that the x-ray beam was incident on the un-etched perimeter of the silicon wafer.

Figure 20 shows the L-edge absorption for the same samples over an extended range of photon energy. The absorption edge at 150 eV is the L_1 edge due to transitions from the Si 2s core level up to the empty 3p states in the conduction band. Notice that the L_1 edge is superimposed upon a decreasing portion of a broad maximum which has a peak at 132 eV. The maximum is due to the dipole-allowed transitions from the 2p core level to the 3d levels in the conduction band.^{56,57} The origin of the secondary shoulder at 168 eV is not known but may be an EXAFS feature.

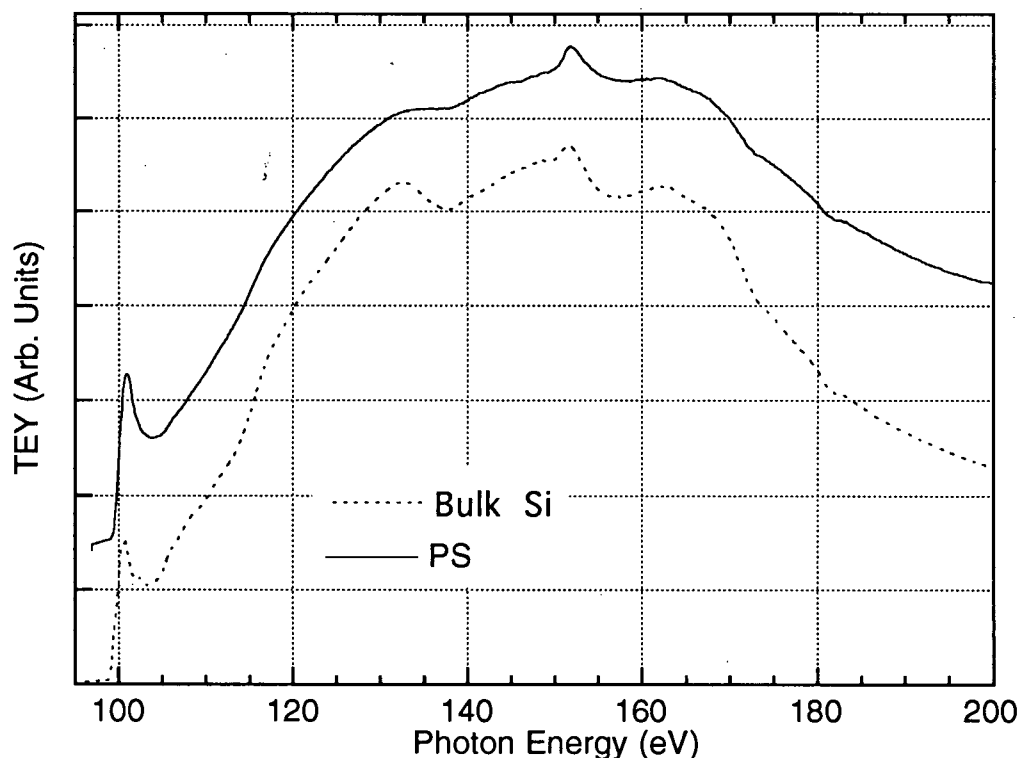


Figure 20: L-edge absorption of bulk silicon and PS over a 100 eV energy range. The electron yields have been scaled at the L_1 edge and then offset to facilitate comparison.

In Fig.21 we show the L_1 edges of Fig.20 on an expanded scale. The peak in the L_1 edge of PS is also shifted to higher energy relative to bulk Si. It is difficult to quantify the quantum shift in the L_1 edge because the shape of the superimposed background also changes when the silicon is made porous. In particular the peak at 132 eV disappears in the PS spectra, which suggests that the d resonance is also affected by the microstructure of the PS. The absorption cross section of the PS just above the L_1 edge is larger than in bulk Si. This could be evidence for an enhanced correlation between the core hole and the final state electron as the dimension of the nanoscale silicon decreases. This effect is also observed in the $L_{2,3}$ edge and is discussed further in section 5.3.

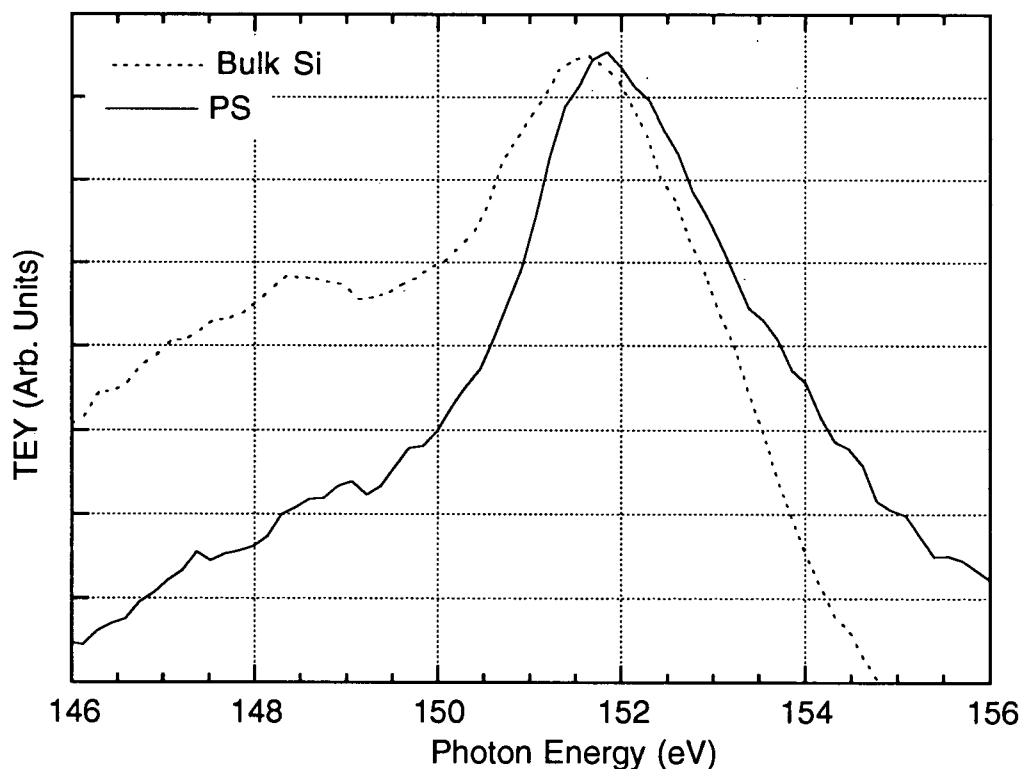


Figure 21: L_1 edge absorption of bulk silicon and PS. The electron yields have been scaled to facilitate comparison.

5.2 K-EDGE ABSORPTION

The K edge absorption also probes the p-states in the conduction band. The K-edge is better suited for detailed measurements of the p-DOS than the L₁-edge, because it is not superimposed on a continuum due to the 2p-3d transitions. In Fig. 22 we compare the Si K-edge absorption spectra for bulk Si and PS prepared in a similar manner as the samples used in the L-edge measurement. The K-edge for bulk Si exhibits structure which we label B' and C'. These peaks occur in the same energy regions as the features B and C in the L-edge. Feature A found just above the threshold in the L-edge of bulk Si is not observed in the K-edge absorption for bulk Si. The absorption onset at the K-edge is a 1.5-2.0 eV broad ramp, which we label A' in Fig. 22.

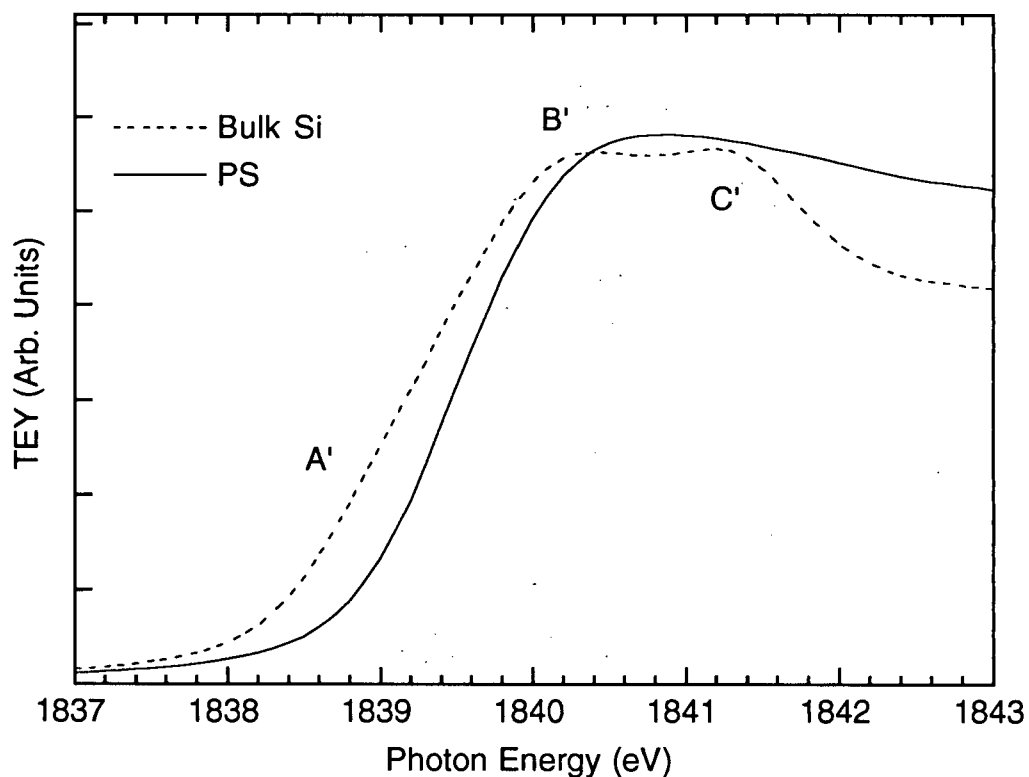


Figure 22: Total electron yield measurements of the absorption of the silicon K edge for bulk Si and a PS sample made from n-type Si $\langle 100 \rangle$, that was etched for 15 mins. at a current density of 35 mA/cm².

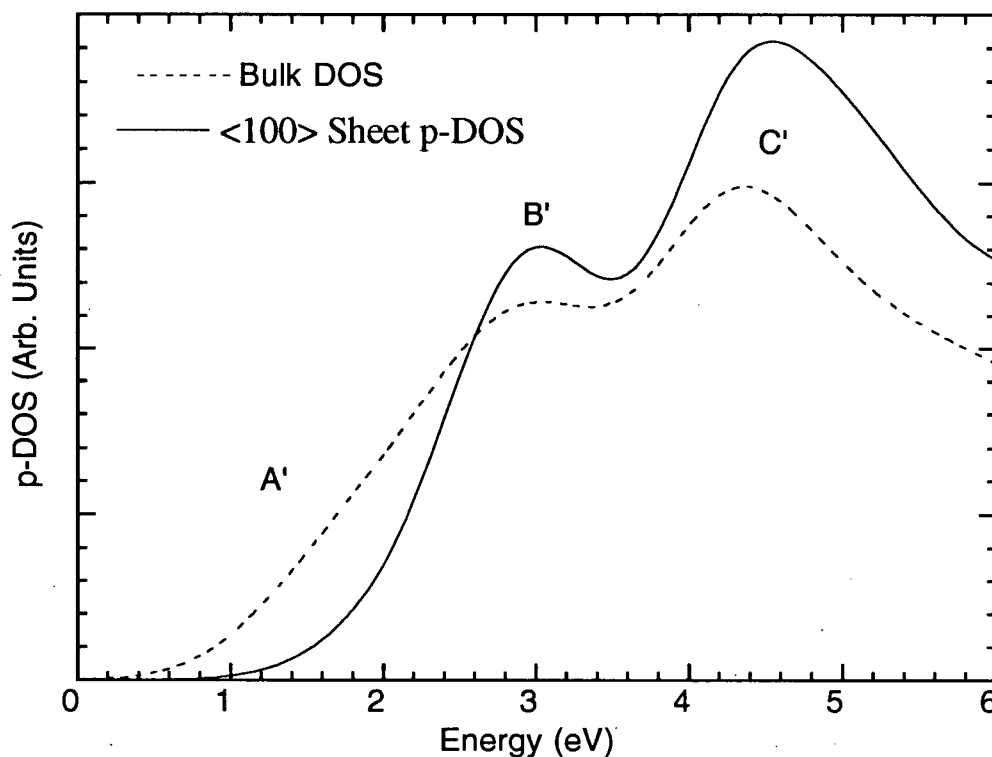


Figure 23: LCAO calculation of the p-density of states in the conduction band for bulk Si shown as a dashed line and for a $\langle 100 \rangle$ sheet of Si shown as the solid line. The zero of energy scale is referenced to the top of the valence band.

In Fig. 23, we plot the calculated p-DOS for the conduction band of bulk silicon and the p-DOS for a single sheet of $\langle 100 \rangle$ silicon. To obtain the p-projection the dipole matrix element from equation 4 is approximated by the overlap of a 3p orbital with the LCAO generated conduction band wavefunction. Evidence that the conduction wavefunctions have primarily p-orbital nature is shown by the fact that the p-projection DOS is very close to the calculated total DOS.⁶¹ The calculated p-DOS is Gaussian broadened by 0.45 eV (FWHM) to represent the experimental resolution at the Si K-edge. The main peaks in the bulk p-DOS are in agreement with the features B' and C' in the K-edge absorption spectrum.

The K-edge for the PS is shifted by 0.4 eV above that of bulk silicon and the features at B' and C' are not visible.^{41,64} Close examination of the absorption edge shows that the K-edge in PS

is actually sharper than in bulk silicon.⁴¹ This is opposite to what was observed in the L-edge of PS, which is thought to be broadened due to an inhomogeneous distribution of sizes. This apparent contradiction can be reconciled by comparing the calculated p-DOS for bulk Si to the p-DOS for a single sheet of <100> silicon as shown in Fig.23. The onset of the p-DOS for the <100> sheet of Si is blue shifted by 0.6 eV and is much sharper compared to the onset of the p-DOS for bulk Si. The reason for this is a combination of the large blue shift and the fact that the feature at B' does not shift since the states contributing to B' are still sampled. We expect inhomogeneous broadening to also affect the K-edge of PS, but in this case it is apparently not the controlling factor.

5.3 EFFECT OF PREPARATION CONDITIONS ON X-RAY ABSORPTION

We find the size of the quantum shift in the $L_{2,3}$ edge (blue shift) depends strongly on the conditions used to prepare the PS. For electrochemically prepared PS, the size of the blue shift depends on the anodization current density, HF concentration, and reaction time as well as conductivity type and dopant concentration in the silicon wafer. Total electron yield measurements of the L-edge show that increasing current densities and post anodization soak times shift the $L_{2,3}$ edge to higher energy as shown in Figs. 24 and 25 respectively. We attribute these spectral shifts to changes in the quantum confinement in the band edges brought about by changes in the microstructure. Figs. 24 and 25 also show that the absorption cross section of the

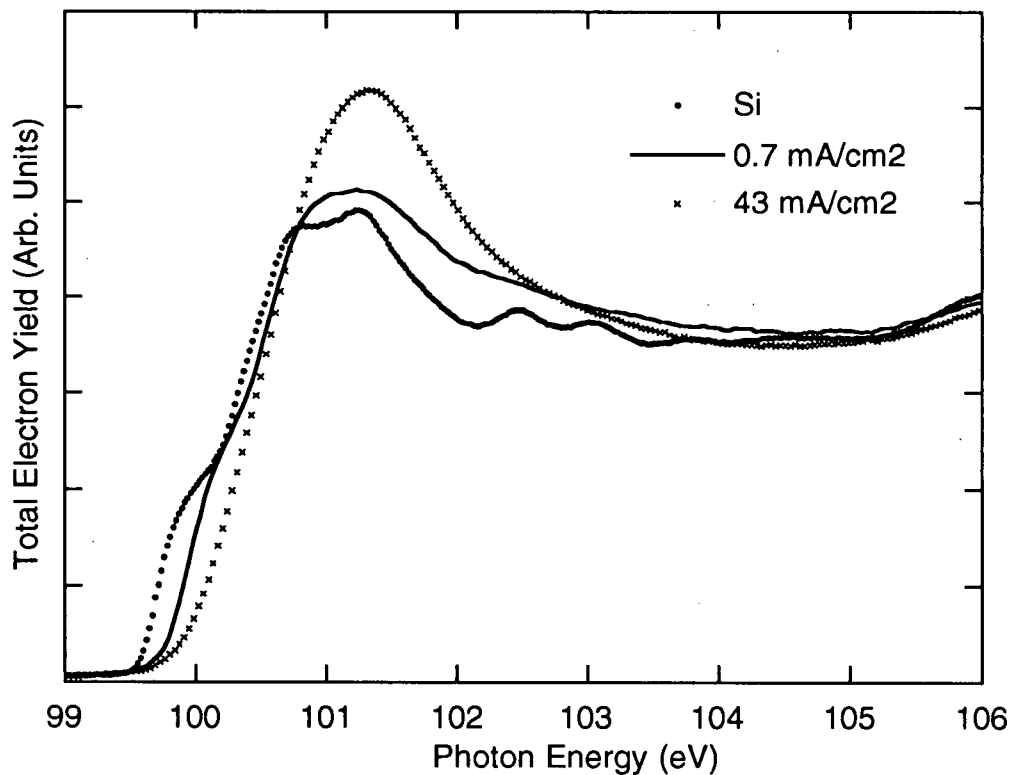


Figure 24: Total electron yield measurements of x-ray absorption at the Si $L_{2,3}$ edge for HF passivated n-type Si (111) (solid dots), and for porous silicon made from n-type Si (111) etched at 0.7 mA/cm^2 (line), and 43 mA/cm^2 (cross).

PS just above the $L_{2,3}$ edge is larger than in bulk Si and that the peak absorption increases with increasing quantum shift in the L-edge, when the spectra are normalized to the same value at 106 eV. (also see Fig. 51 Chap.7) We attribute this effect to enhanced correlation between the core hole and the final state electron as the dimension of the nanoscale silicon decreases.⁶⁵ An electron in the vicinity of a core hole has a larger overlap with the core wavefunction and consequently the absorption intensity is enhanced compared to the delocalized electron. Localization of the states involved in the transition is a well known mechanism for intensity enhancement in XAS. For example, a very strong threshold spike is observed in the L-edge spectrum for silane and disilane

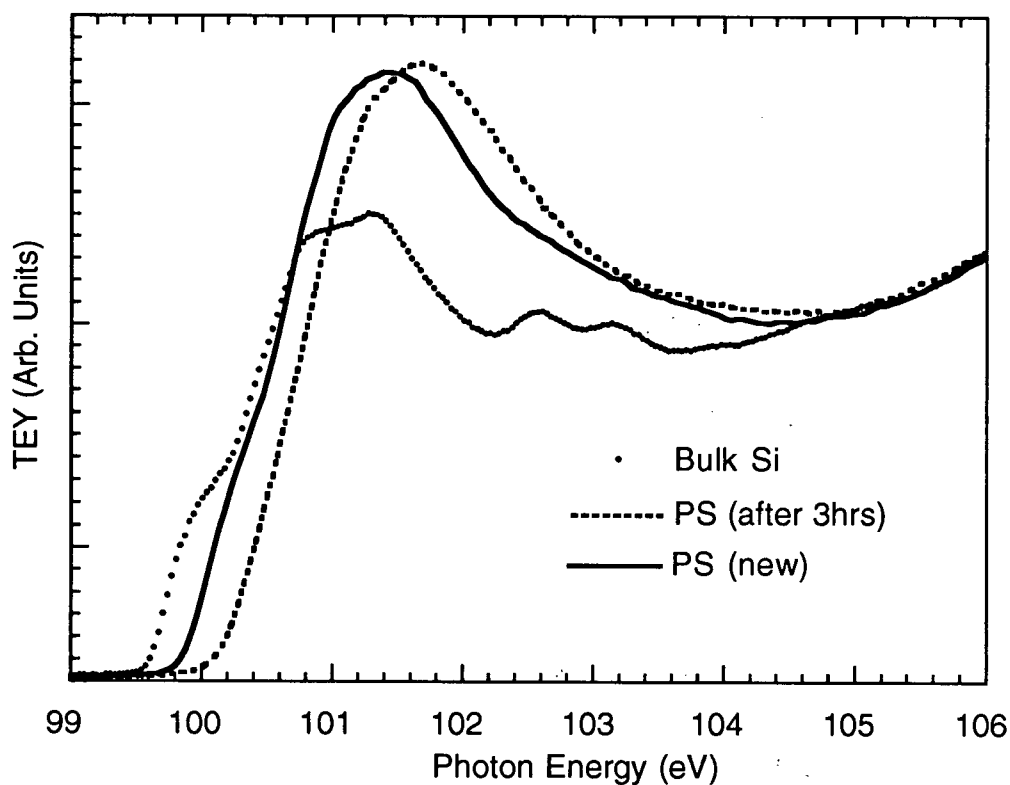


Figure 25: Total electron yield measurements at the Si $L_{2,3}$ edge for HF passivated p-type Si (111) (dotted line), and two types of porous Si. The new PS was prepared by an electrochemical etch of p-type Si (111) in 30% HF in ethanol. Current density was kept constant at 10 mA/cm^2 for 20 min. The Si $L_{2,3}$ edge was measured again on the same PS sample after it has been immersed open circuit in 50% HF/Ethanol for 3 hrs.

gas.^{56,66} From the above argument one would expect the maximum overlap of the excited electron wave function with the 2p core hole in silane molecules. Taken to the molecular limit, this result is consistent with the idea that PS is a form of silicon that is intermediate between bulk and molecular silicon.

In addition the double step feature at the edge associated with the spin orbit splitting of the 2p core level disappears with increasing blue shift.(also see Fig. 51 Chap.7) We attribute the disappearance of the spin orbit feature with an increased inhomogeneous broadening associated with the larger distribution of sizes expected with the increased blue shift. Although the impact of the silicon 2p core potential on the conduction band DOS may also be partially responsible for the disappearance of the spin orbit splitting feature. For example the observed absorption enhancement could cause the spin orbit splitting feature to be washed out.

The structure of the PS is clearly affected by the current density. For example at high current densities or low HF concentration the etching process changes from a stable pore growth regime to an electro-polishing regime. The L-edge of samples made under electro-polishing conditions has no quantum shift and resembles that of bulk silicon. At etching conditions just prior to electropolishing we find the largest shift in the L-edge. In Fig. 26 we plot the shift in the L-edge (ΔE_c) as a function of current density for PS samples made from heavily and lightly doped p-type $\langle 100 \rangle$ silicon etched in a 1:1:2 HF:H₂O:EtOH solution for 25 minutes. In all cases a much smaller L-edge shift is observed in PS made from heavily doped p+ type Si compared to PS prepared from less heavily doped Si. The L-edge shift in the p+ type PS increases with current density up to 35mA/cm² when a maximum shift of 0.12 eV is observed. At higher currents no further shift is noticed. This suggests that there may be a different self-limiting reaction in the PS made from p+ Si since we have to conclude that the nanostructure in the p+ PS is larger than the nanostructure of PS made under the same conditions from p-type material. Recently PS superlattices have been formed by periodically changing the current density during the etch process or by using substrates with layers of alternating doping levels.⁶⁷

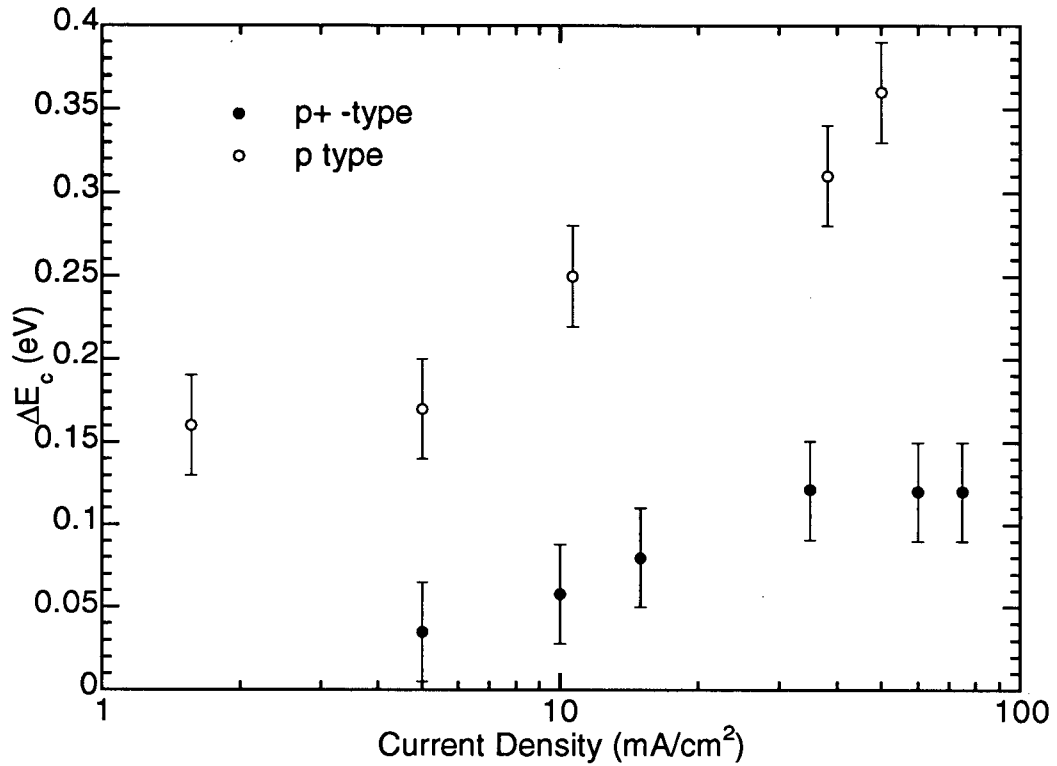


Figure 26: Plot of the conduction band edge shift (L-edge shift) as a function of the current density used to make the PS for two different dopant concentrations in the silicon wafer. The free carrier concentration was 10^{19} cm^{-3} for the p+ type and 10^{17} cm^{-3} for the p-type silicon. Samples were etched in a 1:1:2 HF:H₂O:EtOH solution for 25 minutes.

PS made from heavily doped p-type silicon had L-edge shifts comparable to PS samples prepared under the same anodization conditions from heavily doped n-type silicon. This suggests that PS prepared from heavily doped Si does not depend on the conductivity type. PS samples prepared with the same anodization conditions from either $\langle 111 \rangle$ silicon or $\langle 100 \rangle$ silicon showed no appreciable differences at the L-edge. Therefore we believe the substrate crystal orientation has little effect on the L-edge shift measured in the PS.

Photoluminescence (PL) provides an alternate measurement of the quantum shift. In Fig.27 we plot the color of the PL emission excited by the 488-nm radiation from an Argon laser as a function of HF concentration and current density for PS made from (100) n-type silicon. The

bias voltage was kept at 5 V for all these samples. The PS samples in Fig. 27 can be divided into three distinct categories, judging from the surface appearance and the color of the PL emission. In category 1 the samples are prepared at low current densities or with high HF concentration in the electrolyte. Except for two samples, all PS samples in category 1 are brownish in colour with a PL emission that appears red to the eye. The two exceptions, prepared at both high current density and HF concentration, are black in appearance and do not show visible PL. In category 3 the samples are prepared at high current density or with a low HF concentration.^{34,68} The samples in category 3 are electropolished and appear silver in colour.

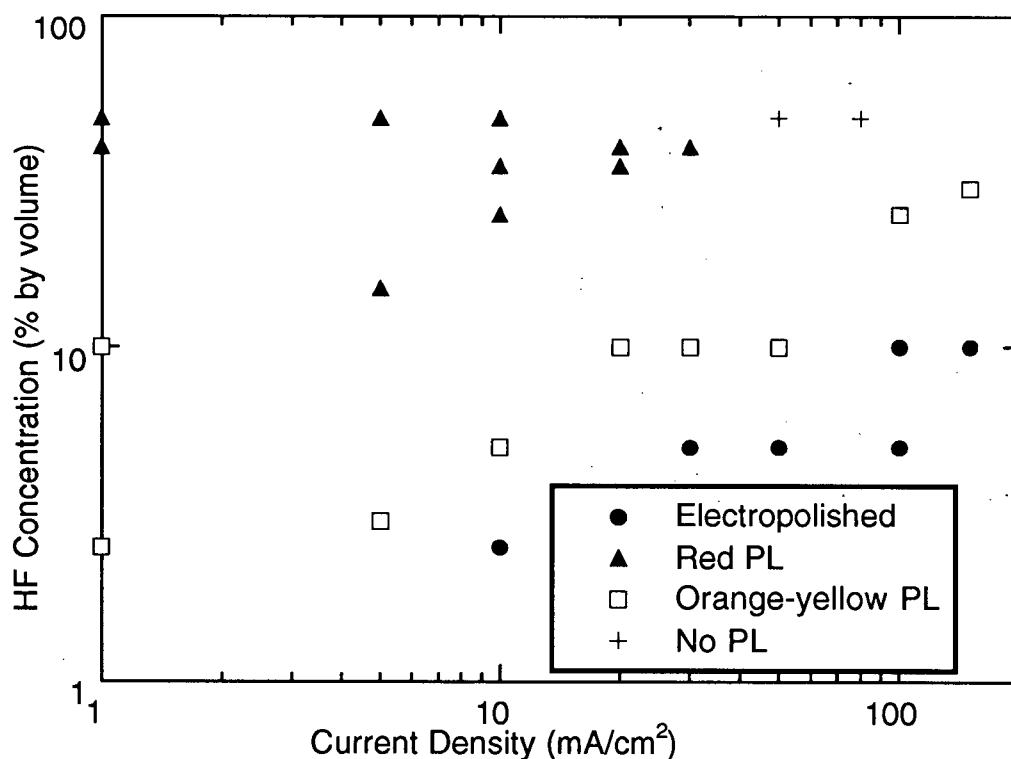


Figure 27: Plot of HF concentration versus current density with PL color detected by the eye as a parameter. PS samples are divided into three categories Red PL, Orange -Yellow PL and electropolishing.

No visible PL emission is observed from these films. The preparation conditions for the PS samples in category 2 are intermediate between the samples in categories 1 and 3. The samples in

category 2 range from tan to gold in color with a PL emission that ranges from orange to yellow-green. These results show that the blue shift observed in both the L-edge absorption and the visible PL increases when the current density during preparation is increased or the HF concentration in the electrolyte is decreased.⁶⁴ The largest blue shift is obtained just below the threshold for electropolishing.

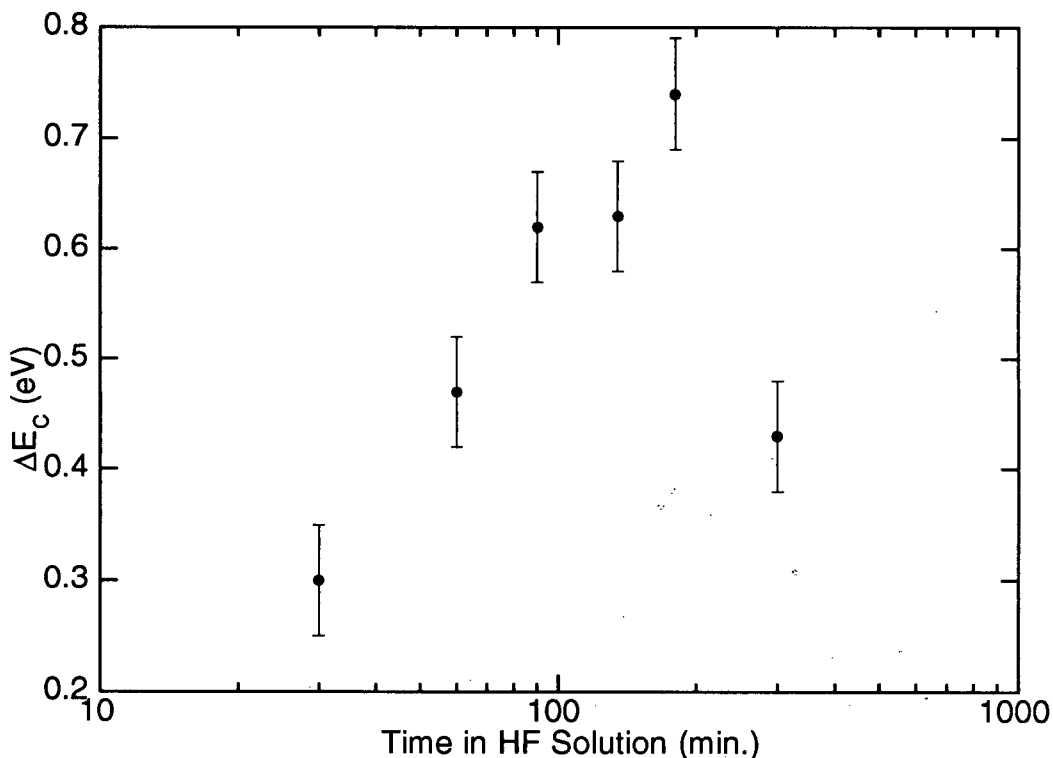


Figure 28: Plot of conduction band shift as a function of the time the porous silicon is soaked in HF solution after anodization. A p-type Si (100) sample was initially anodized in a 50% HF ethanol solution at a constant current density of 20 mA/cm² for 20 minutes. After 5 hours in solution the conduction band begins to shift back toward crystalline silicon. This is interpreted as the onset of complete dissolution of the porous silicon and exposure of the bulk silicon underneath.

Larger quantum shifts are observed for electrochemically etched PS samples that are left open circuit in the HF solution for long periods of time.^{16,69} In Fig. 28 we show the quantum shift as a function of the time spent in a 50%HF:EtOH solution after anodization. The quantum

shift increases with time up to the three hour mark. After this time the quantum shift decreases reverting back to zero, the value for bulk silicon. We interpret this as evidence for a minimum structure size in the porous silicon. Once the minimum size has been obtained, further etching will just cause the sample to decompose. When the sample decomposes, the L-edge broadens and shifts back to the value for bulk silicon because the L-edge spectra starts to include the spectra from the exposed bulk silicon substrate underneath. The dissolution rate of PS in HF depends strongly on the composition of the electrolyte. The L-edge blue shift was much smaller in a PS sample that was soaked for 90 minutes in an aqueous HF solution ($\Delta E_C = 0.15$ eV) compared to a sample soaked for 90 minutes in a 30% HF in ethanol solution ($\Delta E_C = 0.62$ eV). Since PS is highly hydrophobic, ethanol allows the HF solution to infiltrate the pores, if ethanol is not added the chemical etch rate is very slow.²⁹

Large quantum shifts were also obtained in PS samples made by stain etch method. In Fig. 29 we show the L-edges of bulk silicon and stain-etched PS made from p-type Si. The chemical (stain etched) PS samples were reacted in a 4:1:5 solution of HF:HNO₃:H₂O for 2 minutes and 20 minutes. We found that the L-edge of the stain etch PS was shifted to higher energy by 0.71 eV for the 20 minute sample and 0.43 eV for the 2 minute sample. Also we note that the general shape of the stain etch L-edge is similar to that of electrochemical PS. A similar correlation between the quantum shift in the L-edge and the etching time is observed in the electrochemically produced PS as described in chapter 6. Yet unlike electrochemical PS the L-edge blue shift in stain etch PS does not depend strongly on process conditions or conductivity type of the Si substrate. X-ray absorption measurements showed no variation in the position of the L-edge for stain etch PS samples with respect to HF concentration in the etching solution (X:1:5, HF:HNO₃:H₂O solutions where $1 < X < 8$). These results are in agreement with a recent PL studies of stain etched PS.^{38,70}

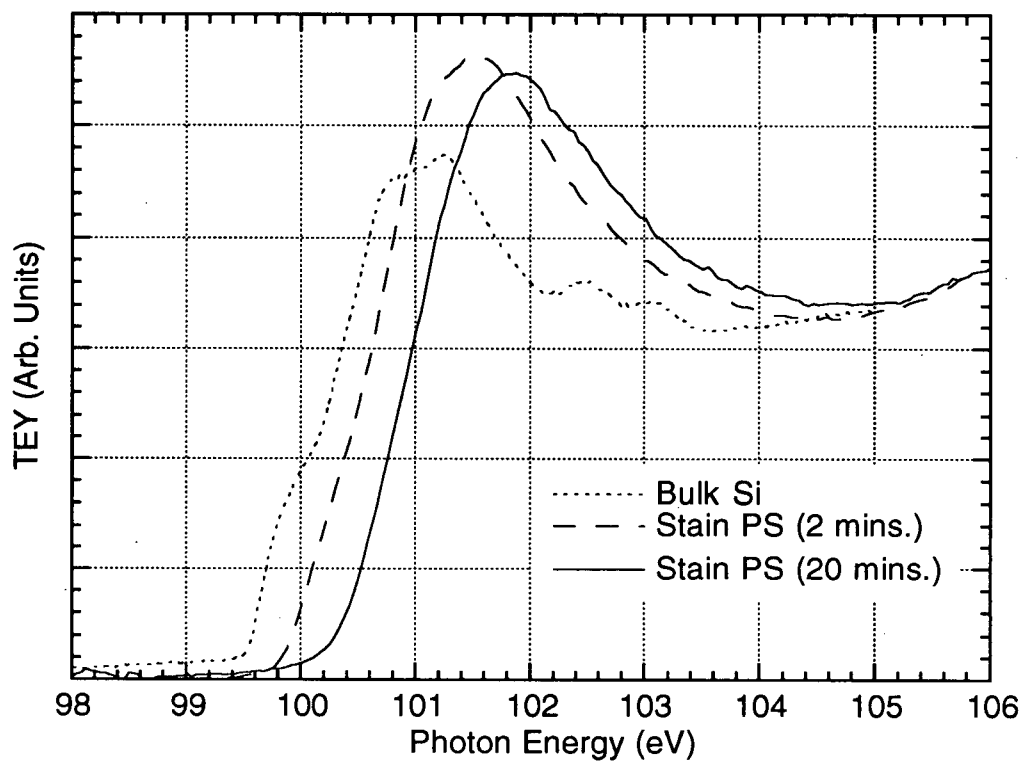


Figure 29: Total electron yield measurements at the Si $L_{2,3}$ edge for HF passivated p-type Si (100) (dotted line), and stain etch porous Si. The PS was prepared by chemically etching of p-type Si (100) in a 4:1:5 solution of HF:HNO₃:H₂O for 2 minutes (dashed line) and for 20 minutes (solid line).

5.4 PHOTOEMISSION

Photoemission is an alternative probe of the composition, that is more sensitive to surface oxygen than the total electron yield measurements. Photoemission spectra of the valence band of PS is shown in Fig. 30 together with the valence band of an HF-rinsed Si (111) wafer for reference. The photon energy is 150 eV for the silicon samples and the binding energy scale assumes a 4.5 eV work function for the electron energy analyzer. The spectrum for HF-rinsed Si is similar to earlier measurements.⁷¹ The PS valence band in Fig. 30 is shifted to higher binding energy compared with the HF-treated Si by 1.5 eV. This shift is partly due to charging. Because the PS is highly resistive, the photoemission current causes a positive charge to build up on the

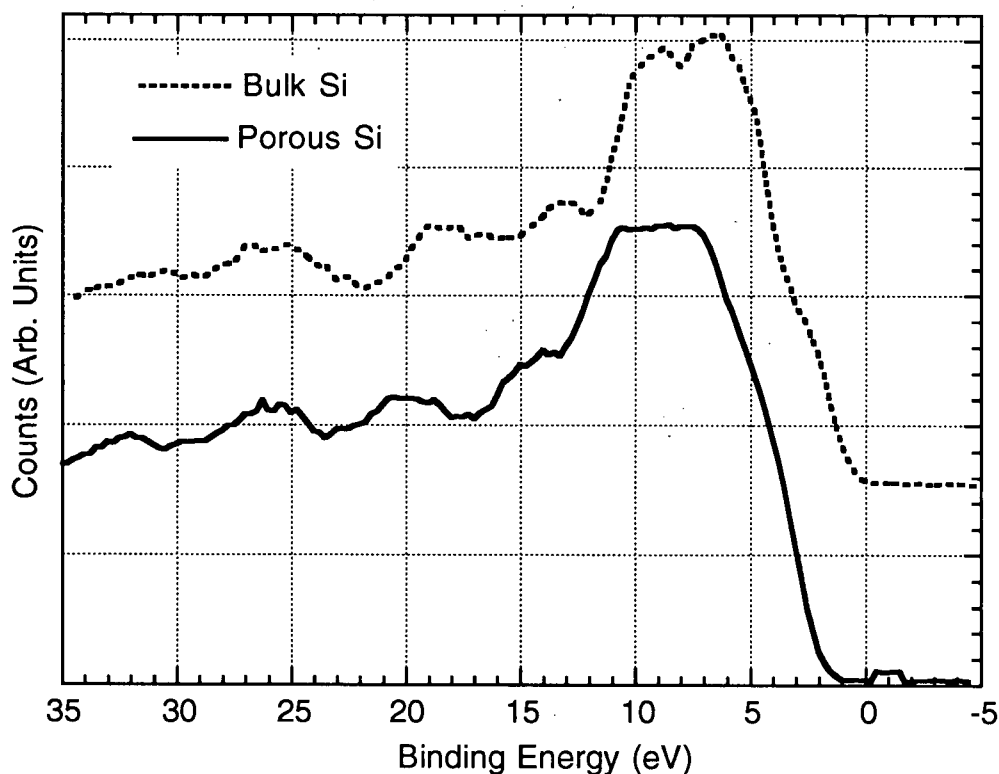


Figure 30: Photoemission valence band spectra for HF rinsed bulk Si (dotted line) and PS (solid line) measured at a photon energy of 150 eV. The spectra are raw data not corrected for charging.

sample which shifts the photoemission spectrum to higher binding energy. We chose not to use an electron flood gun to reduce the charging effect in order to ensure that there is no possibility of local negative charging of the sample caused by the flood gun. The charging effect is intensity dependent and was observed in all as-prepared PS samples to varying degrees. Differences in the Fermi level or changes in the electronic structure of the porous material due to its microstructure could also cause energy level shifts. However one can eliminate the effects of charging and changes in the surface Fermi level, at least for the top of the valence band, by referencing the valence band to the low binding energy side of the Si 2p core level. The Si 2p core level will have the same charging and Fermi-level induced shifts in photoemission as the valence band but will be insensitive to changes in electronic structure associated with the microstructure of the silicon.

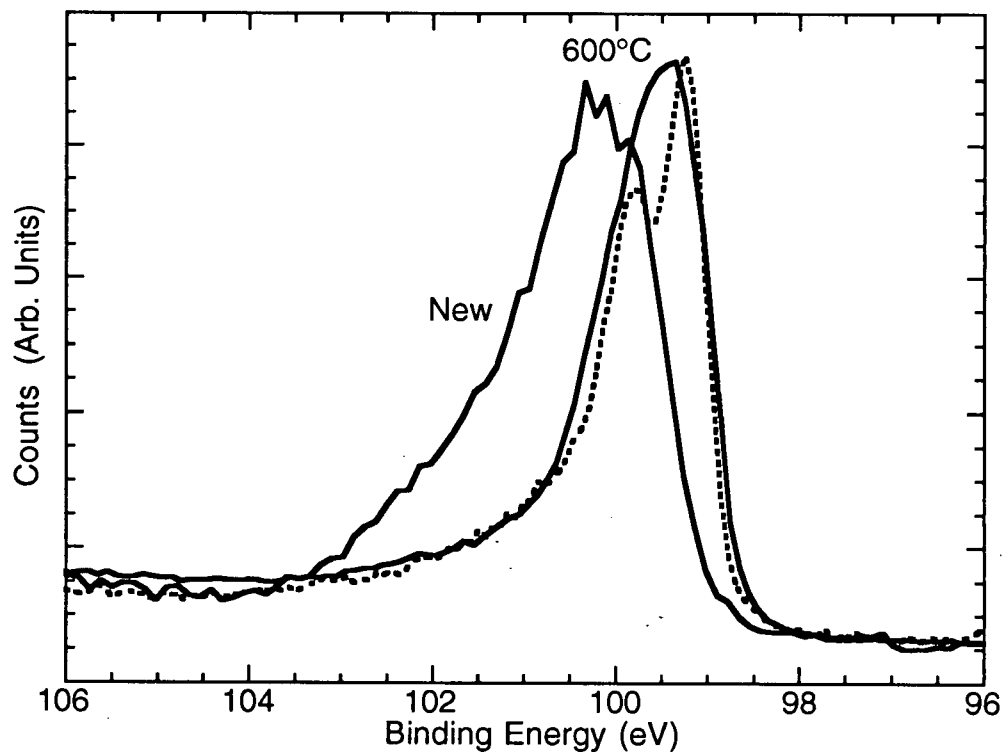


Figure 31: The Si 2p core levels measured at a photon energy of 150 eV, for the bulk Si and the PS sample shown in fig. 30. The PS data is for the as-prepared (new) sample and after annealing at 600°C.

In order to keep the charging effect the same during the photoemission measurements of the valence band and the Si 2p core level, the two spectra were measured one after the other without moving the sample or changing the photon flux. The resulting Si 2p core level spectrum is shown in Fig. 31 for the same PS sample as in Fig. 30. Compared with the spectrum for bulk Si also shown in Fig. 31, the 2p photoemission peak for PS is broadened and shifted to larger binding energy. The shape of the 2p core level spectrum varied from sample to sample and the width increased with the excitation intensity. We attribute these effects to differential charging associated with the inhomogeneous structure of the PS. Since charging shifts the spectrum to higher binding energy, the low binding energy side of the 2p photoemission spectrum will be due to that part of the material that charges the least.

In order to show in a different way that the broadening of the Si 2p core level is due to charging and not to an oxygen chemical shift we heated the PS in-situ without moving the sample, and re-measured the photoemission spectrum. After annealing the PS at 300°C for a few minutes, the 2p photoemission spectrum narrows substantially due to a reduction in the charging effect. This may be due to an increase in surface conductivity associated with a loss of hydrogen. Further heating to 600°C shown in Fig. 31 causes the Si 2p photoemission spectrum to shift and narrow to the point where it matches the binding energy and width of the bulk Si 2p level with no indication of a chemically shifted component associated with oxygen. By 600°C we expect hydrogen to be lost and the mobility of the surface atoms to be high enough for the pore structure to begin to collapse. If the as-prepared PS did contain oxygen, after annealing one would expect to see a chemically shifted component in the Si 2p level, associated with SiO₂ bonding. However a chemically shifted component is not observed in the annealed PS sample in Fig. 31 which confirms the absence of oxygen in the freshly prepared material.

Further evidence for the absence of oxygen in the PS can be obtained from the valence band photoemission. If the surface of the PS was oxidized one would expect to see peaks at 10 eV and 30 eV binding energy in the photoemission spectrum corresponding to the oxygen 2p and 2s orbitals respectively.^{71,72} Although the valence band of clean silicon has a peak near 10 eV

binding energy unrelated to oxygen, which complicates the identification of the oxygen 2p orbital, no peak is observed in Fig. 30 at 30 eV corresponding to the oxygen 2s orbital. On the other hand if the PS sample is exposed to air for a few hours strong oxygen peaks are clearly visible in the valence band photoemission. Cross section calculations show that the oxygen 2s and 2p orbitals are a factor of 4 larger photoemission cross sections at 150 eV than the Si 3s and 3p orbitals that make up the valence band.⁷³ This means that the valence band photoemission spectrum is particularly sensitive to oxygen. In addition at 150 eV photon energy the valence band photoelectrons have an escape depth of a few atomic layers. Accordingly even a fraction of a monolayer of oxygen should be easily detectable in photoemission.

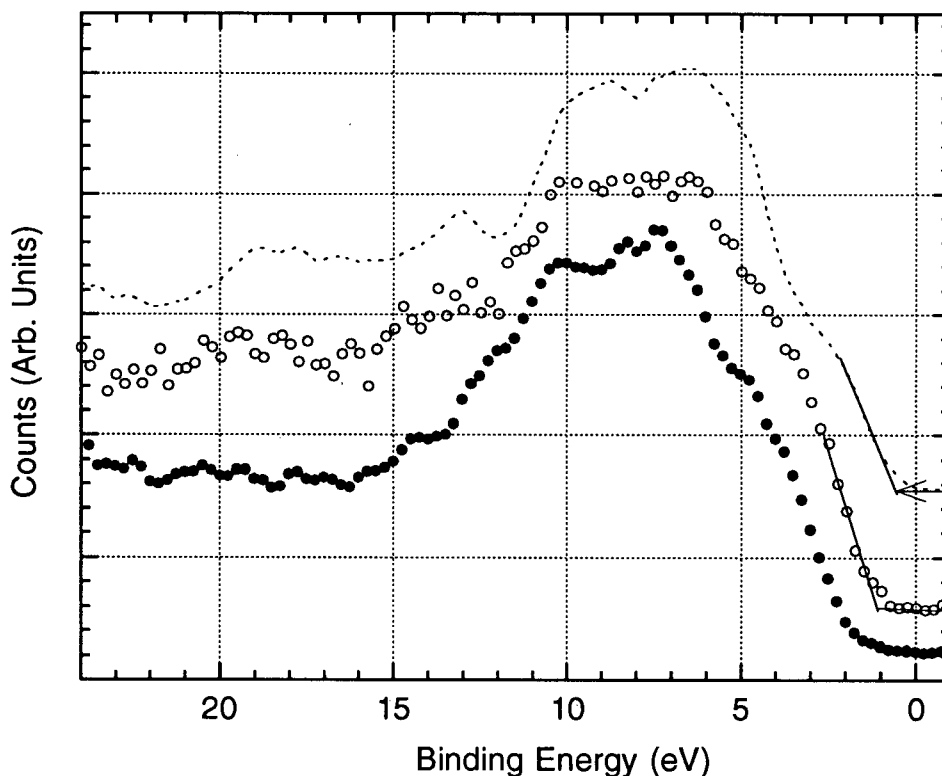


Figure 32: Photoemission spectra of the top of the valence band, corrected for charging for HF rinsed bulk Si (dotted line), for electrochemical PS (open circles) and stain etch PS (filled circles). For the electrochemical PS the current was held at 1 mA/cm² for 20 mins. followed by 40 mA/cm² for 1 min. The etch was controlled by adjusting the illumination intensity on the n-type starting material. The stain etch PS was made by etching p-type Si <100> in a 4:1:5 solution of HF:HNO₃:H₂O for 30 minutes.

In order to detect changes in the electronic structure of the top of the valence band in PS, we measured the binding energy of the top of the valence band relative to the top of the Si 2p orbital (low binding energy side). This was done by first locating the top of the valence band by a linear extrapolation of the photoemission data such as that illustrated in Fig. 32; a similar extrapolation gives the top of the Si 2p core level. Subtracting these two quantities produces a relative binding energy which is independent of charging and Fermi level shifts, that can be compared with bulk Si. If the valence band recedes due to quantum confinement, then one would expect the separation between the top of the valence band and the Si 2p level to be

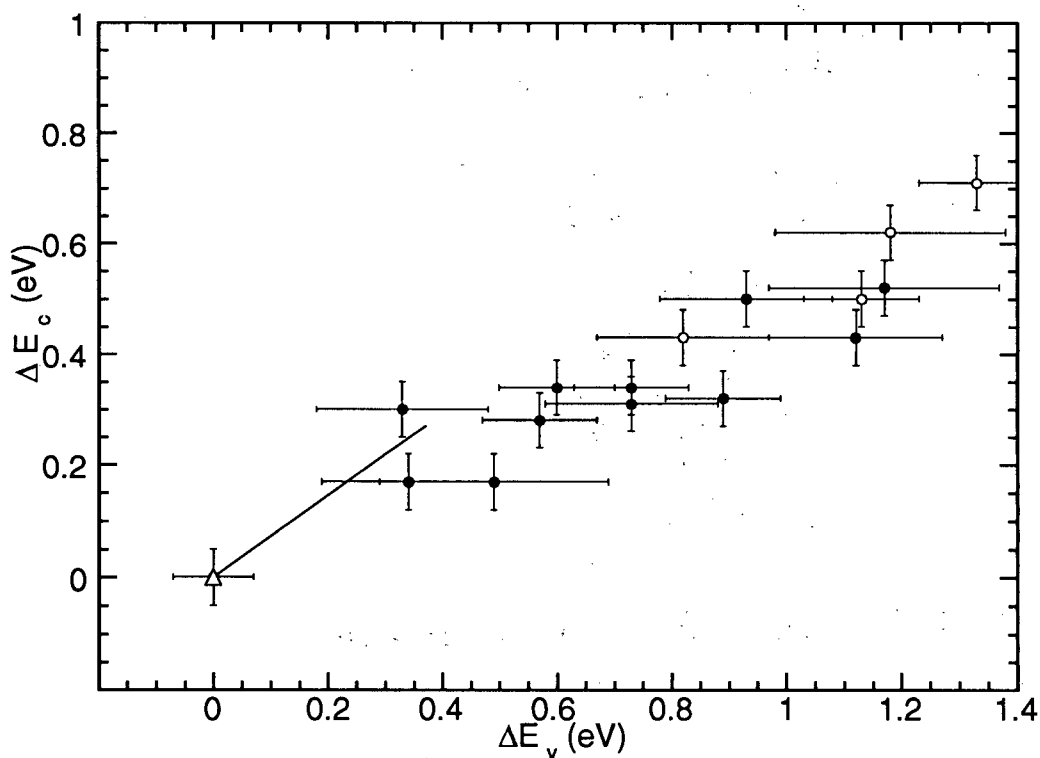


Figure 33: Conduction band shift as a function of the valence band shift for a series of porous Si samples prepared electrochemically (solid circles) and by stain etch (open circles). The shifts are measured relative to bulk Si, indicated by the open triangle. The electrochemical samples showed larger quantum shifts with increasing current density during preparation and time spent soaking in HF after preparation. The solid line is an effective mass calculation for a (100) quantum wire as discussed in the text.

reduced relative to bulk Si. A reduction in this separation is observed, as shown in Fig. 33 where we plot the conduction band edge shift as a function of the valence band shift for a series of samples. The conduction band edge shifts are determined from Si L_{2,3} edge absorption spectra such as those shown in Figs. 24 and 25.

In Fig. 33 we find the shift to higher binding energy in the valence band edge (ΔE_v) in PS is larger than the shift in the conduction band but is proportional to it, with a proportionality factor of 2.12 ± 0.17 . These results are consistent with quantum confinement in a granular material whose microstructure depends on the preparation conditions as explained further in section 7.1. It is interesting to note that amorphous silicon hydride has a bandgap in the same range as PS and that the increase in the bandgap is primarily due to the recession of the top of the valence band, as in PS.⁷⁴

The relationship between the quantum shifts in the valence and conduction band edges can be predicted from effective mass theory. This theory is valid in the limit that the quantum confinement energy is small compared to the bandgap. The quantum shifts depend on the dimensionality of the confinement and its orientation relative to the principle axes of the crystal. Since we know very little about the shape of the Si microstructures we compare the experimental data in Fig. 33 with the quantum shifts one would expect for (100) oriented quantum wires with square crosssections. In this case there exists two kinds of confinement for electrons arising from (i) the two constant energy ellipsoids with their long axis parallel with the length of the wire and (ii) the four other conduction band ellipsoids with their long axis along the (100) and (010) directions. If m_t and m_l are the transverse and longitudinal effective masses in silicon at the conduction band minimum ($0.2 m_0$ and m_0 , respectively) we obtain the following expressions for the edge shift in the conduction band:

$$\begin{aligned}\Delta E_c^i &= \frac{2\hbar^2\pi^2}{2m_tL^2} \\ \Delta E_c^{ii} &= \left(1 + \frac{m_t}{m_l}\right) \frac{\hbar^2\pi^2}{2m_tL^2}\end{aligned}\quad (23)$$

For $L=30\text{\AA}$ the two conduction band shifts are 0.420 eV and 0.252 eV respectively.

The effect of hole confinement can also be estimated with effective mass theory. In this calculation we neglect both the spin-orbit splitting and the off diagonal elements in the effective mass Hamiltonian of the valence band.⁷⁵ A perturbation calculation shows that the off diagonal part of the effective mass Hamiltonian (band warping) has a negligible effect on the lowest energy eigenstate for a (100) oriented quantum wire.⁷⁵ For a (100) wire a first series of valence band levels is given by:

$$\Delta E_v = \frac{m\pi^2(i^2 + j^2)}{L^2} \quad (24)$$

with a ground state at $i=j=1$. In the above equation m is the effective mass parameter of the valence band which is equal to -4.43 in units of $\hbar^2/2m_0$. The hole ground state quantum shift in a Si wire with a 3 nm square crosssection is equal to $\Delta E_v = 0.371$ eV. The calculated quantum shifts for the lowest quantum state are shown by the solid line in Fig. 32. In this line the lateral dimension of the wire is a parameter which has a minimum value of 3 nm at the right hand end. The corresponding theoretical lines for a (100) oriented quantum box and a (111) oriented quantum well have the same slope as the wire to within a few percent. The slope of the line calculated for a quantum wire in Fig. 33, is in good agreement with the data even though the measured quantum shifts are not small compared to the bandgap. Clearly a more elaborate electronic structure calculation is needed to make a meaningful comparison with the data over the entire range in Fig. 33.

The Si LVV Auger electron spectrum provides an alternative measurement of the quantum shift in the valence band of PS. In the quantum confinement picture the maximum kinetic energy of an Auger electron from the PS will be lower than in crystalline silicon by a factor of $2(\Delta E_v)$. The reason for the factor of two is that the ejected Auger electron comes from a valence band with

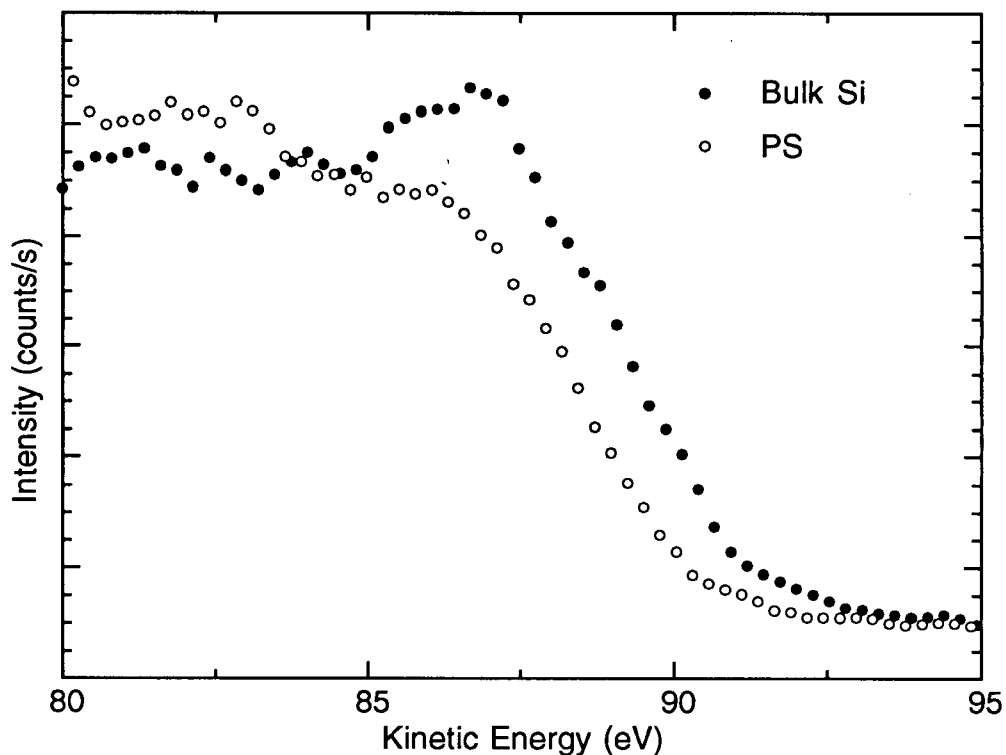


Figure 34: LVV Auger spectra measured at $h\nu = 140$ eV, for bulk Si (solid line), as prepared PS (open circles). The PS was prepared by electrochemically etching (111) oriented n-type Si at $1\text{mA}/\text{cm}^2$ for 15 min. followed by $25\text{mA}/\text{cm}^2$ for 5 min. The current was controlled by changing the illumination intensity.

a larger minimum binding energy while at the same time the electron that drops into the 2p core level has less excess energy to dissipate since it comes from the quantum shifted porous silicon valence band. In Fig. 34 we show the LVV Auger electron edge of an electrochemical PS sample along with the Auger edge of bulk Si. In Fig. 35 we show the valence band photoemission data for the same samples. Notice that the Auger edge for the PS is shifted to lower kinetic energy by 1.2 eV when compared to bulk silicon which is exactly twice the valence band shift, ΔE_v , obtained from the photoemission data in Fig. 35. Fig. 36 shows the correlation between the quantum shifts of the Auger and valence band edges for a range of PS samples. The data agrees well with the solid line which represents a proportionality factor of 2 between the Auger and valence band shift.

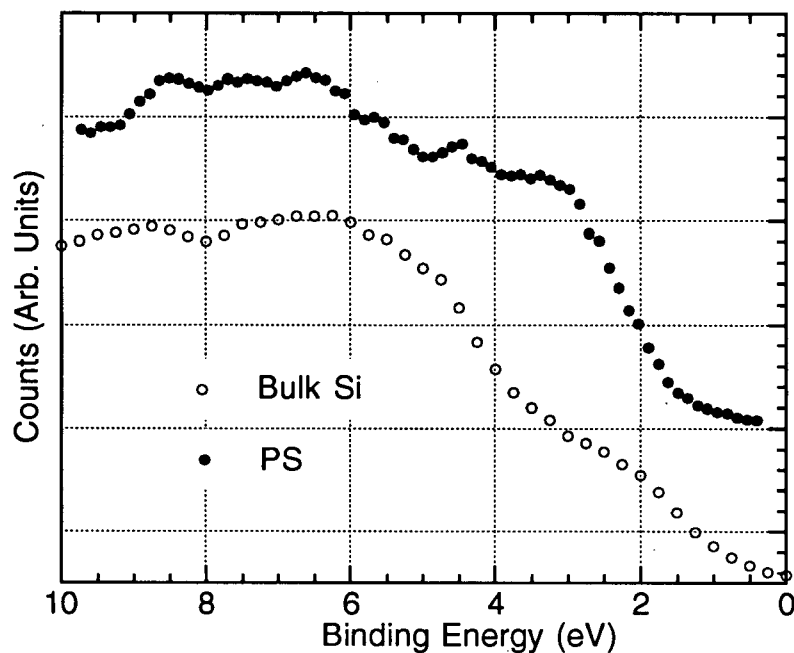


Figure 35: Photoemission spectra of the valence band of PS at $h\nu=140$ eV for an as-prepared sample (solid circles) and bulk silicon (open circles). The valence band spectra have been referenced to the Si 2p core level to correct for charging or Fermi level shifts.

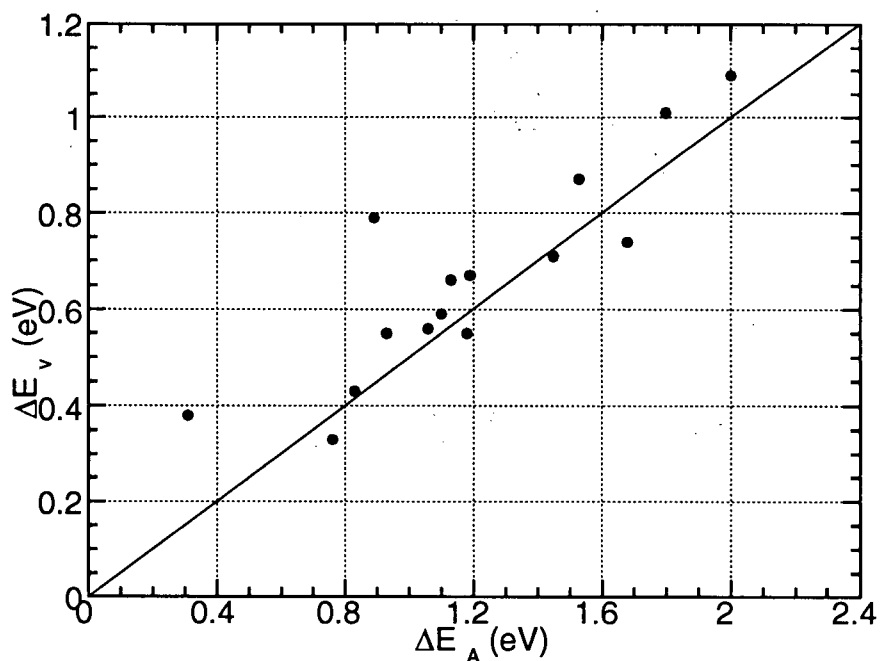


Figure 36: Correlation between the quantum shifts of the Auger and valence band edges for a range of PS samples. The solid line represents a proportionality factor of 2 between the Auger and valence band shift.

6. SILOXENE

An alternative explanation for the optical properties in PS is that the etching reaction leaves a siloxene-like residue on the surface of the porous silicon and that this material is responsible for the luminescence. "As-prepared" siloxene luminesces efficiently in the visible (550nm)^{12,76,77}, while siloxene heated to 400°C in inert gas is much weaker⁷⁰ and is near 700-800 nm.^{76,77} The PL peak of PS can be shifted depending on preparation conditions in approximately the same range as the siloxene and the heat treated siloxene samples. Structural modifications of siloxene have been proposed that according to theory exhibit "chemical quantum confinement" with various optical bandgaps.¹³ These proposed chemical confinement structures are shown in Fig. 12. However, the x-ray diffraction pattern for siloxene is consistent with only one structure, in which (111) sheets of silicon are terminated on one side by hydrogen and on the other side by OH.^{41,42} It was also shown that as-prepared siloxene has a substantial amorphous SiO_x impurity with 1 < x < 2.

The silicon L-edge absorption of PS, siloxene and HF rinsed crystalline Si are compared in Fig. 37. Only the siloxene absorption spectrum shows clear evidence of oxygen. In the siloxene case the large peaks near 106 and 108 eV in Fig. 37 are excitonic features characteristic of SiO₂.⁷⁸ We attribute this part of the spectrum to the amorphous SiO_x impurity phase which was observed in the x-ray diffraction experiments. There is no indication of the peak at 104.5 eV reported for SiO. The silicon L-edges in PS and HF-rinsed crystalline silicon, in Fig. 37, show neither the SiO nor the SiO₂ peaks. However, it is possible that the terminal OH groups on the siloxene sheets also do not produce any sharp features in the silicon L-edge. For example excitonic effects in the absorption associated with SiO₂ may not be present with a single SiO bond on a given Si atom. Therefore the absence of the peaks associated with SiO (bridging oxygen) and SiO₂, in the PS absorption spectrum, does not in itself prove that there is no siloxene present on the surface of the porous silicon. In addition the siloxene, like the PS, shows a blue shift in the L-edge relative to crystalline silicon of approximately 0.65 eV.

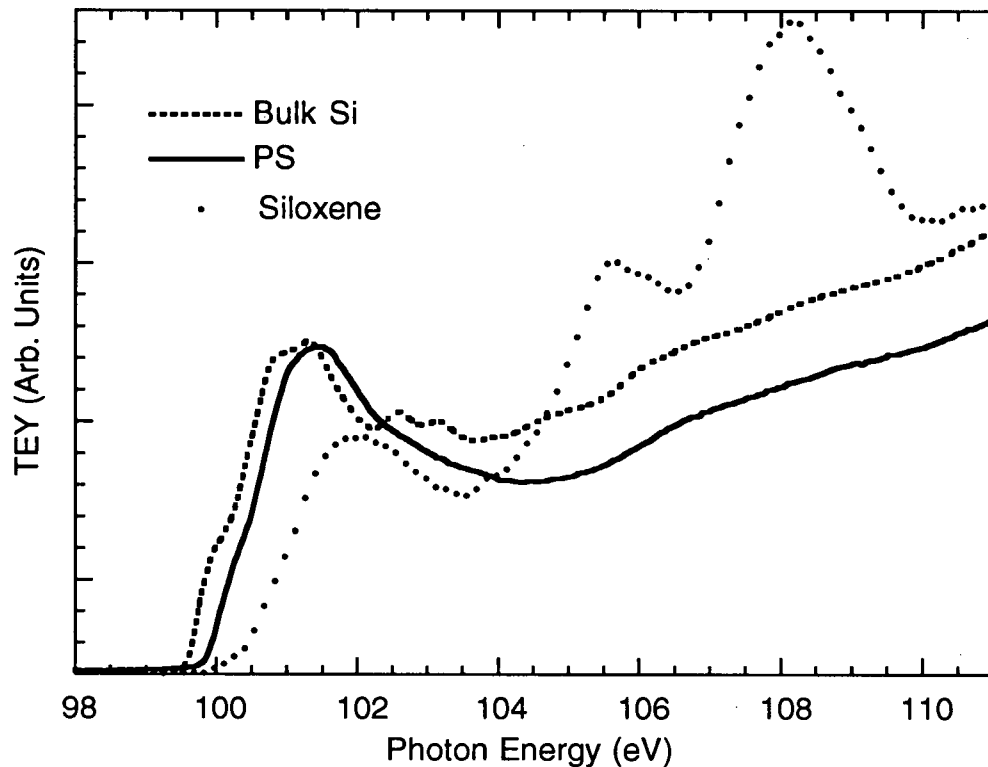


Figure 37: Total electron yield measurements of x-ray absorption at the silicon $L_{2,3}$ edge for HF passivated n-type Si (111) (dotted line), siloxene (dots), and porous Si (solid line). Porous Si was prepared by an electrochemical etch of n-type Si (111) in 30% HF in ethanol. The current density was kept constant at 0.4 mA/cm^2 for 40 min. then raised to 40 mA/cm^2 for 2 min.

The silicon K-edge spectra for siloxene, stain etch PS and crystalline Si are shown in Fig. 38. The chemical PS samples were prepared by etching p-type Si $\langle 100 \rangle$ in a 4:1:5 solution of HF:HNO₃:H₂O for 20 minutes. The absorption edges of the stain etch PS and siloxene are compared to that of bulk Si and are found to be blue shifted.⁴¹ The absorption edge of the stain etch PS is 0.6 eV higher than bulk Si and is similar to the K-edge shown in Fig. 22 for the electrochemical PS sample. A large absorption peak is observed in the siloxene sample at 1847 eV which is due to the amorphous SiO_x impurity phase.^{41,79} The magnitude of the SiO_x peak varies from sample to sample depending on the preparation conditions and the age of the siloxene. The

K-edge absorption of siloxene ranged from 0.5 to 0.6 eV higher than bulk Si. Also the absorption edge of the siloxene is sharper than that of the bulk Si. It is interesting to note that the measured L-edge shift for the siloxene and stain etch PS samples shown below is approximately 0.1 eV larger than the K-edge shift measured on the same samples. Not enough data has been taken to determine if this is experimental error or a real effect.

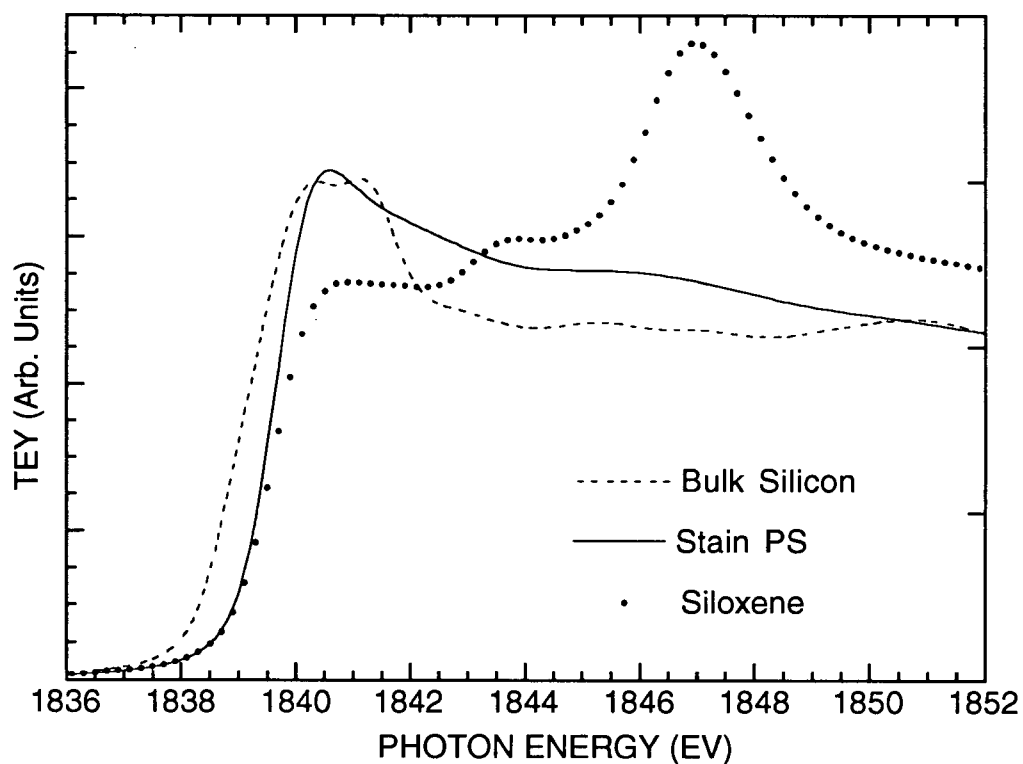


Figure 38: Si K-edge absorption spectra for bulk Si (dotted line), stain etch PS (solid line) and as prepared siloxene (dots).

Further evidence for the absence of oxygen in the PS can be obtained from the valence band photoemission, an alternative probe of the composition, that is more sensitive to surface oxygen than the total electron yield measurements. Photoemission spectra of the valence band of PS and siloxene are shown in Fig. 39 together with the valence band of an HF-rinsed Si (111)

wafer for reference. The valence band spectrum for siloxene shown in Fig. 39 has strong peaks near 10 eV and 30 eV characteristic of oxygen 2p and 2s orbitals respectively. However the PS valence band spectrum does not show the peaks at the position of the oxygen 2s or 2p orbitals. Thus the absence of oxygen in photoemission in the as-prepared PS, as shown in Fig. 39, also means that there is no siloxene on the surface.

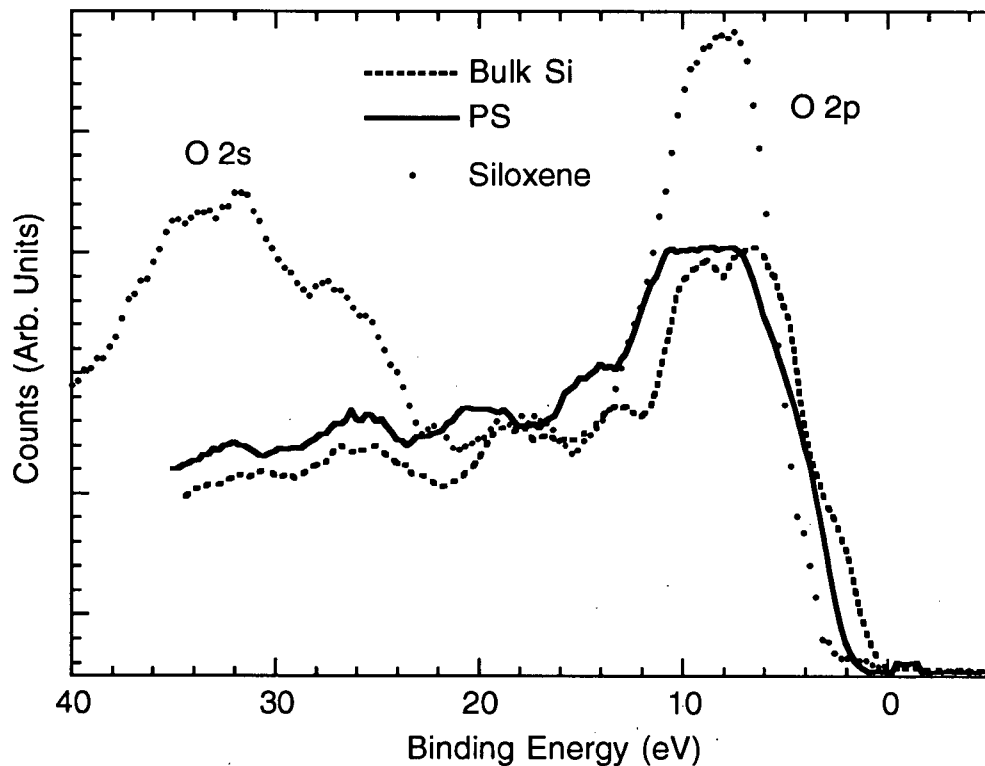


Figure 39: Photoemission valence band spectra for HF rinsed bulk Si (dotted line) and PS (solid line) measured at a photon energy of 150 eV. The dots is the valence band of siloxene measured at a photon energy of 100 eV. The spectra are raw data not corrected for charging.

The x-ray absorption of the layered polysilane and PS are found to be remarkably similar as shown in Fig. 40. In particular, the K absorption edge of layered polysilane is shifted by 0.62 eV with respect to bulk silicon.^{41,80} This is the same as that of the stain etch PS sample. Conceivably, PS, which we know to be oxygen free, could be made up of a small number of Si.

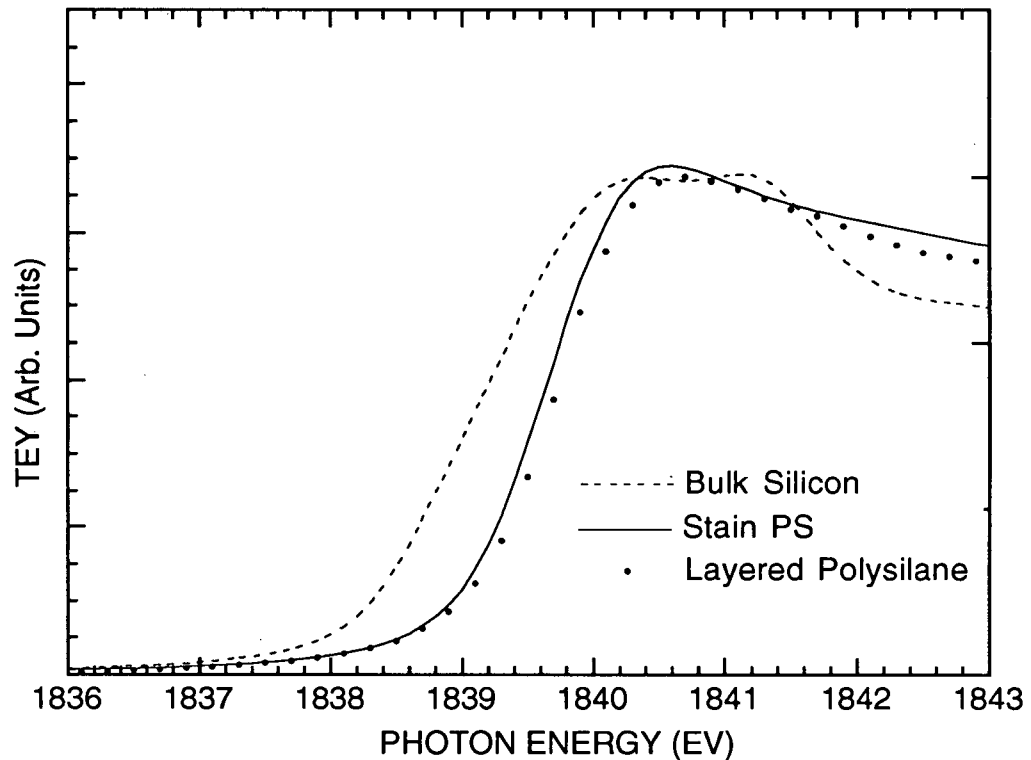


Figure 40: The silicon K-edge spectra for layered polysilane, stain etch PS and crystalline Si.

(111) layers stacked as in crystalline Si but terminated above and below with hydrogen. The as-prepared siloxene spectrum also resembles that of layered polysilane apart from the peak due to α - SiO_2

Figure 41 shows the L-edge absorption spectra for crystalline silicon, amorphous- SiO_2 and a heat treated siloxene sample. The heat treated siloxene sample shows features in the absorption spectrum which can be associated with both Si and SiO_2 . The edge jump at 99.5 eV in the heat-treated siloxene is not shifted with respect to bulk silicon. It shows the spin-orbit splitting, but does not show a peak after the edge like that of crystalline silicon. These are exactly the characteristics of the L-edge of amorphous Si. The x-ray diffraction pattern of heat treated siloxene closely resembles that of amorphous-Si not siloxene.⁴¹ Contrary to the diffraction data the valence

band photoemission spectra for heat treated siloxene is basically identical to the spectra for amorphous-SiO₂.

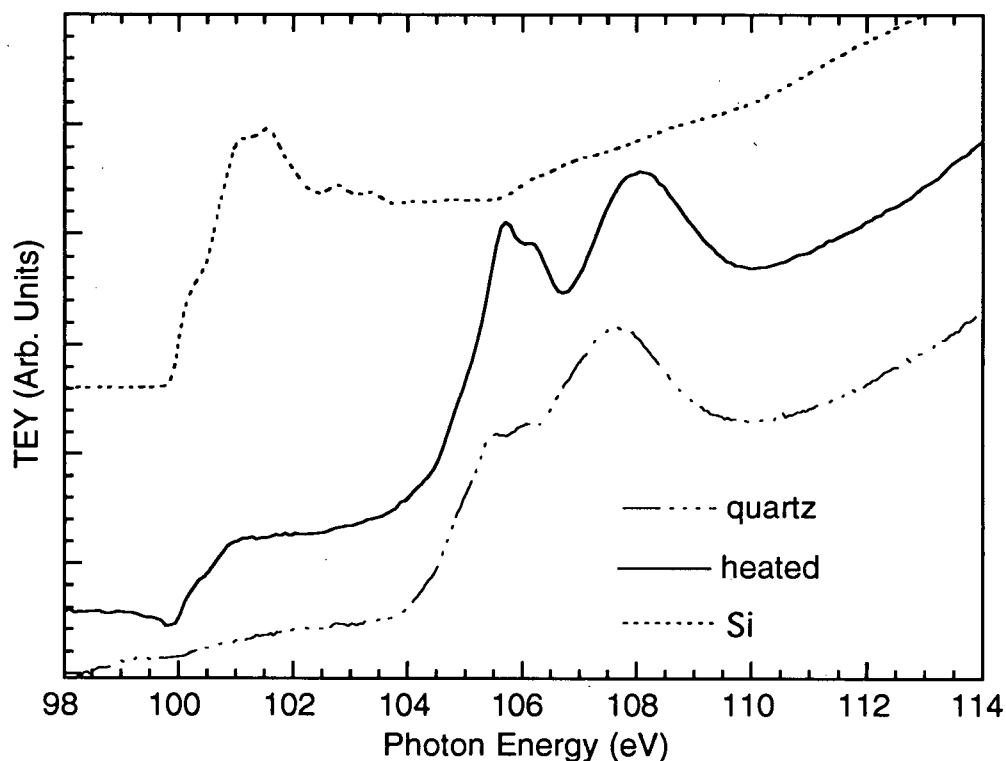


Figure 41: L-edge absorption spectra for crystalline silicon, heat treated siloxene, and amorphous-SiO₂. The curves have been offset vertically for clarity.

The results show that in bulk measurements (diffraction) heat treated siloxene resembles amorphous-Si; in surface sensitive measurements (photoemission) it resembles amorphous-SiO₂, and with an intermediate probe of depth (TEY) it shows the characteristics of both. This indicates that heat treated siloxene must be considered to be small amorphous-Si particles coated with amorphous-SiO₂. As siloxene (Si₆H₆O₃) is heated to 250°C, the layer structure collapses and hydrogen gas is evolved.⁸¹ The results suggest that once the hydrogen is released the silicon and oxygen arrange into clusters of Si coated by SiO₂. If the Si particles are small enough, they will show quantum size effects. Presumably this could explain the weak visible luminescence in the heat treated siloxene. Heat treated siloxene may be similar to rapid thermal oxidized PS. ⁸²

7. EFFECT OF PREPARATION CONDITIONS ON BANDGAP

7.1 ANNEALING EFFECTS

Thermal annealing studies have shown that the visible PL shifts to the red, and eventually disappears when PS is heated to 600°C in vacuum^{83,84}. In the context of the quantum confinement model the disappearance of the PL during thermal annealing can be attributed to non-radiative recombination caused by dangling bonds that are generated as the passivating hydrogen is lost from the surface. On the other hand, in the molecular surface species model the changes in the PL with annealing would be due to the decomposition of the surface species.

The PS samples were thermally annealed in UHV through resistive heating of the sample holder. The temperature of the sample was measured with an optical pyrometer which was calibrated on one PS sample with a thermocouple pressed onto the back. The absolute sample temperature is believed to be accurate to $\pm 30^\circ\text{C}$. The PS was annealed at each temperature for a fixed time of 3 minutes and then returned to room temperature for x-ray absorption and photoemission measurements. Hydrogen evolution during annealing was detected with a mass spectrometer mounted with a line of sight to the sample. During each anneal the maximum amplitude of the mass two peak (H_2) was recorded. After each anneal the PS sample was inspected visually in-situ for PL, which was excited by the 337 nm line from a HeCd laser. Progressively higher temperature anneals caused a red shift in the L-edge absorption and the gradual reappearance of the spin orbit splitting as shown in Fig. 42. In this figure the PS L-edge is plotted after anneals at 300°C, 455°C and 590°C. We note that after annealing at 590°C the PS absorption edge is red shifted slightly (0.1 eV) below the bulk Si L-edge. Also the shape of the absorption edge is qualitatively different in that the ratio of L_2 to the L_3 absorption edges appears to be larger for PS annealed at 590°C than for bulk Si.

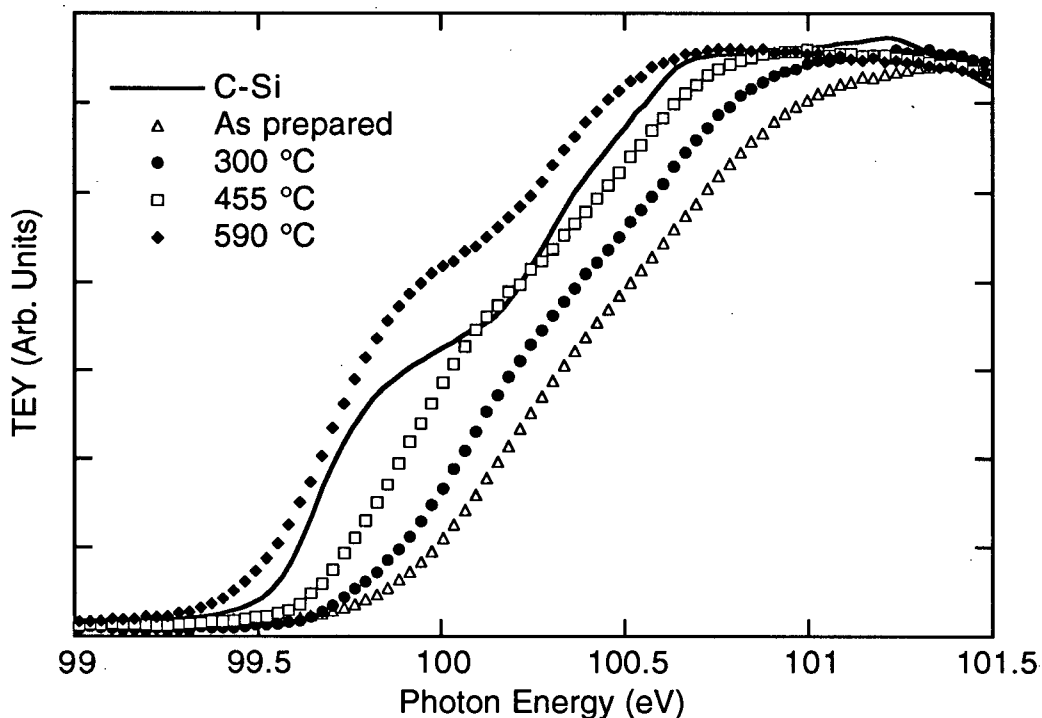


Figure 42: Total electron yield measurements of absorption at the Si L_{2,3} edge for a crystalline Si sample (solid line), a freshly etched PS sample (open triangles), and PS heated to 300°C (solid circles), 455°C (open squares) and 590°C (solid squares). The electron yields have been scaled by the edge jump to facilitate comparisons. The PS was electrochemically etched at 1mA/cm² for 15 min. followed by 35mA/cm² for 5 min. by increasing the illumination intensity on the (100) n-type starting material.

In Fig. 43 we plot the quantum shift in the L-edge and the peak H₂ signal from the mass spectrometer as a function of annealing temperature. Hydrogen will desorb from PS when the temperature is high enough to sever the Si-H chemical bond. Fourier transform infrared studies on PS annealed in vacuum have shown that hydrogen from SiH₂ species desorbs between 360 and 420°C, whereas hydrogen from SiH species desorbs between 450 and 530°C^{84,85}. The as-prepared PS sample shown in Fig. 43 initially had a 0.4 eV quantum shift in the L-edge, which with stepwise annealing up to 430°C decreased by 0.1 eV. Hydrogen evolution was observed in

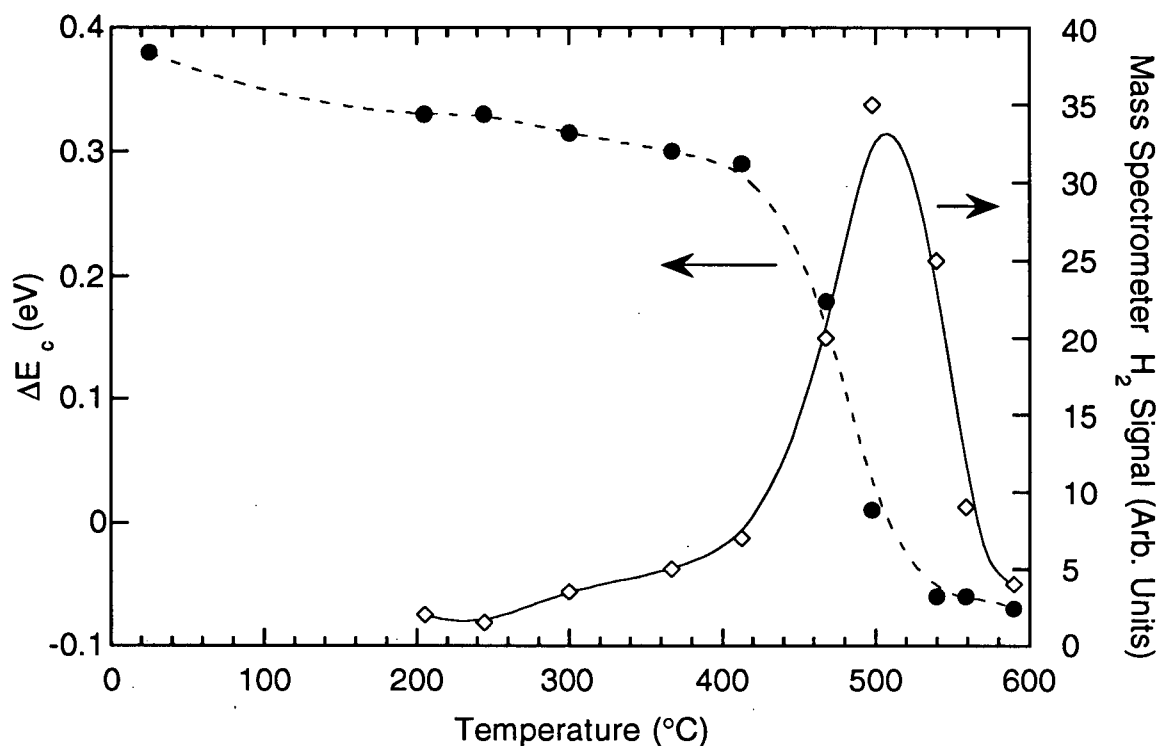


Figure 43: Energy shift of the conduction band edge relative to bulk Si measured by x-ray absorption and the peak H_2 signal observed in the mass spectrometer during annealing, as a function of the annealing temperature.

the mass spectrometer over the same annealing temperature range, presumably due to dissociation of SiH_2 species. On annealing above $430^\circ C$ ΔE_c drops sharply to zero and then at $540^\circ C$ becomes slightly red shifted while in the same temperature range the hydrogen evolution peaks and then drops to zero. ΔE_c remained constant at -0.07 eV when the PS sample was annealed above $530^\circ C$.

The intensity of the visible PL from the PS was not affected by anneals below $300^\circ C$. Between 300 and $420^\circ C$ the PL intensity decreased with annealing temperature and above $420^\circ C$ no PL was detectable visually, consistent with previous PL studies on PS^{83,84}. The PS PL disappears at a lower annealing temperature than the sharp drop in ΔE_c presumably because of the strong effect of a few Si dangling bonds on the non-radiative recombination rate. The L-edge shifts and hydrogen evolution results can be explained in a straight forward way with the quantum confinement model. We propose that as the hydrogen passivation layer desorbs, the PS

nanostructures agglomerate to reduce their surface energy. The resulting net increase in the size of the microstructure reduces the quantum confinement effect.⁸⁶ The slight red shift in the L-edge in the agglomerated PS could be due to structural disorder which could reduce the gap.

Photoemission studies show that the valence band edge is also shifted in PS relative to bulk Si. Earlier we showed that the shift to higher binding energy in the valence band edge (ΔE_v) in PS is larger than the shift in the conduction band but is proportional to it.¹⁶ In Fig.44 we show the valence band photoemission spectrum of as-prepared PS and the same sample after heating to

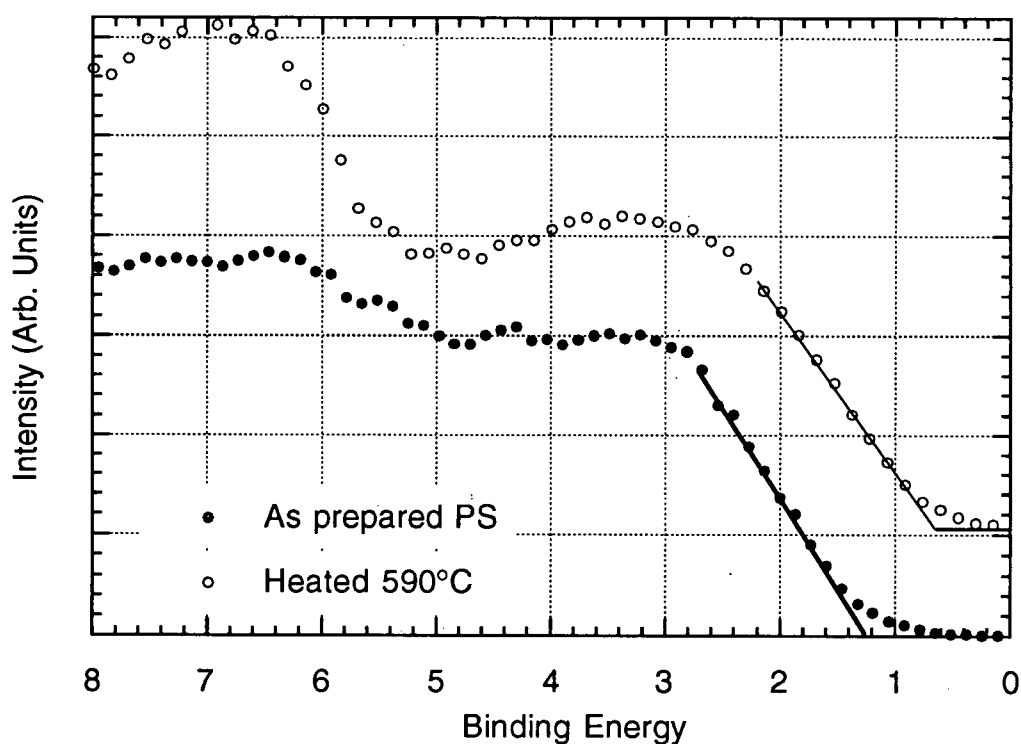


Figure 44: Photoemission spectra of the valence band of PS at $h\nu=140$ eV for an as-prepared sample (solid circles) and the same sample after annealing at 590°C . The valence band spectra have been referenced to the Si 2p core level to correct for charging or Fermi level shifts. The PS was prepared by electrochemically etching (111) oriented n-type Si at $1\text{mA}/\text{cm}^2$ for 15 min. followed by $25\text{mA}/\text{cm}^2$ for 5 min. The current was controlled by changing the illumination intensity.

590°C, both measured at a photon energy of 140 eV. The valence band edge of the as-prepared PS has a higher binding energy (by 0.6 eV) than the same sample after heating to 590°C. In the latter case the binding energy is the same as for bulk Si. The peak in the photoemission spectrum at 7 eV binding energy for the annealed PS in Fig.44 corresponds to the oxygen 2p orbital. The intensity of this peak increases with each consecutive anneal. During annealing the chamber pressure can rise as high as 1×10^{-7} Torr for a short period of time due to out-gassing of water vapor from the sample, sample holder and exposed parts of the chamber. This water vapor may be responsible for the oxygen contamination of the PS after annealing. The valence band photoemission is sensitive to even a fraction of a monolayer of surface oxygen because the oxygen 2p orbital has a significantly larger cross section at 140 eV photon energy than the Si 3s and 3p orbitals which make up the valence band.⁷³

We have plotted ΔE_v (open circles) and $(\Delta E_A)/2$ (filled circles) on the same energy scale for easy comparison in Fig. 45. Note that the conduction and valence band edge shifts have the same dependence on annealing temperature. As expected the data points for ΔE_v and $(\Delta E_A)/2$ are consistent at all annealing temperatures within experimental error. Also for ease of comparison the conduction band edge shift, ΔE_c , is plotted on a scale that is expanded by a factor of 2.0 on the right hand axis. This is further illustrated in Fig.46 where we plot the ΔE_c as a function of ΔE_v with annealing temperature as a parameter for a number of different PS samples. Note that the conduction and valence band edge shifts have the same dependence on annealing temperature. A linear fit to the data gives a proportionality factor of 1.89 ± 0.18 for $\Delta E_v/\Delta E_c$. This is in good agreement with the value reported earlier of 2.12 ± 0.17 on a series of samples made with different preparation conditions.^{16,86-88}

The fact that the ratio of the valence band shift to the conduction band shift remains constant during annealing suggests that the quantum shift in the two band edges is not sensitive to the geometric shape or crystallographic orientation of the microstructure of the PS. The alternative explanation seems unlikely, namely that the surface orientation and shape remains fixed as the

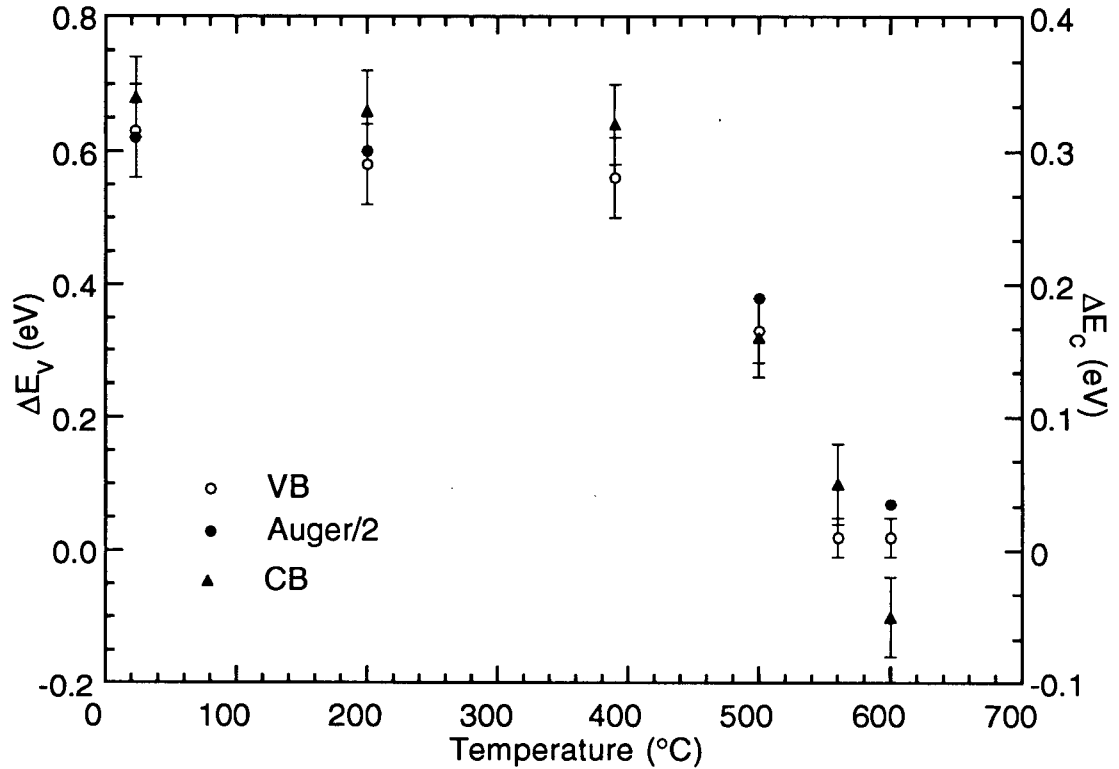


Figure 45: Quantum shift in the conduction band measured by x-ray absorption (triangles), and in the valence band measured by photoemission (open circles) and by Auger spectroscopy (solid circles) all for the same PS sample as a function of annealing temperature. The shift in the Auger spectrum has been divided by two to facilitate comparisons with the photoemission data. Valence and conduction band quantum shifts include error bars representing uncertainty in measurement.

microstructure grows in size during annealing. Quantum confinement shifts can be estimated most simply in the effective mass approximation where we neglect the spin-orbit splitting as discussed earlier. In this model the ratio of the valence to conduction band edge shifts is 1.48 for a $\langle 100 \rangle$ oriented wire with a square cross section and 1.42 for a $\langle 100 \rangle$ oriented square box. Similarly the ratios are 1.42, 1.48 and 4.4 for one dimensional quantum wells oriented in the (111), (110) and (100) directions respectively^{16,75}. Except for the effective mass result for the (100) well, these values are close to the measured ratio and support the hypothesis that the ratio may not be very sensitive to the geometric shape or crystallographic orientation of the microstructure in the PS.

More sophisticated pseudopotential calculations give a ratio of valence to conduction band edge shifts of about 1.8 for (100) quantum wells⁸⁹, and for 2.0 spherical quantum dots⁹⁰ rather different from the effective mass calculation but in good agreement with the experimental data.

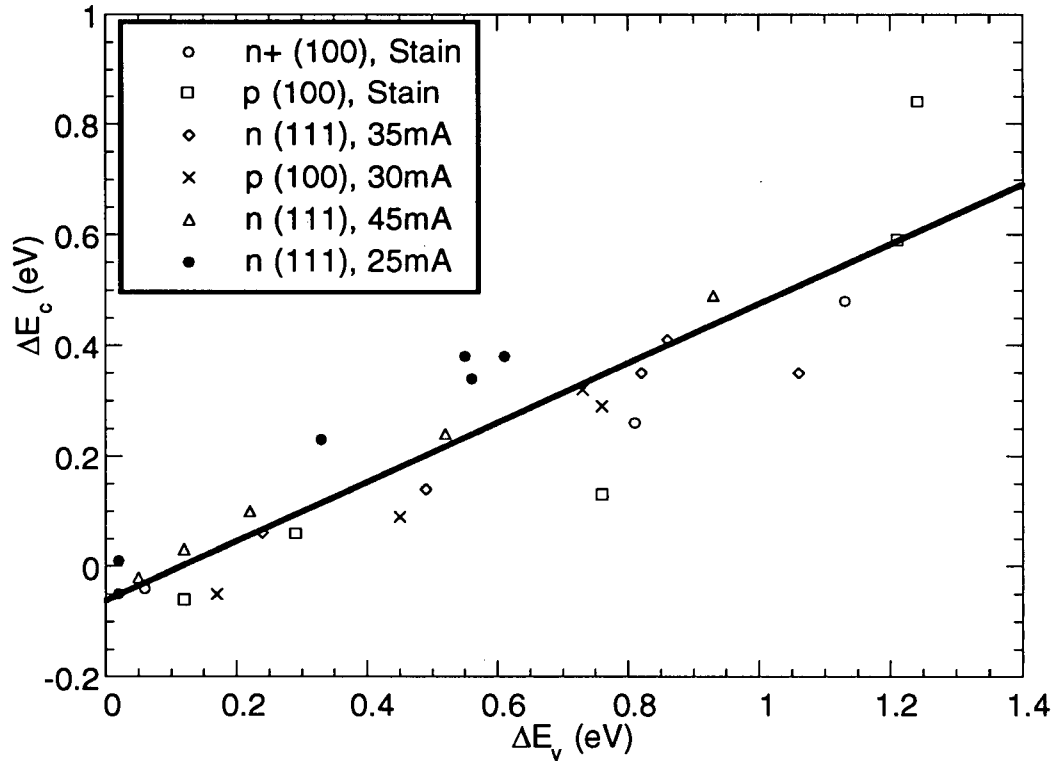


Figure 46: Conduction band shift as a function of the valence band shift with annealing temperature as a parameter for a number of different porous Si samples. The type of silicon and reaction used to form the PS is given in the legend. Electrochemical PS is labeled by the current density used in the anodization, chemical PS etched in a 4:1:5 HF:HNO₃:H₂O solution is labeled as stain. The solid line is a best fit line to the data.

In principle the L-edge blue shift in PS might also be explained by a chemical shift in the Si 2p core level caused by hydrogen bonding. In fact an apparent chemical shift is observed in the more surface sensitive Si 2p core level photoemission, although this could also be caused by inhomogeneous charging of the PS or small amounts of surface oxide. Since blue shifts of up to

0.7 eV are measured in some of the PS samples and the Si 2p core level is chemically shifted by 0.3 eV per hydrogen bond⁹¹, at least two hydrogen bonds per silicon atom would be needed to explain the L-edge data. This amount of hydrogen would require a polysilane (linear chain) structure which has a Si/H ratio of 1/2. This structure would be expected to have a dramatically different L-edge absorption from bulk Si, in addition to a hydrogen chemical shift. Even for the smaller blue shifts the chemical shift explanation would still require of order one bonded hydrogen for each Si atom, to a depth of order 10's of nanometers in the PS: a surface hydrogen layer would not be enough. Such high hydrogen contents are difficult to reconcile with the experimental observation that the hydrogen passivation of PS can be replaced by oxygen while retaining similar photoluminescence characteristics.^{82,83,92} Furthermore, hydrogen will chemically shift the 2p core level and add a Si-H bonding orbital to the valence band, but otherwise have little effect on the valence band edge. Since the valence band edge is measured relative to the 2p core level the net effect on the valence band will be to cause an apparent shift to lower binding energy, contrary to what is observed.

7.2 SELF LIMITING MODEL

7.2.1 Model 1: Porous Silicon Strongly Coupled to Bulk Silicon

For reasons that are discussed further below the anodization process preferentially etches the bulk silicon at the bottom of the pores and does not attack the PS film that is left behind on the surface as a product of the reaction. One can conclude that the etching process is self-limiting and stops when the thickness of the residual silicon reaches a certain critical value. The chemical reaction that takes place in the etching process requires holes to be available at the semiconductor electrolyte interface. It has been proposed that the self-limiting behaviour of the etching process is

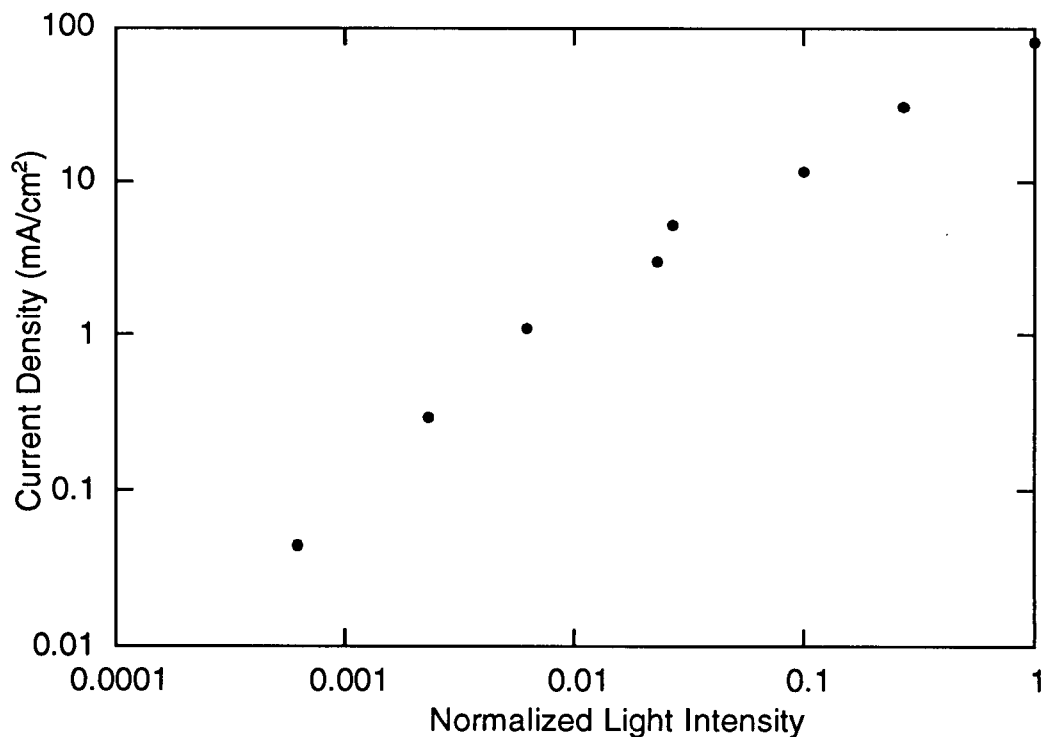


Figure 47: Current density as a function of light intensity during electrochemical etching of n-type 1-30 Ω -cm silicon at 5 V applied bias. A background current density of 0.2 mA/cm² measured in the dark, has been subtracted.

caused by a reduction in the number of holes at the semiconductor-electrolyte interface when the dimensions of the silicon microstructures in the porous material are small enough to produce a quantum shift in the valence band.³ To test the hypothesis that the self-limiting behaviour of the etching process is due to the quantum confinement effect and to identify the preparation conditions which produce large quantum shifts, we have explored the effect of various preparation conditions on the silicon L-edge shift in PS.

The porous silicon samples are made from n-type Si anodized under illumination from a halogen lamp. A constant voltage of 3V was applied between the silicon substrate and the Pt wire

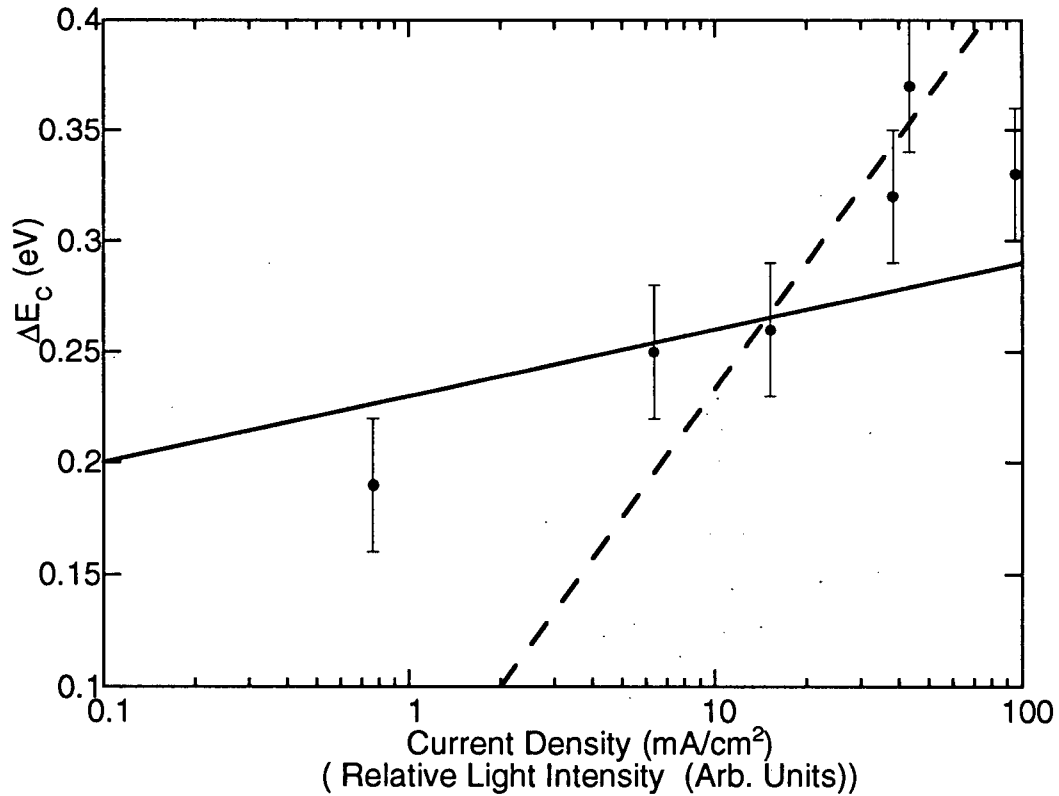


Figure 48: Conduction band edge shift as a function of the current density used to make the PS. The current density is proportional to the light intensity. The number of photo-generated holes is also proportional to the light intensity. The solid line has a slope of $0.5 kT$ as predicted by the model 1 and the dashed line has a slope of $0.33 kT_L$ as predicted by model 2. Both models are discussed in the text.

counter electrode during preparation. For the 3 V bias used in the anodizing, the current in the electrochemical cell is approximately linear in the light intensity, as shown in Fig. 47.^{69,93} A series of samples were prepared at different current densities by first pre-anodizing n-type Si substrates for 10 mins. at a current density of 0.8 mA/cm^2 , and then increasing the current density to a new value for the final 5 mins. by adjusting the illumination intensity. A graph of the quantum shift as a function of the current density in the last 5 min of the anodization is shown in Fig. 48. A second set of PS samples were prepared from n-type Si. In this case the current density was kept constant and the etching time was varied. The quantum shift as a function of etching time is plotted in Fig. 49 for a series of samples etched at a constant current of either 25 mA/cm^2 or 10 mA/cm^2 .

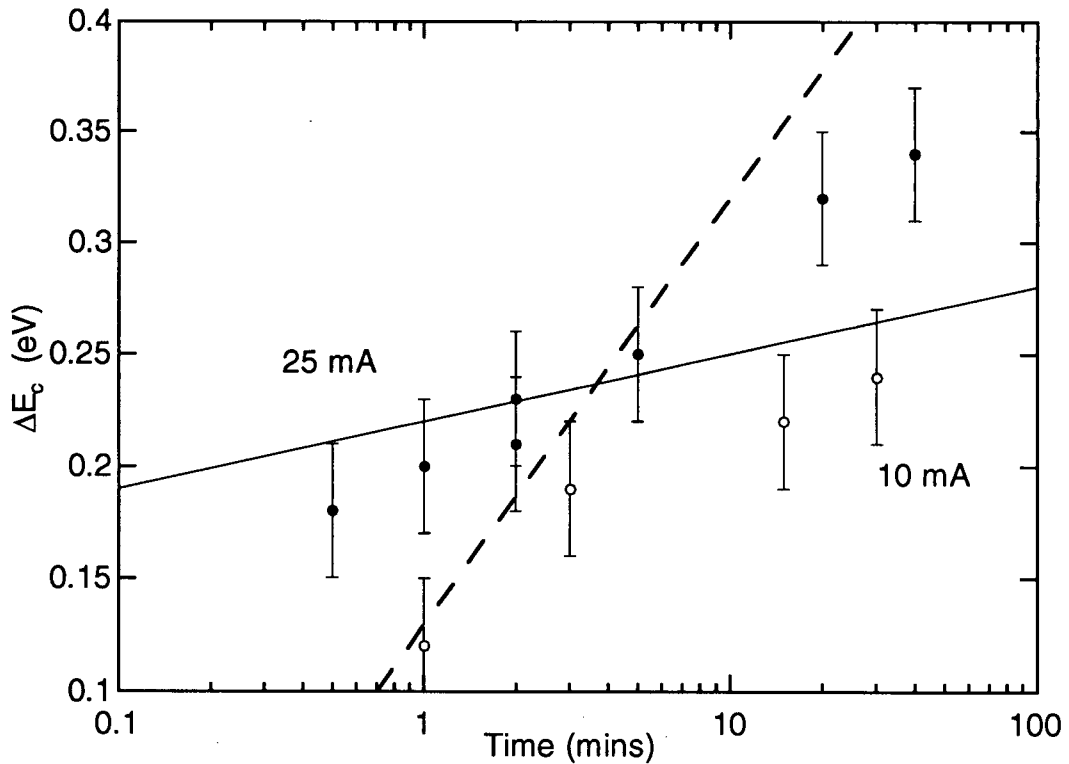


Figure 49: Conduction band edge shift as a function of the anodization time used to make the PS. The filled circles represent samples etched at a current density of 25 mA/cm^2 . The open circles are

samples etched at 10 mA/cm². The solid line has a slope of 0.5 kT as predicted by the model 1 and the dashed line has a slope of 0.33 kT_L as predicted by model 2.

The blue shift in the CB edge increases in a logarithmic manner with anodization current and with anodization time as shown in Figs. 48 and 49.

In order to explain the observed increase in the quantum size effect with etching current we propose the following simple model. To begin with we note that there are at least two types of silicon in the problem: there is bulk silicon at the bottom of the pores which etches rapidly during the anodization, and there is the porous material which we believe has at least one small dimension which etches slowly or not at all.^{3,69,75} Based on earlier studies of the etching mechanism we assume that the etch rate is proportional to the density of holes at the semiconductor electrolyte interface,^{3,75} and that no other factors such as diffusion of reactants are important in determining the etch rate. Consistent with this assumption we further assume, as proposed earlier^{3,69}, that the quantum size effect is a key part of the self-limiting mechanism. The idea is that the etching proceeds until the Si skeleton becomes so thin that there are no holes left in the valence band, because the band edge is quantum shifted away from the hole Fermi energy.

In the experiment the anodization current is found to be proportional to the light intensity, as shown in Fig. 47. This means that the hole density is proportional to the light intensity assuming the reaction rate is proportional to the number of holes at the semiconductor electrolyte interface. In general the density of holes at the semiconductor-electrolyte interface will be proportional to the product of the absorbed optical flux F and the hole lifetime τ . In this case from the usual definition of the Fermi energy, the Fermi energy for holes at the interface between the bulk Si and the electrolyte (position A in Fig. 50) is given by,

$$F\tau = K_1 \exp[-(E_{fp}-E_v)/kT] \quad (24)$$

where K_1 is a constant independent of the light intensity because we have assumed that the hole density is proportional to the light intensity. As shown in Fig. 50, E_{fp} is the quasi Fermi energy for holes and E_v is the energy of the top of the valence band in the bulk Si.

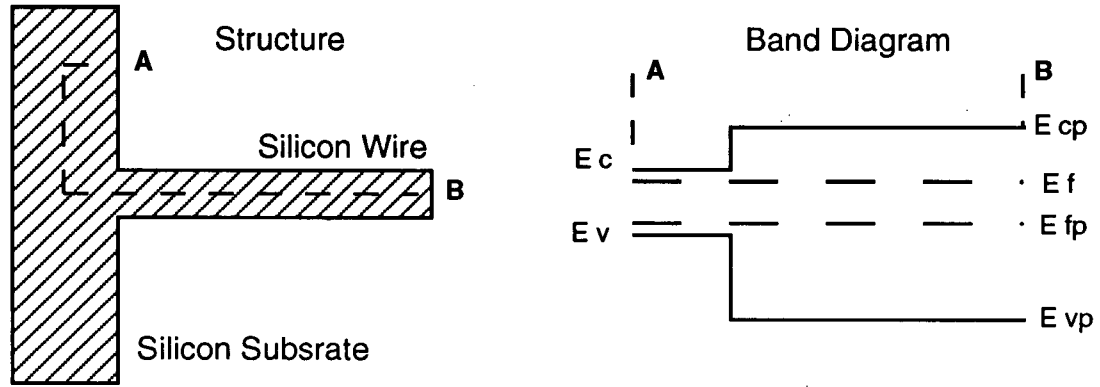


Figure 50: Schematic diagram showing a silicon wire on a bulk Si substrate. An energy band diagram along the line connecting A to B is also shown.

At this point we need a way to estimate the density of holes in the PS. The density of holes will be determined by a balance between the amount of light absorbed in the porous material, the recombination rate of electrons and holes in the PS and the transfer rate of electron-hole pairs between the bulk Si and the PS.⁹⁴ For simplicity we assume that the quasi-Fermi energy for holes is constant in the PS and equal to the quasi-Fermi energy for holes at the surface of the bulk material as shown in Fig. 50. This assumption is valid, for example, in the limit that the electron-hole pair transfer between the PS and the bulk Si is rapid compared with the recombination rate in the PS and the carrier generation rate from the light absorption in the PS. In this case the density of holes, p_{ps} at the surface of the PS (position B in Fig. 50) can be related to the hole Fermi energy in the bulk silicon as follows,

$$p_{ps} = K_2 \exp[-(E_{fp} - E_{vp})/kT] \quad (25)$$

where K_2 is a constant independent of the light intensity and E_{vp} is the energy of the top of the valence band in the PS. We have neglected band bending and surface recombination in the PS. These assumptions are reasonable since the surface of the PS is passivated by hydrogen. The opposite limit, namely slow exchange of electron hole pairs between the PS and bulk Si will be considered in the next section.

If the illumination level is increased during the anodization process there will be an increase in the density of holes at the surface of both the porous and the bulk Si, and the rate of the etching reaction will go up. However as the porous material gets smaller E_{vp} in equation 25 will decrease due to quantum confinement which will reduce the surface hole concentration and slow the etch rate. After an initial transient, the etch rate of the PS will decrease exponentially, as the size scale of the porous material shrinks. In the experimental situation the electrolyte composition and the etching time is held fixed and the light intensity is allowed to vary. For a given etching time, to first approximation the etching rate (or hole density) at the end of the reaction, will be a constant, independent of the illumination level. Although the reaction will proceed further at high illumination levels, the hole density at the end should be approximately independent of the illumination for a fixed etch time. This is the "self-limiting" hole density.

Setting this critical hole concentration equal to another light intensity independent constant K_3 , we can solve equation 24 and 25 for the light intensity dependence of the confinement shift, $\Delta E_v = E_v - E_{vp}$. The result is,

$$\Delta E_v = kT [\ln F + \ln(K_2 \tau / K_1 K_3)] \quad (26)$$

The quantum shift measured in the experiment is actually the conduction band shift ΔE_c and not the valence band shift ΔE_v . However photoemission measurements of the quantum shift in the valence band show that ^{16,86},

$$\Delta E_c = 0.5 \Delta E_v \quad (27)$$

Taking this additional factor of 0.5 into account we obtain the solid line shown in Figs. 48, as the predicted current dependence of the quantum shift in the conduction band. The solid line in Figs. 48 has been shifted along the vertical axis to match the data. The calculated slope is approximately a factor of two smaller than the best fit to the data.

In another experimental situation the illumination intensity or current density is held constant and the etch time is varied. As discussed above we assume that the etching rate is completely determined by the density of holes and is proportional to the density of holes. It follows that if the etch time is scaled up by a factor f , the same PS structure will be obtained provided the hole density is scaled down by the same factor. This means that the PS structure is a function of the product of the hole density (or light flux F) and the etch time, t .

Accordingly the etch time can be incorporated into equation 26 as follows:

$$\Delta E_v = kT [\ln(Ft) + \text{constant}] \quad (28)$$

Taking into account the fact that $\Delta E_v = 2 \Delta E_c$ we find:

$$\Delta E_c = 0.5kT [\ln(Ft) + \text{constant}] \quad (29)$$

In Fig. 49 we plot the conduction band shift as a function of anodization time for two sets of samples prepared at different current densities. In both cases the shift in the conduction band edge increases logarithmically with etching time. The slope of the best fit line to the data was 1.4 kT for the samples prepared at 25 mA/cm² and 1.25 kT for the samples prepared at 10 mA/cm². The slope is a factor of ≈ 3 larger than the solid line with slope 0.5 kT, which is predicted by equation 29.

In this model there will be a maximum quantum shift in the valence band in PS, since the hole Fermi level cannot be made to go below the top of the valence band of the bulk Si with

reasonable dc light intensities. This limit also means that one of the assumptions, namely that the hole density is a linear function of light intensity will breakdown at high light intensities. Accordingly one would expect the bandgap of Si to be the upper limit on the quantum shift in the valence band for PS produced by the electrochemical method. The data in Fig. 48, are consistent with this limit if we convert the conduction band edge shift into the equivalent valence band shift, using equation 27, which gives a maximum valence band shift of 0.7 eV.

7.2.2 Model 2: Porous Silicon Weakly Coupled to Bulk Silicon

Now we consider the opposite limit where the exchange of holes between the PS and the bulk silicon substrate is slow. We assume the density of holes in the PS depends on the light flux F absorbed in the PS, according to the following expression:

$$p_{ps} = F^\gamma \quad (30)$$

This dependence on absorbed flux, where $0.5 < \gamma < 1$ is commonly observed in photoconductors.⁹⁵ Since the bandgap increases as the size scale of the porous material gets smaller, a decreasing portion of the tungsten lamp spectrum will be have an energy high enough to be absorbed in the PS. To account for this effect we write:

$$F = F_0 e^{\frac{-\Delta E_g}{kT_L}} = F_0 e^{\frac{-3\Delta E_v}{2kT_L}} \quad (31)$$

where $T_L = 3000K$ is the temperature of the tungsten lamp, assumed to be much less than E_g/k , and $\Delta E_g = \frac{3}{2}\Delta E_v$ represents the increase in the PS bandgap above that of bulk silicon. If we substitute equations 30 and 31 into equation 25, using the fact that $E_{vp} = E_v - \Delta E_v$, we can write an expression for the PS Fermi energy in terms of the quantum shift in the valence band:

$$E_{fp} = E_v + kT(\ln K_2 - \gamma \ln F_0) + \left(\frac{3}{2}\gamma \frac{T}{T_L} - 1\right)\Delta E_v \quad (32)$$

The density of holes in the PS can now be related to the shift in the valence band by substitution of the energy of the PS Fermi energy into equation 25.

$$p_{ps} = F_0^\gamma e^{-\left(\frac{3}{2}\gamma \frac{\Delta E_v}{kT_L}\right)} \quad (33)$$

The etching will slow as the quantum shift increases the bandgap reducing the number of electron hole pairs produced at a given light intensity. For a given etch time and solution conditions the etching process terminates at a critical value of the hole concentration which we set as a constant K_4 . At the critical hole concentration we solve equation 33 for ΔE_v , and find that the quantum shift is a logarithmic function of the light intensity:

$$\begin{aligned} \Delta E_v &= \frac{2kT_L}{3} \left(\ln F_0 - \frac{1}{\gamma} \ln K_4 \right) \\ \Delta E_c &= \frac{kT_L}{3} \left(\ln F_0 - \frac{1}{\gamma} \ln K_4 \right) \end{aligned} \quad (34)$$

The second equation in (34) is the predicted shift in the conduction band as a function of lamp intensity according to the $\Delta E_v = 2 \Delta E_c$ rule. The dashed line in Fig. 48 is the predicted current dependence of the quantum shift in the conduction band. The calculated slope of the dashed line is approximately a factor of three larger than the best fit to the data.

The time dependence of the quantum shift in this model can be formulated in much the same way as described previously on page 88. This means that the PS structure formed is a function of the product of the hole density (or light flux F) and the etch time, t . The effect of varying the etch time is incorporated into the expression for the critical hole concentration which we set as a constant K_5 .

$$K_5 = p_{ps}t \quad (35)$$

We substitute equation 33, the expression for the hole density in the PS into equation 35 and solve for the time dependence of the quantum shift.

The result is:

$$\Delta E_c = \frac{kT_L}{3\gamma} \ln t + \frac{kT_L}{3} \left(\ln F_0 - \frac{\ln K_5}{\gamma} \right) \quad (36)$$

The predicted relationship between the quantum shift and etch time, for γ equal to 1, is plotted as a dashed line in Fig. 49. The dashed line has been shifted along the vertical axis to match the data of the PS samples etched at 25 mA/cm². We find the slope of this line is approximately 2 times larger than the best fit to the data.

We find both self limiting models predict that the quantum shift should increase in a logarithmic manner with current density and anodization time in agreement with the data. As shown in Figs. 48 and 49, the completely connected model gives slopes too shallow and the completely disconnected model gives slopes too steep, and the actual best fit slope to the data is somewhere in between. This suggests that the actual self limiting mechanism is a combination of the two models, which is perhaps reasonable since there is experimental evidence for both models as discussed below.

A consequence of the self limiting model where the PS is not in electrical contact with the bulk is that the size of the nanostructure should be sensitive to the wavelength of the light illuminating the sample during anodization. That is, the etching process should stop when the bandgap of the PS approaches the illumination photon energy as shown in Fig.51. To test this we have measured the quantum shift of the conduction band edge of the nanostructure phase in PS as a function of the wavelength of the long pass cut-off filters on the lamp used to illuminate the sample during etching. This technique has recently been used during post-anodization soaking to control PL intensity and blue shift.^{96,97}

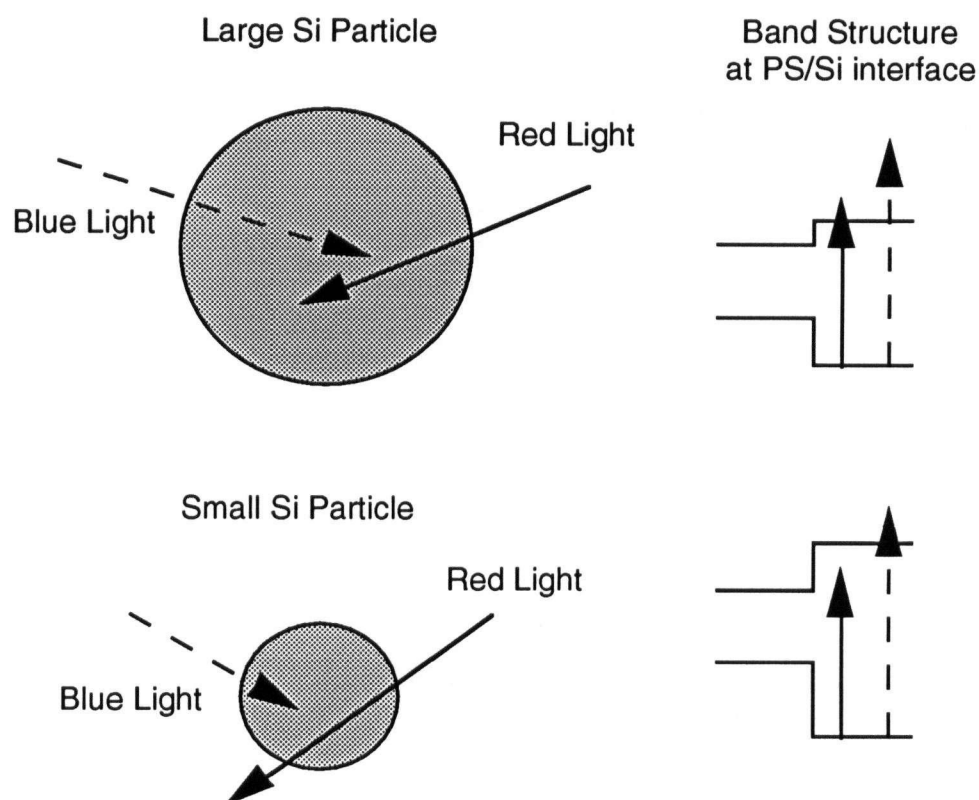


Figure 51: A schematic diagram of the illumination wavelength dependence of the PS etching process.

The Si L-edge absorption is shown in Fig. 52 for PS prepared electrochemically from the same substrate under illumination from light of different maximum photon energies. The current was held constant during the preparation of the PS by adjusting the distance between the sample and the lamp. Notice that the L-edge in the PS is shifted in energy relative to bulk Si and that the shift increases with the frequency of the illuminating light. It has been reported recently that the frequency of illumination also increases the L-edge shift during post anodization HF soaking.⁹⁸ The bandgap of PS can be determined by adding the measured conduction and the predicted

valence band shift to the bandgap of bulk silicon. In Fig. 53 we plot the bandgap of PS as a function of the photon energy of the cut-off filter used with the tungsten-halogen lamp during the electrochemical etching. The solid line with unity slope corresponds to the situation where the bandgap equals the maximum photon energy of illumination. We find a linear relationship between photon energy and the bandgap for both the n-type PS samples (filled circles) and the p+ PS

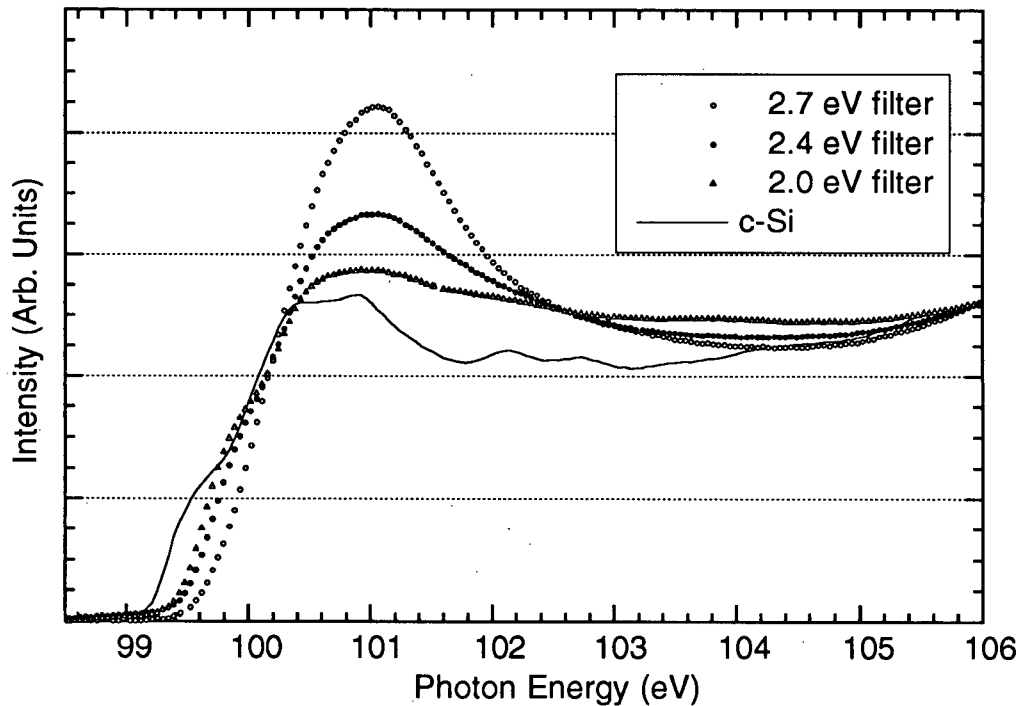


Figure 52: X-ray absorption spectra of bulk n-type (111) Si and n-type PS etched at 25 mA while illuminated by broad spectrum light with maximum photon energies of 2.0, 2.4 and 2.7 eV.

samples (open circles). The bandgaps measured using the 3.6 eV filter did not fall on the line. This may be because the spectrum of the halogen lamp falls off dramatically in this energy region. The bandgap for the n-type PS is at least 0.4 eV less than the photon energy at all points, yet the slope is remarkably close to unity. A bandgap larger than the energy of the illuminating light would be hard to explain. However it is reasonable for the bandgap to be smaller in a systematic manner because the etching reaction will slow down when the size gets close to the illumination

wavelength. It is perhaps surprising that the bandgaps of the p+ samples also show a dependence on the photon energy of the light. A possible explanation is that the PS nanostructure becomes intrinsic once the particle size is small enough.

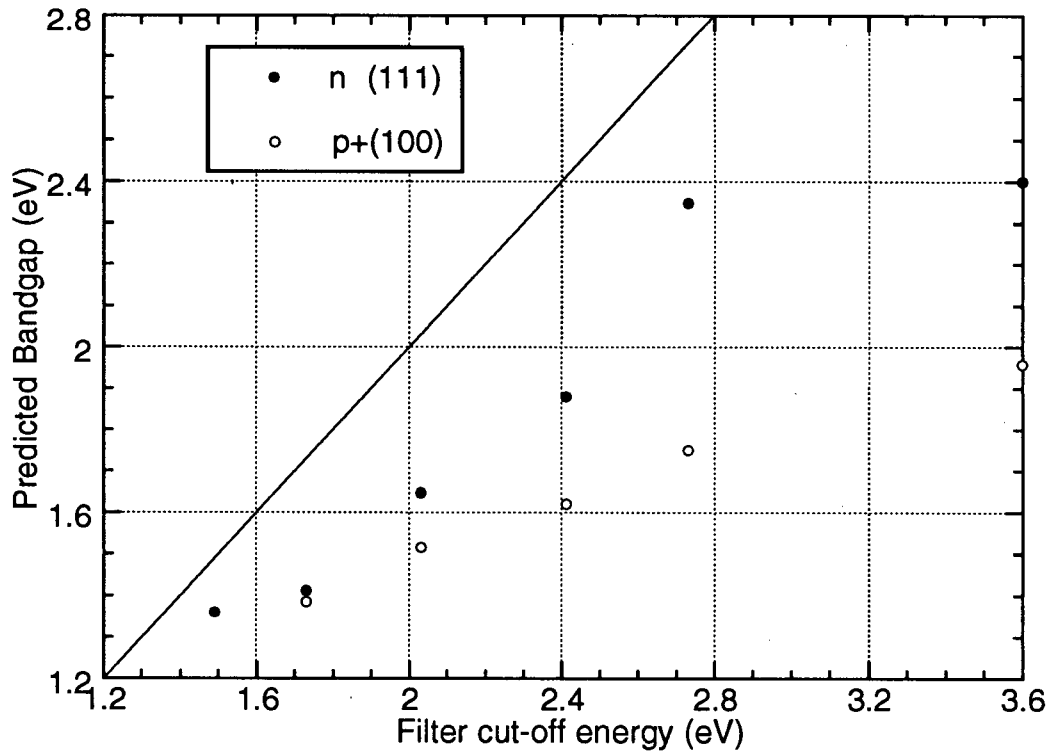


Figure 53: Plot of bandgap as a function of maximum photon energy of illumination during anodization. The n and p+ samples were prepared under the same conditions at $25\text{mA}/\text{cm}^2$ for 15 mins.

7.3 LIMITING FORM OF POROUS SILICON

The self limiting model with rapid hole exchange with the bulk substrate predicts that there will be a maximum quantum shift in the valence band in PS produced by the electrochemical method, since the hole Fermi level cannot be made to go below the top of the valence band of bulk Si. Maximum valence band shifts of approximately 1 eV (the bandgap for Si) would be expected on this basis for PS made from n-type Si. The largest quantum shift in the conduction band edge measured for electrochemically prepared PS is 0.45 eV. (half the valence band shift) This is in good agreement with the predicted maximum conduction band shift of 0.5 eV.

Larger quantum shifts can be obtained by soaking the PS in HF, as shown in Fig. 25 or by the stain etch method as shown in Fig. 29. HF will continue to etch the porous silicon very slowly even in the absence of an external potential as has been reported earlier.^{1,69} Presumably this reaction is similar to the stain etch reaction mechanism. The largest L-edge shift measured for PS sample after a post-anodization HF soak is approximately 0.70 eV. This is the same maximum value measured for stain etch PS samples. Continued post anodization after the L-edge has reached the maximum shift causes the PS structure to dissolve, suggesting a limiting form of PS has been obtained.

The K-edge x-ray absorption of the layered polysilane and PS are found to be remarkably similar. In particular, the K absorption edge of layered polysilane is shifted by 0.6 eV with respect to bulk silicon. This is the same as that of the stain etched PS samples with the maximum conduction band shift as shown in Fig. 40. First principles electronic structure calculations show that Si_6H_6 has a direct band gap of about 3.1 eV.^{99,100} PS with a 0.7 eV conduction band shift should have a band gap of 3.2 eV, using the 2:1 ratio of valence band shift to conduction band shift. Conceivably PS could consist of (111) oriented layers of Si terminated with hydrogen with a chemical formula Si_{6n}H_6 , where n is the number of layers and it depends on the preparation conditions. In this picture layered polysilane (n=1) is the limiting form of PS. If this hypothesis

is proven to be correct , then it explains the close similarity between the x-ray absorption properties of these materials.

7.4 PHOTOLUMINESCENCE

Photoelectron experiments show that the energy of the conduction band and valence band edges in PS depends on the conditions used in the synthesis of the material and on treatment after preparation.^{16,65,87} Since photoelectron spectroscopy involves the collection of low energy electrons emitted from the material it is inherently surface sensitive. Consequently in an inhomogeneous material such as PS, the results of the photoelectron spectroscopy may not be directly comparable with the more bulk sensitive optical techniques such as photoluminescence (PL). We compare the peak energy of the room temperature PL of PS with the bandgap determined from the photoelectron spectroscopy measurements for a series of PS samples prepared under different conditions.

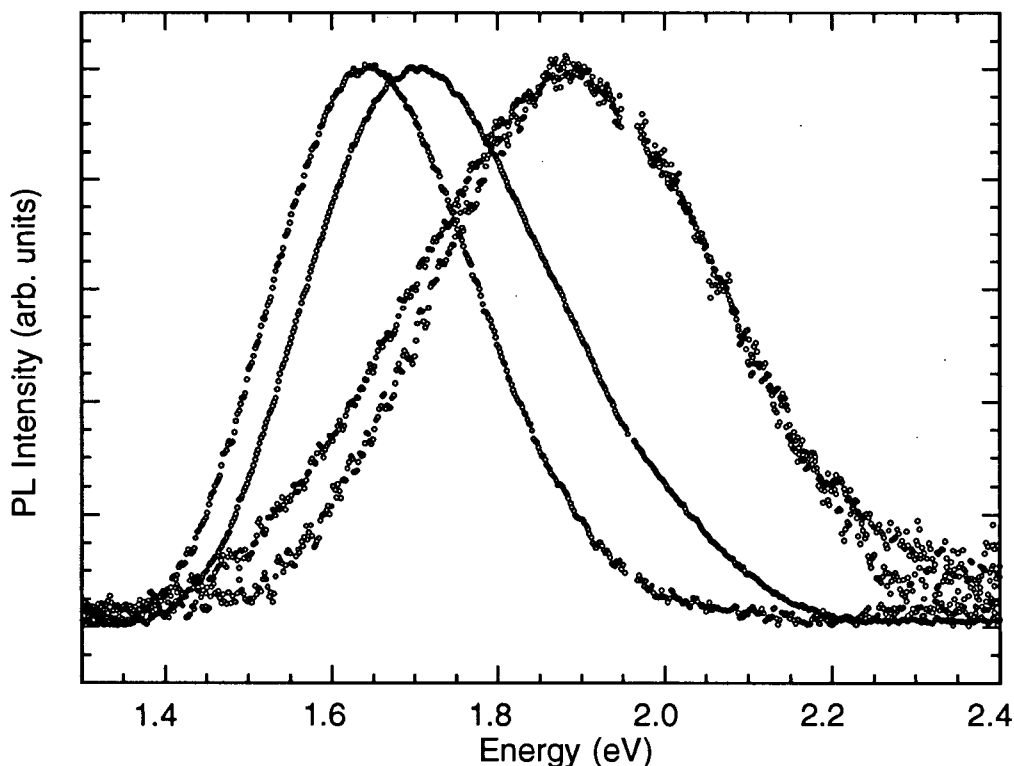


Figure 53: PL spectra from n-type PS samples prepared using current densities of (left to right) 0.6, 10, 30, and 60 mA/cm². The 60 mA/cm² sample peaks at the same energy as the 30 mA/cm² sample but has a larger FWHM. The PL intensity has been normalized for easier comparison.

The samples were prepared by electrochemical anodization of p and n-type silicon at constant current. The electronic properties of the PS made from the n-type material were modified by changing the current density during anodization. A p-type sample, anodized at 1mA/cm^2 for 3 hours, was modified after preparation by soaking in HF for varying lengths of time. PL spectra for a series of PS samples prepared with different current densities and HF soak times are shown in Figs. 53 and 54 respectively. The PL spectra are normalized to correct for the spectral dependence of the throughput of the interferometer. To facilitate comparisons the PL spectra have been scaled to the same value at the peak.

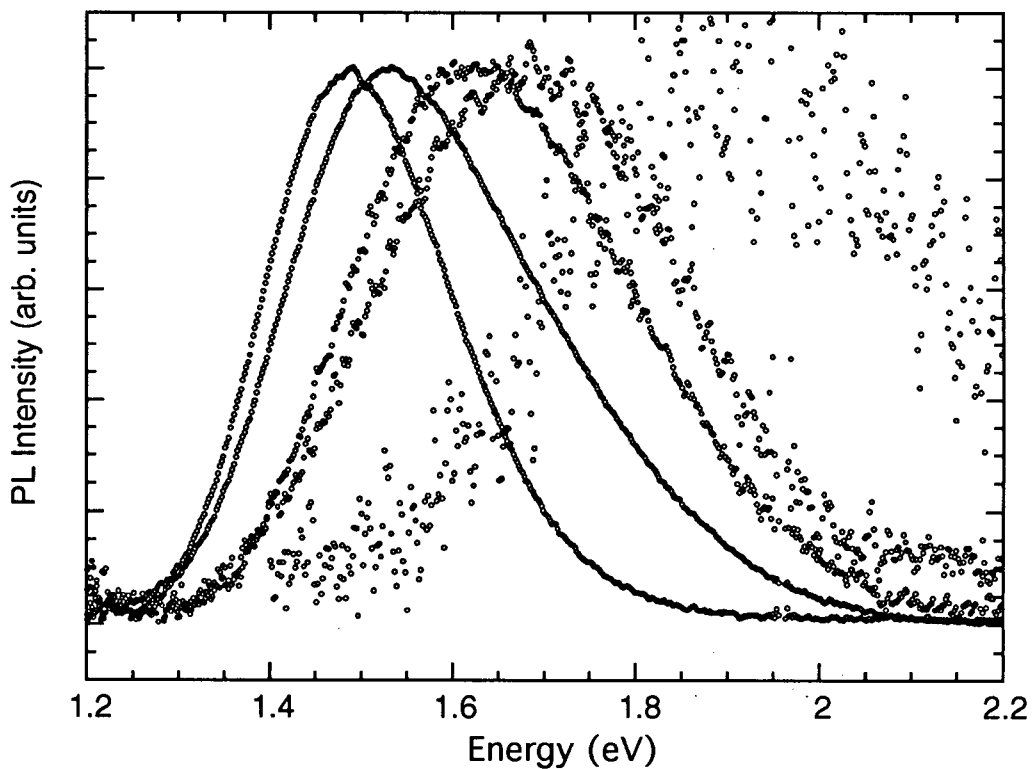


Figure 54: PL spectra from p-type PS samples. Parts of an initial sample prepared with a current density of 1mA/cm^2 were soaked in HF for (from left to right) 0, 60, 120, 180, and 240 min. The PL intensity has been normalized for easier comparison.

Qualitatively the L-edge absorption and the PL spectra show the same behavior with increasing current density (Fig. 24) and increasing soak time (Fig. 25), namely a shift to higher energy. In contrast to PL and optical absorption in the visible range, which involve transitions between the top of the valence band and the bottom of the conduction band, the L-edge absorption is sensitive only to the conduction band and not to the valence band since the initial state in the x-ray absorption is the Si 2p core level. To compare the PL data with the L-edge emission we also need information about the valence band. As discussed earlier we approximate the change in the VB edge by,^{16,86}

$$\Delta E_v = 2.0 \Delta E_c \quad (37)$$

If we use the factor of 2 to relate the valence band shift to the L-edge shift we obtain a "photoelectron bandgap" from the L-edge absorption, which can be compared with the PL spectrum. In Fig. 55 we plot the energy and the halfwidth of the peak in the PL spectrum as a function of the bandgap obtained by photoelectron spectroscopy for the series of PS samples in Figs.53 and 54 above. Although the energy of the PL emission shows a similar increase with current density and soak time as the photoelectron bandgap the PL bandgap is consistently lower as shown in Fig. 55. PL emission is expected to be at photon energies below the bandgap found from absorption type measurements, since the optically excited electrons and holes can thermalize to lower energy states by diffusion to regions with smaller bandgap before they recombine radiatively. In addition, PL probes the material to depths of 100's of nanometers set by the penetration depth of the 457nm excitation light whereas the photoelectron spectroscopy is sensitive to depths of 10's of nanometers given by the escape depth of the photoelectrons. In porous silicon one might expect the outer part of the material to have a larger quantum shift since the surface is exposed to the anodizing reaction longer than the material deeper inside and therefore may be expected to have a smaller microstructure. On this basis as well one would expect the photoelectron bandgap to be larger than the PL bandgap.

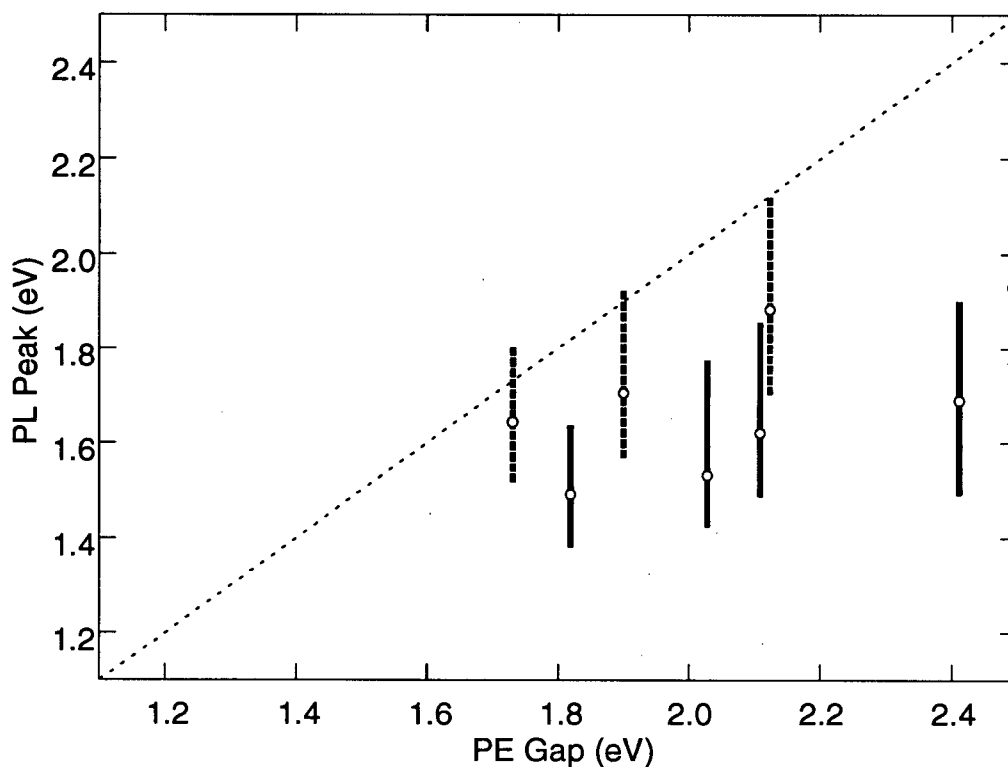


Figure 55: PL peak positions (marker) and spectral width (length of the bars) as a function of the bandgap as determined from photoelectron spectroscopy (PE gap). Solid bars represent HF soaked samples (Fig. 48) while dashed bars correspond to samples prepared with different current densities (Fig. 47). On the dashed line the PL peak position equals the PE gap.

Given the above arguments it is interesting to note that some of the PL emission is at higher energy than the photoelectron bandgap. This is not inconsistent with the photoelectron spectroscopy results since in an inhomogeneous sample the parts of the sample with the lowest energy absorption will dominate the absorption threshold and tend to give a lower limit for the bandgap.

As shown in Fig. 53 and 54 in addition to the increase in the peak energy in the PL the width of the PL emission band also increases with the current density and soak time. The full width at half maximum obtained from Gaussian fits to the emission spectra are plotted in Fig. 55 as a function of the corresponding photoelectron bandgaps. The increase in width is consistent with the

change in the shape of the L-edge absorption with increasing blue shift as illustrated in Fig. 24. The L-edge for the bulk Si sample has distinct double edge feature associated with the 0.6eV spin orbit splitting of the 2p core level. This feature becomes progressively less distinct with increasing blue shift in the L-edge in PS. The shape of the L-edge in PS can be simulated by convoluting the bulk Si L-edge with a Gaussian of increasing width as the blue shift increases as shown in Fig. 56. The width of the Gaussian broadening function used to simulate the data is set equal to the width of the PL emission spectrum, while the energy offset of the Gaussian causing the shift up in energy is determined from the quantum shift observed in the PL spectra taking the 1:2 ratio for the conduction to

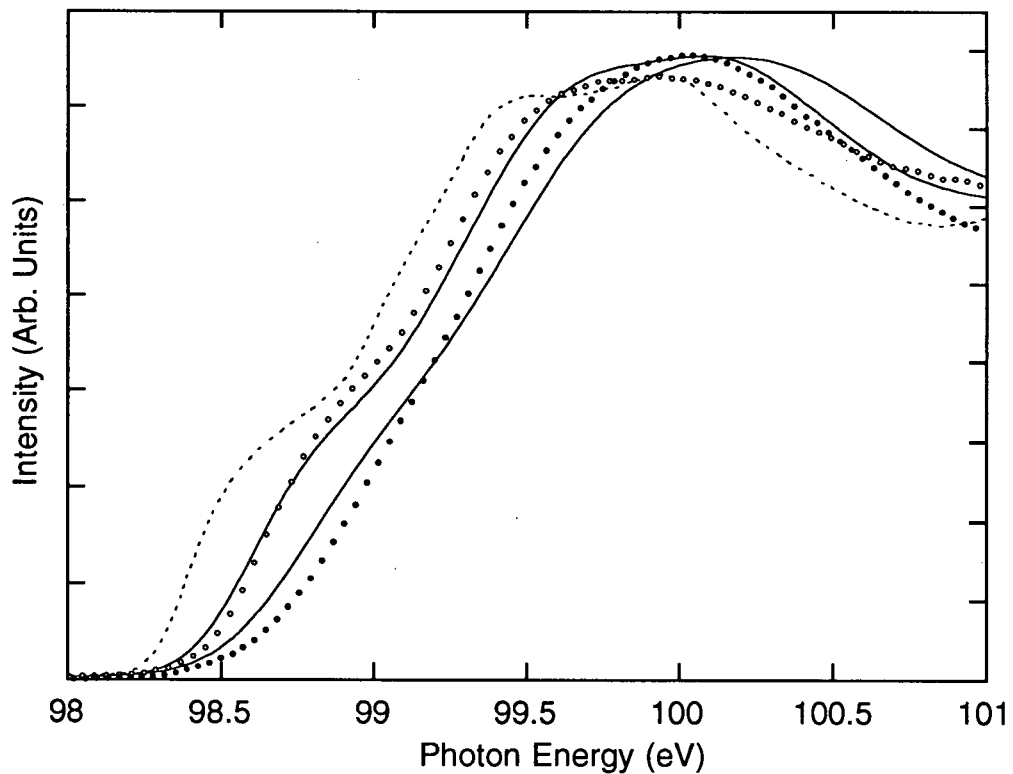


Figure 56: X-ray absorption spectra shown in Fig.24 normalized at the absorption peak. The solid lines model the PS absorption edge. They were obtained by convoluting the spectrum of crystalline Si with Gaussian whose width and energy shifts were determined from the corresponding PL spectra as discussed in the text.

valence band quantum shifts. Discrepancies between model and experiment may be to some extent due to the fact that the width of the PL spectrum arises from inhomogeneous broadening of both the conduction and valence bands whereas the L-edge is only sensitive to the conduction band.

It is interesting to speculate on the origin of the increase in the width of the PL emission band and the broadening of the L-edge absorption with increasing blue shift. The simplest explanation for the width of the PL emission band is that it is inhomogeneous broadening due to the size distribution of the microstructure. As the microstructure shrinks the effect on the quantum confinement energy of a given fluctuation in the dimension of the microstructure increases. As an easy to calculate example of this effect we assume that the PS is made up of (111) oriented 2D Si microsheets terminated at the surface by Si-H bonds. In this case the minimum dimensional fluctuation will be a change in the thickness of the sheet by one hexagonal (111) layer of silicon atoms. If the average 2D sheet contains N layers then it is reasonable to expect a minimum thickness fluctuation of $N \pm 1$ layers if both surfaces of the sheet have the minimum fluctuation. Of course this interpretation neglects the effect on the width of the PL emission band of carrier relaxation in the semiconductor to low energy locations. This model has the virtue of reproducing the correct value for the maximum bandgap that has been measured in PS namely the bandgap of a single (111) sheet (layered polysilane).^{69,99,100}

The bandgap of (111) oriented silicon wafers as a function of thickness can be estimated using an effective mass theory. In this approximation the sum of the quantum shifts in the conduction and valence bands is given by ⁷⁵,

$$\Delta E = \Delta E_c + \Delta E_v = \frac{\hbar^2 \pi^2}{2 L^2} \frac{1}{3} \left(\frac{2}{m_t^*} + \frac{1}{m_l^*} \right) + \frac{\hbar^2 \pi^2}{2m_0 L^2} \frac{1}{3} (k + 2m) \quad (38)$$

for a sheet of thickness L . The curvature of the conduction bands is described by longitudinal and transverse effective masses, m_t^* , m_l^* and that of the valence band by the effective mass parameters k and m .⁷⁵ The full width at half maximum, W , of the PL peaks due to thickness fluctuations is,

$$W = 2(\Delta L) \frac{d}{dL}(\Delta E) \quad (39)$$

where ΔL is the monolayer thickness of 3.13\AA . We find the following relationship in electron volts, between W and ΔE :

$$W = 0.74(\Delta E)^2 \quad (40)$$

This simple result gives a remarkably good fit to the width of the PL spectrum as shown in Fig. 57.

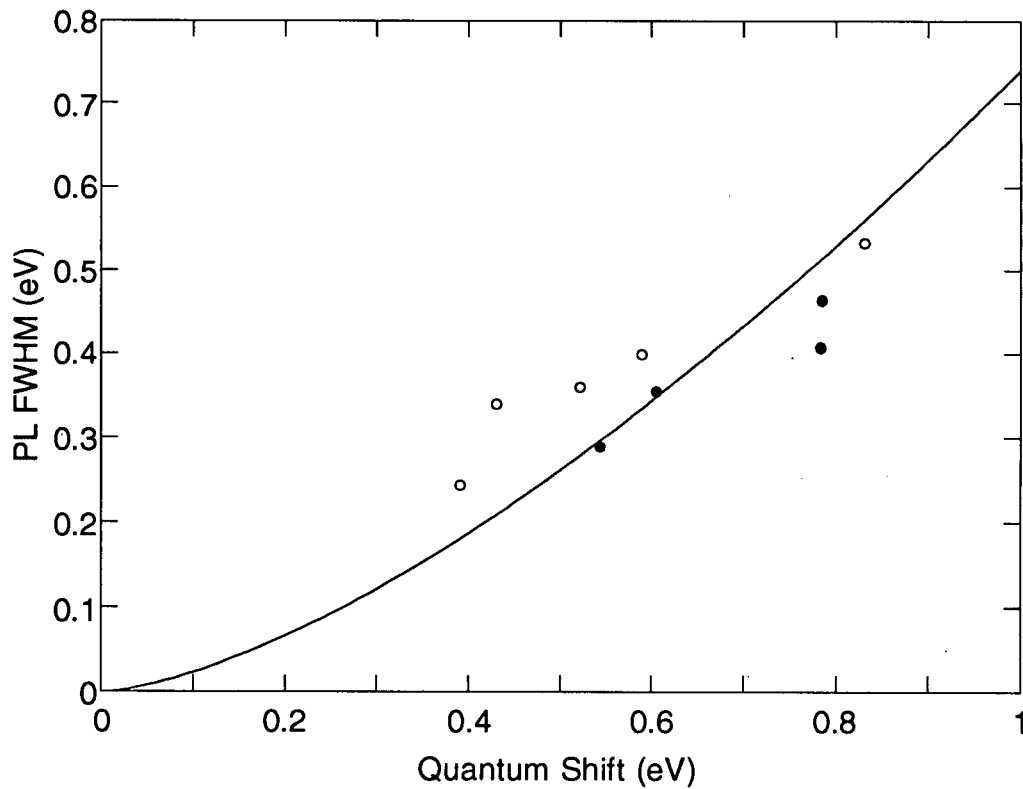


Figure 57: FWHM of the PL spectra as a function of the quantum shift ΔE , defined as the PL peak position minus 1.1 eV, the Si bandgap energy. Open circles indicate HF soaked samples (Fig. 48) while filled circles indicate samples produced using different current densities (Fig. 47). The solid line is an effective mass model for the expected PL width from hydrogen terminated Si (111) sheets.

8. CONCLUSIONS

In conclusion we find that x-ray absorption measurements at the Si K and L-edge are a sensitive probe of the quantum confinement effects in the conduction band of PS. We show for the first time a blue shift in the x-ray absorption spectrum of PS when compared to bulk silicon. The blue shift can be explained in terms of quantum confinement which raises the bottom of the conduction band, consequently the absorption threshold will increase by the same amount. Our x-ray absorption measurements suggest that the size of the nanostructure can be controlled by such things as the anodization current density, anodization time, photon energy of light illuminating the sample during anodization and post anodization soaking in HF solution. The x-ray absorption spectra also show an excitonic enhancement at the Si L edge in PS which increases with the quantum shift in the L-edge absorption. The enhanced excitonic absorption is in agreement with the expectation that electron-hole interactions increase in silicon nanocrystals due to confinement effects, and is consistent with the high luminescence efficiency in PS. Differences in the electronic structure of the conduction band between bulk silicon and PS are understood qualitatively using a simple LCAO model. In particular we can understand the blue-shifting of the conduction band minimum in PS for both L and K edges. This model also explains the steeper onset of the K-edge spectrum for porous silicon as compared to the bulk.

PES data show that the valence band of porous silicon is also shifted relative to the bands for bulk silicon, and the shift is dependent on how the PS is prepared. The quantum shift in the valence band is larger than the shift in the conduction band and is proportional to it with a proportionality constant of 2.0 that is independent of preparation conditions. This agrees with the quantum confinement model for PS which predicts that the energies of the valence and conduction band should be correlated and depend on the size of the Si microstructure. The quantum confinement shifts have been estimated using a simple effective-mass approximation where we neglect the spin orbit splitting. In this effective mass model the ratio of valence to conduction band edge shifts is 1.48 for a (100) oriented wire with square cross section, 1.42 for a (100)

oriented box. Similarly the ratios are 1.42, 1.48, and 4.4 for a sheet oriented in the (111), (110) and (100) directions respectively. More sophisticated pseudopotential calculations give a ratio of valence to conduction band edge shifts of 1.8 for (100) oriented sheet and 2.0 for a spherical quantum dot rather different than the effective mass calculation but in good agreement with the experimental data.

The Si LVV Auger electron spectrum provides an alternative measurement of the quantum shift in the valence band of PS. We find that the maximum kinetic energy of an Auger electron from the PS will be lower than in crystalline silicon by a factor of $2(\Delta E_{vb})$. The reason for the factor of two is that the ejected Auger electron comes from a valence band with a larger minimum binding energy while at the same time the electron that drops into the 2p core level has less excess energy to dissipate since it comes from the quantum shifted porous silicon valence band.

An independent confirmation of the relationship between the quantum shifts in the valence and conduction band edges is obtained from the PS annealing experiments. The quantum shifts in the conduction and valence band edges of PS relative to bulk Si are found to decrease with progressively higher annealing temperatures, up to 550°C, at which point the band edge energies revert to the values for bulk Si. These results suggest that the PS nanostructure collapses with an increase in the PS particle size in the temperature range between 400 and 500°C where the surface hydrogen evolves. The ratio of the shift in the valence band edge to the shift in the conduction band edge remains approximately constant with annealing and equal to 1.9, in agreement with the ratio determined as a function of preparation conditions. The fact that the ratio of the valence band shift to the conduction band shift remains constant during annealing suggests that the quantum shift in the two band edges is not sensitive to the geometric shape or crystallographic orientation of the microstructure of the PS. We conclude from the study of thermal annealing of porous silicon that the changes in the conduction and valence bands, and the hydrogen evolution are all consistent with a quantum confinement model for the optical properties in which H passivation of the surface of the nanostructures plays a critical role in the high luminescence efficiency.

Measurements of the Si L-edge have proven a useful way to probe the effects of different preparation procedures on the electronic structure of PS. In particular we explore the hypothesis that the self limiting behavior of the etching process is caused by a reduction in the number of holes at the semiconductor-electrolyte interface when the dimension of the silicon microstructure in the porous material is small enough to produce a quantum shift in the valence band. Two models have been proposed to explain the logarithmic dependence of the quantum shift on the anodization current (light intensity) and the anodization time. In the first model we assume that the photogenerated holes in PS are in thermal equilibrium with bulk silicon. In other words the PS is completely connected to the bulk silicon. In the second model we assume the opposite limit where the photogenerated holes in the PS are isolated from the bulk silicon. Although both models predicted a logarithmic dependence of the quantum shift with anodization current and etch time, neither model exactly fit the data. The completely connected model predicts quantum shifts that are too small and the weakly connected model predicts quantum shifts that are too large. We find the actual results is somewhere in between the two models. This suggests that the actual form of the self limiting etch mechanism is a combination of the two models.

The peak in the photoluminescence spectra for a series of porous silicon samples have been compared with photoelectron spectroscopy measurements of the band edge quantum shifts. The peak in the PL spectrum and the bandgap determined from photoelectron spectroscopy show a similar variation with preparation conditions although the PL peak is lower in energy than the gap determined from photoelectron spectroscopy. Both the PL and the L-edge absorption show an increase in inhomogeneous broadening with increasing quantum shift. This increase is consistent with an effective mass theory for quantum confinement in 2D silicon sheets with one atomic layer fluctuations in the surface topography.

An alternative explanation for the visible PL is emission from a surface siloxene ($\text{Si}_6\text{H}_6\text{O}_3$) layer which is peaked near 550 nm. The structure is known to consist of Si (111) layers terminated above and below by OH groups and H atoms. It has been proposed that the shift in the PL peak with preparation conditions could be caused by a heat-treated form of siloxene. This is

difficult to reconcile with photoelectron experiments which show that freshly prepared PS does not contain oxygen. Recently an oxygen-free form of siloxene (Si_6H_6) called layered polysilane has been synthesized. The x-ray absorption of the layered polysilane and PS are found to be remarkably similar. In particular, the K absorption edge of layered polysilane is shifted by 0.6 eV with respect to bulk silicon. This is the same as that of the PS samples with the maximum conduction band shift. First principles electronic calculations show that Si_6H_6 has a bandgap of about 3.1 eV. PS with a 0.7 eV conduction band shift should have a band gap of 3.2 eV, using the 2:1 ratio of valence band shift to conduction band shift. These results suggest that PS is composed of a Si_{6n}H_6 silicon layer sandwich structures with small n . As the PS is etched a the number of layers decreases, a limiting form of PS is obtained which occurs when $n=1$.

These results show how PS is a useful model system for explaining dimensional effects in Si nanostructures.

9. REFERENCES

1. L. T. Canham, *Appl. Phys. Lett.* **57**, 1046 (1990)
2. A. G. Cullis, L. T. Canham, *Nature*, **353**, 335 (1991).
3. V. Lehmann, and U. Gosele, *Appl. Phys. Lett.* **58**, 856 (1991).
4. V. Lehmann, and U. Gosele, *Adv. Mater.* **4**, 114 (1992)
5. M.I.J. Beale, J.D. Benjamin, M.J. Uren, N.G. Chew and A.G. Cullis, *J. Cryst. Growth* **73**, 622 (1985).
6. R.W. Hardeman, M.I.J. Beale, D.B. Gibson, J.M. Keen, C. Pickering and D.J. Robbins, *Surf. Sci* **152**, 1051 (1985)
7. V. Lehmann, *J. Electrochem. Soc.* **140**, 2836 (1993).
8. A. Uhler, *Bell Syst. Tech. J.* **35**, 333 (1956).
9. T. Unagami *Jpn. J. Appl. Phys.* **19**, 231 (1980).
10. C. Pickering, M.I.L. Beale, D.J. Robbins, P.J. Pearson, R. Greef, *J. Phys. C* **17**, 6543 (1984).
11. S.M. Prokes, O.J. Glembocki, V.M. Bermudez, R. Kaplin, L.E. Friedersdorft and P.C. Searson, *Phys. Rev. B* **45**, 13788 (1992).
12. M. Stutzmann, J. Weber, M. S. Brandt, H. D. Fuchs, M. Rosenbauer, P. Deak, A. Hopner, A. Breitschwerdt, *Advances in Solid State Physics*, **32**, 179 (1992).
13. P. Deak, M. Rosenbauer, M. Stutzmann, J. Weber, M. S. Brandt, *Phys. Rev. Lett.* **69**, 2531 (1992).
14. I. Sagnes, A. Halimaoui, G. Vincent, P. A. Badoz, *Appl. Phys. Lett.* **62**, 1155 (1993).
15. T. van Buuren, Y. Gao, T. Tiedje, J. R. Dahn, B. M. Way, *Appl. Phys. Lett.* **60**, 3013 (1992).
16. T. van Buuren, T. Tiedje, J. R. Dahn, B. M. Way, *Appl. Phys. Lett.* **63**, 2911 (1993).
17. P.D.J. Calcott, K.J. Nash, L.T. Canham, M.J. Kane, D. Brumhead, *J. Lumin.* **57** 257 (1994).

18. D.J. Lockwood, A. Wang, B. Bryskiewicz, *Solid State Commun.* **89**, 587 (1994).
19. Y. Kanemitsu, H. Uto, Y. Masumoto, T. Matsumoto, T. Futagi, H. Mimura, *Phys. Rev. B* **48**, 2827 (1993).
20. P.M. Fauchet, to be published *J. Lumin.* (1996).
21. V. Petrova-Koch, T. Muschik, *Thin Solid Films* **255**, 246 (1995).
22. V. Lehmann, *Thin Solid Films* **255**, 1 (1995).
23. K.H. Tan, G.M. Bancroft, L.L. Coatsworth and B.W. Yates, *Can. J. Phys.* **60**, 131 (1982).
24. W. Gudat, C. Kunz, *Phys. Rev. Lett.* **29**, 169 (1972).
25. M.P. Seah and W.A. Dench, *Surface Interface Analysis* **1**, 2 (1979).
26. B.X. Yang, F.H. Middleton, B.G. Olsson, G.M. Bancroft, J.M. Chen, T.K. Sham, K.H. Tan and D.J. Wallace, *Nucl. Instrum. Methods A* **316**, 422 (1992).
27. M. Sansone, R. Hewitt and W. Eberhardt, *Nucl. Instrum. Methods A* **266**, 422 (1988).
28. P.C. Searson, J.M. Macaulay and F.M. Ross, *J. Appl. Phys.* **72**, 253 (1992).
29. A. Halimaoui, *Appl. Phys. Lett.* **63**, 1264 (1993).
30. J. Von Behren, L. Tsybeskov and P.M. Fauchet, *Microcrystalline and Nanocrystalline Semiconductors*, *Mat. Res. Soc. Proc.* **358**, (1995).
31. P.C. Searson, *Appl. Phys. Lett.* **59**, 832 (1991).
32. H. Foll, *Appl. Phys. A* **53**, 8 (1991).
33. X.G. Zhang, S.D. Collins and R.L. Smith, *J. Electrochem. Soc.* **136**, 1561 (1989).
34. R.L. Smith and S.D. Collins, *J. Appl. Phys.* **71**, R1 (1992).
35. R.J. Archer, *J. Phys. Chem. Solids* **12**, 104 (1960).
36. M.I.J. Beale, J.D. Benjamin, M.J. Uren, N.G. Chew and A.G. Cullis, *J. Cryst. Growth* **75**, 408 (1986).
37. S.K. Ghandi, *VLSI Fabrication Principles* (Wiley, New York, 1983) pp 478-482.
38. R.W. Fathauer, T. George, A. Ksendzov and R.P. Vasquez, *Appl. Phys. Lett.* **60**, 995 (1992).
39. F. Wohler, *Leibigs Ann. Chem.* **127**, 257 (1863).

40. H. Kautsky, *Z. Anorg. Allem. Chem.* **117**, 209 (1921).
41. J.R. Dahn, B.M. Way, E.W. Fuller, W.J. Weydanz, J.S. Tse, D.D. Klug, T. van Buuren and T. Tiedje, *J. Appl. Phys.* **75**, 1946 (1993).
42. J.R. Dahn, B.M. Way, E. Fuller and J.S. Tse, *Phys. Rev. B* **48**, 17872 (1993).
43. S.F. Chung, S.D. Collins and R.L. Smith, *Appl. Phys. Lett.* **55**, 675 (1989).
44. A. Nakajima, Y. Ohshima, T. Itakura, and Y. Goto, *Appl. Phys. Lett.* **62**, 2631 (1993).
45. M.W. Cole, J.F. Harvey, R.A. Lux, D.W. Eckart and R. Tsu, *Appl. Phys. Lett.* **60**, 2800 (1992).
46. R. Tsu, H. Shen and M. Dutta, *Appl. Phys. Lett.* **60**, 6 (1992).
47. D.J. Lockwood, A.G. Wang, *Solid State Commun.* **94**, 905 (1995).
48. A.A. Lomov, D. Bellet, G. Dolino, *Phys. Stat. Sol. B* **190**, 219 (1995). , D.Bellet, S. Billat, G. Dolino, M. Ligeon, C. Meyer and F. Muller, *Solid State Commun.* **86**, 51 (1993).
49. S. Gardelis, U. Bangert, A.J. Harvey and B. Hamilton, *J. Electrochem. Soc.* **142**, 2094 (1995).
50. D.Bellet, S. Billat, G. Dolino, M. Ligeon, P. Blanc, M. Krisch, *J. Appl. Phys.* **71**, 145 (1992).
51. A. Guinier, *X-ray Diffraction in Crystals, Imperfect Crystals, and Amorphous Bodies* (W.H. Freeman and Company, San Francisco, 1963).
52. E. Koppensteiner, A. Schuh, G. Bauer, V. Holy, D. Bellet, and G. Dolino, *Appl. Phys. Lett.* **65**, 1504 (1994).
53. V. Lehmann, B. Jobst, T. Muschik, A. Kux and V. Petrova-Koch, *Jpn. J. Appl. Phys.* **32**, 2095 (1993).
54. V. Vezin, P. Goudeau, A. Naudon, A. Halimaoui and G. Bomchil, *Appl. Phys. Lett.* **60**, 2625 (1992).
55. W. Eberhardt, G. Kalkoffen, C. Kunz, D. Aspnes and M. Cardona, *Phys. Stat. Sol.* **88**, 135 (1978)
56. F.C. Brown, R.Z. Bachrach, M. Skibowski, *Phys. Rev. B* **15**, 4781 (1977).

57. G.R. Harp, Zhi-Lan Han and B.P. Tonner, *Physica Scripta* **T31**, 23 (1990)
58. B. Abeles, I. Wagner, W. Eberhardt, J. Stohr and H. Stasiewski, *Optical Effects in amorphous Semiconductors*, edited by P.C. Taylor and S.G. Bishop (American Institute of Physics, New York, 1984), p.394.
59. A. Bianconi, R. Del Sole, A. Selloni, P. Chiaradia, M. Fanfoni and I. Davoli, *Solid State Commun.* **64**, 1313 (1987).
60. S. Patitsas, T. van Buuren, T. Tiedje, *J. Electrochem. Soc.* to be published 1996.
61. D.A. Papaconstantopoulos, *Handbook of the band structure of Elemental Solids*, (Plenum, New York, 1986).
62. L. Yang, B. Abeles, W. Eberhardt, H. Stasiewski and D. Sondericker, *Phys. Rev. B* **35**, 9395 (1987).
63. Z.H. Lu, D.J. Lockwood and J.M. Baribeau, *Nature* **378**, 258 (1995).
64. T.K. Sham, X.H. Feng, D.T. Jiang, B.X. Yang, J.Z. Xiong, A. Bzowski, D.C. Houghton, B. Bryskiewicz and E. Wang, *Can. J. Phys.* **70**, 813 (1992)
65. T. van Buuren, T. Tiedje, S.N. Patitsas, C. D. W. Jones, *Proc. of 22 ICPS*, edited by D.J. Lockwood (World Scientific, Singapore, 1994) p.2125.
66. D.G.J. Sutherland, G.M. Bancroft, J.D. Bozek and K.H. Tan, *Chem. Phys. Letters* **199**, 341 (1992).
67. St. Frohnhoff, M.G. Berger, M. Thönissen, C. Dieker, L. Vescan, H. Münder and H. Lüth, *Thin Solid Films* **255**, 59 (1995).
68. H. Aoyagi, A. Motohashi, A. Kinoshita, T. Aono and A. Satou, *Jpn. J. Appl. Phys.* **32**, L1 (1993).
69. T. van Buuren, T. Tiedje, W. Weydanz, *Mat. Res. Soc. Proc.*, Vol. **298**, 283 (1993).
70. J.K. Kidder, Jr. P.S. Williams, T.P. Pearsall, D.T. Schwartz, and B.Z. Nosho, *Appl. Phys. Lett.* **61**, 2896 (1992).
71. M. Nakazawa, Y. Nishioka, H. Sekiyama, S. Kawase, *J. Appl. Phys.* **65**, 4019 (1989).
72. G. Hollinger, F.J. Himpsel, *J. Vac. Sci. Technol.* **A1**, 640 (1983).

73. J. J. Yeh, I. Lindau, *Atomic Data Nuclear Data Tables* **32**, 1 (1985).
74. L. Ley, in the *Physics of Hydrogenated Amorphous Silicon*, edited by J.D. Joannopoulos and G. Lucovskyy (Springer, Berlin, 1994), Vol. II, p. 98.
75. M. Voos, Ph. Uzan, C. Delalande, G. Bastard, A. Halimaoui, *Appl. Phys. Lett.* **61**, 1213 (1992).
76. M.S. Brandt, H.D. Fuchs, M. Stutzmann, J. Weber, and M. Cardona, *Solid State Commun.* **81**, 307 (1992).
77. I. Hirabayashi, K. Morigaki and S. Yamanaka, *J. Non-Crystall. Solids* **59&60**, 645 (1983).
78. R. S. Bauer, R. Z. Bachrach, *J. Vac. Sci. Technol.* **17**, 509 (1980).
79. S. L. Friedman, M. A. Marcus, D. L. Adler, Y. H. Xie, T. D. Harris, P. H. Citrin *Appl. Phys. Lett.* **62**, 1934 (1993).
80. T.K. Sham, D.T. Jiang, I. Coulthard, J.W. Lorimar, X.E. Fang, K.H. Tan, S.P. Frigo, R.A. Rosenberg, D.C. Houghton and B. Bryskiewicz, *Nature* **363**, 331 (1993)
81. H. Ubara, T. Imura, A. Hiraki, I. Hirabayashi and K. Morigaki, *J. Non-Crystall. solids* **59&60**, 641 (1983).
82. V. Petrova-Koch, T. Muschik, A. Kux, B.K. Meyer, F. Koch and V. Lehmann, *Appl. Phys. Lett.* **61**, 943 (1992).
83. C. Tsai, K. H. Li, J. Sarathy, S. Shih, J. C. Campbell, B. K. Hance, J. M. White, *Appl. Phys. Lett.* **59**, 2814 (1991).
84. M. B. Robinson, A. C. Dillon, D. R. Haynes, and S. M. George, *Appl. Phys. Lett.* **61**, 1414 (1992).
85. P. Gupta, V. L. Colvin, and S. M. George, *Phys. Rev. B* **37**, 8234 (1988).
86. T. van Buuren, T. Tiedje, S. N. Patitsas, W. Weydanz, *Phys. Rev. B* **50** 2719 (1994).
87. S. Eisebitt, T. Van Buuren, J. E. Rubensson, J. Lunning, T. Tiedje, W. Eberhart, *Proc. of 22 ICPS*, edited by D.J. Lockwood (World Scientific, Singapore, 1994) p.2133.

88. S. Eisebitt, J. Lüning, J.-E. Rubensson, T. van Buuren, S. N. Patitsas, T. Tiedje, M. Berger, R. Arens-Fischer, S. Frohnhoff, and W. Eberhardt, to be published Solid State Comm., Sept.1996.
89. S.B. Zhang, Alex Zunger, Appl. Phys. Lett. **63**, 1399, (1993).
90. L.W. Wang and Alex Zunger, Nanocrytalline Semiconductor Materials, edited by P.V. Kamat, D. Meisel (Elsevier Science, 1996).
91. D.G.J. Sutherland, G.M. Bancroft, K.H. Tan, Surface Sci. Letters **262**, L96 (1992).
92. J.L. Batstone, M.A. Tischler, and R.T. Collins, Appl. Phys. Lett. **62**, 2667 (1993).
93. V. V. Doan, M. J. Sailor, Science **256**, 1791 (1992).
94. N. Noguchi, I. Suemune, Appl. Phys. Lett. **62**, 1429 (1993).
95. A. Rose, *Concepts in Photoconductivity*, Krieger & Sons (1978).
96. H. Koyama, N. Koshida, J. Appl. Phys. **74**, 6365 (1993).
97. H. Koyama, T. Nakagawa, T. Ozaki and N. Koshida, Appl. Phys. Lett. **65**, 1656 (1994).
98. Y. Suda, T. Ban, T. Koizumi, H. Koyama, Y. Tezuka, S. Shin and N. Koshida, Jpn. J. Appl. Phys. **33**, 581 (1994).
99. C. G. van der Walle, J. E. Northrup, Phys. Rev. Lett. **70**, 1116 (1993).
100. J. S. Tse, J.R. Dahn, F. Buda, J. Phys. Chem. **99**, 1896 (1995).